CESIUM BASED POLYOXOMETALATES AS CO-CATALYSTS FOR PROTON EXCHANGE MEMBRANE FUEL CELLS (PEMFC)

GIANLUCA D'ANGELO

DISSERTAÇÃO PARA OBTENÇÃO DO GRAU DE MESTRE EM

QUÍMICA

ORIENTADORES:

Dr. Francesco Nobili

Prof[a]. Maria de Fátima Grilo da Costa Montemor

JÚRI

Presidente: Prof[a]. Maria Matilde Soares Duarte Marques

Orientador: Prof[a]. Maria de Fátima Grilo da Costa Montemor

Vogal: Prof. Corrado Bacchiocchi

Vogal: Dr. Diogo Miguel Franco dos Santos

DEZEMBRO DE 2015

INDEX

LIST OF FIGURE

LIST OF TABLES

ABSTRACT

O trabalho descrito nesta tese foi orientado para a síntese e caracterização de suportes catalíticos de células de combustível de tipo PEM (*proton exchange membrane*) baseadas em polioxometalatos (POM) contendo césio ($Cs_xH_{5-x}PMo_{10}V_2O_{40}\cdot 8H_2O$), a partir do heteropoliácido $H_5PMo_{10}V_2O_{40}\cdot 8H_2O$. Foram sintetizados e analisados três POMs contendo diferentes proporções de césio, respetivamente $Cs_{2.5}H_{2.5}PMo_{10}V_2O_{40}\cdot 8H_2O$, $Cs_3H_2PMo_{10}V_2O_{40}\cdot 8H_2O$ e $Cs_{3.5}H_{1.5}PMo_{10}V_2O_{40}\cdot 8H_2O$.

Uma vez sintetizados, e com o objetivo de obter informação sobre a sua morfologia e composição, os compostos foram analisados por métodos físicos (SEM-XRD, IV, XRD). Estas análises foram úteis para prever o possível desempenho eletroquímico dos compostos sintetizados. Seguidamente foram preparadas combinações usando os três POMs sintetizados e dois conteúdos de platina diferentes. Deste modo, foi possível compreender qual a combinação Pt/POM que resultava no melhor desempenho eletroquímico e qual dos três POMs sintetizados era mais vantajoso. Foram efetuados três tipos de análises: voltametria cíclica (VC), para caracterizar os processos redox nas amostras investigadas; voltametria de varrimento linear (VVL) com um elétrodo de disco rotativo (EDR), para estudar a cinética da reação de redução de oxigénio (RRO), e finalmente *stripping* de CO, para obter informação sobre a ocorrência de envenenamento do catalisador por CO. Foram ainda realizados ensaios numa célula de combustível completa, tendo sido obtidas curvas de polarização e aplicada espectroscopia de impedância eletroquímica, pela sua utilidade na avaliação do desempenho dos elétrodos modificados com POMs sintetizados neste trabalho. Os bons resultados obtidos abrem perspetivas promissoras de desenvolvimento futuro deste tipo de tecnologia.

This thesis work was oriented to the synthesis and characterization of catalytic supports of PEM-Fuel cells based on polyoxometalates (POM) containing Cesium ($Cs_xH_{5-x}PMo_{10}V_2O_{40}\cdot 8H_2O$), starting from the heteropolyacid $H_5PMo_{10}V_2O_{40}\cdot 8H_2O$. Three POMs with different amounts of Cesium, respectively: $Cs_{2.5}H_{2.5}PMo_{10}V_2O_{40}\cdot 8H_2O$, $Cs_3H_2PMo_{10}V_2O_{40}\cdot 8H_2O$ and $Cs_{3.5}H_{1.5}PMo_{10}V_2O_{40}\cdot 8H_2O$, were synthesized and analyzed.

Once synthesized, in order to obtain information on the morphology and composition, the compounds were analyzed by physical methods (SEM-XRD, IR, XRD). These analyses were useful also to get a forecast of what could be the electrochemical performance of the synthesized compounds. Afterwards, inks were prepared and underwent electrochemical characterizations, using the three synthesized POMs and two different platinum contents. In this way, it was possible to understand which Pt/POM combination gives the best electrochemical performance and which of the three POMs synthesized enhances those benefits. Three types of analysis were performed: cyclic voltammetry

(CV), in order to characterize the redox processes of the investigated samples; linear sweep voltammetry (LSV) with rotating disk electrode (RDE), in order to study the kinetics of the oxygen reduction reaction (ORR), and finally CO-stripping, in order to obtain information on catalyst poisoning by CO. Moreover, tests have been performed in a complete fuel cell, recording polarization curves and electrochemical impedance spectroscopy, useful to evaluate the performance of the electrodes modified with POMs synthesized in this work. The good results open promising future developments in the use of this type of technology.

AIM OF THE THESIS

The object of this work is the synthesis and characterization of co-catalysts support (POMs) for Platinum used as catalyst in Oxygen reduction reaction (ORR), in PEM-Fuel Cells. The key point of the application of these insoluble polyoxometalates is the high surface area that helps to increase the dispersion of nano-size Pt, increasing the active area. In this way it is possible to use lower amounts of Platinum, reducing the cost of the final PEM-fuel cell. Thanks to high surface acidity, high proton conductivity, insolubility in water and fast redox behaviour, POMs can also help the catalytic processes involved in ORR. So, the main goal of this work is to maintain performance, reducing the amount of Platinum used in PEM-Fuel cells.

KEY WORDS

Catalysis, Oxygen Reduction Reaction (ORR), Polyoxometalates, PEM fuel cells, Reduced platinum loading.

PALAVRAS-CHAVE

Catálise, Células de combustível de tipo PEM, Menor *loading* de platina, Polioxometalatos, Reacção de redução de oxigénio

ABBREVIATION LIST

POM – polyoxometalates

POM 2.5-2-10 – $Cs_{2.5}H_{2.5}PMo_{10}V_2O_{40}{\cdot}8H_2O$

POM 3-2-10 – $Cs_3H_{2.5}PMo_{10}V_2O_{40}{\cdot}8H_2O$

POM 3.5-2-10 – $Cs_{3.5}H_{2.5}PMo_{10}V_2O_{40}{\cdot}8H_2O$

PEMFC – proton exchange membrane fuel cell

HOR – Hydrogen oxidation reaction

ORR – Oxygen reduction reaction

SHE – standard Hydrogen electrode

RRDE – rotating ring-disk electrode

PVM – phosphovanadomolibdic acid(s)

PVM 2-10 – $H_5PMo_{10}V_2O_{40}{\cdot}8H_2O$

K-L – Koutecky-Levich

RH – Relative humidity

Pt – Platinum

GC – glassy carbon

GDL – gas diffusion layer

MEA – membrane electrode assembly

Comm. MEA – commercial MEA

Mod. MEA 1 – modified MEA with POM 3-2-10

Mod. MEA 2 – modified MEA with POM 2.5-2-10

1. INTRODUCTION

1.1 Fuel Cells – Basic Principles

The basic operation of the fuel cell is extremely simple. The first demonstration of a fuel cell was by lawyer and scientist William Grove in 1839, using an experiment along the lines of that show in **Figure 1**. In **Figure 1(a)**, water is being electrolysed into hydrogen and oxygen by passing an electric current through it. In **Figure 1(b)**, the power supply has been replaced with an ammeter, and a small a current is flowing. The electrolysis is being reversed – the hydrogen and oxygen are recombining, and an electric current is being produced.[1]

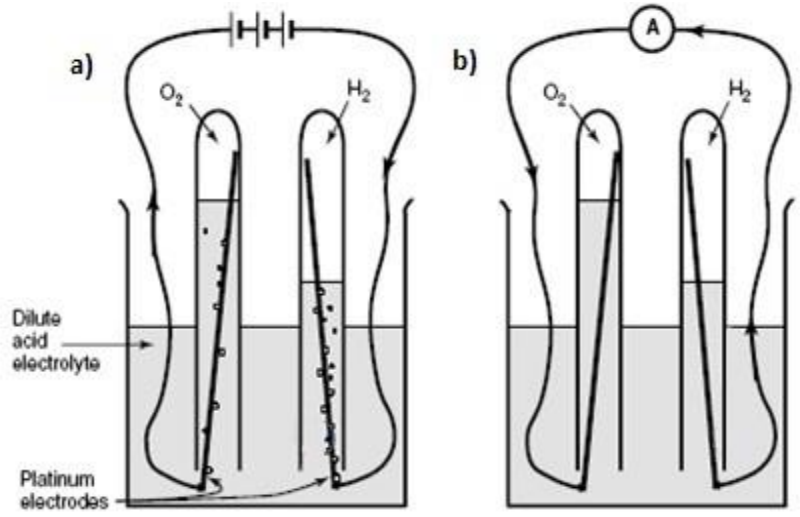

Figure 1: (a) The electrolysis of water. The water is separated into hydrogen and oxygen by the passage of an electric current. (b) A small current flows. The oxygen and the hydrogen are recombining.

We can look the fuel cell as a hydrogen combustion summarized in this simple reaction:

$$2H_2 + O_2 \longrightarrow 2H_2O \qquad (1)$$

A fuel cell is an electrochemical tool that continuously converts chemical energy into electric energy for as long as fuel and oxidant are supplied, during reactions heat energy being liberated.

Fuel cells therefore bear similarities to batteries, with which they share the electrochemical nature of the power generation process, and to the engines which - unlike batteries - will work continuously consuming a fuel.[2]

Unlike engines or batteries, a fuel cell does not need recharging, it operates quietly and efficiently, and when hydrogen is used as fuel the only waste product is water.

Fuel cell consumes substances from outside and is therefore able to function without interruption until the system is supplied with fuel and oxidant, and this further differentiates it from a normal battery.

There are many types of fuel cells, but they all consist in two electrodes (an anode and a cathode) and an electrolyte. At the anode a catalyst oxidizes the hydrogen turning this latter into a positively charged ion and a negatively charged electron. The hydrogen ions are transported through the electrolyte after the reaction, at the same time electrons are transported from the anode to the cathode through an external circuit, producing direct current electricity. The electrolyte is a substance specifically designed so ions can pass through it, but the electrons cannot. At the cathode, hydrogen ions are reunited with the electrons and the two react with oxygen to form water **(Figure 2**).

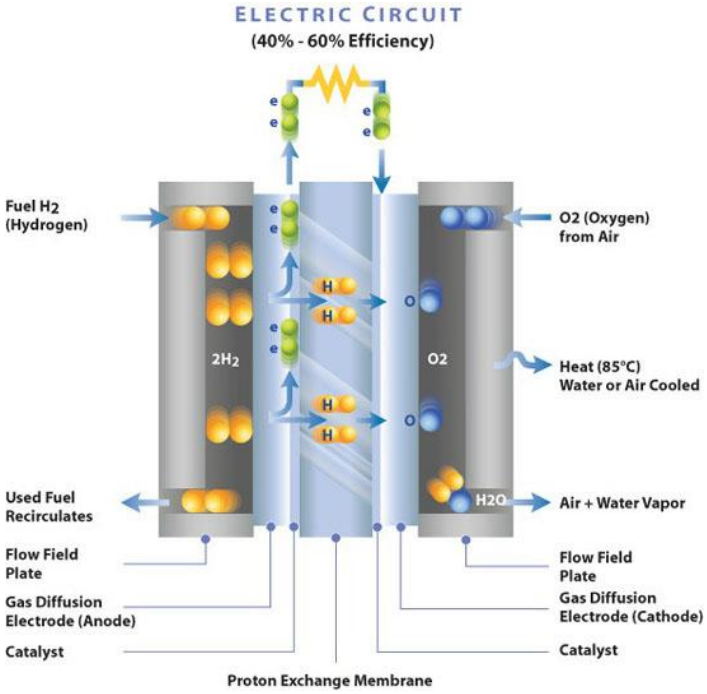

Figure 2: Representation of a generic fuel cell.

The voltage of a fuel cell is quite small, about 0.7 V when drawing a useful current. This means that to produce a useful voltage many cells have to be connected in series. Such a collection of fuel cells in series is known as "stack"[1] (**Figure 3**).

Figure 3: A stack and a single fuel cell.

1.2 Types of Fuel Cell

Fuel cells are classified primarily by the kind of electrolyte they employ (alkaline, polymer electrolyte, phosphoric acid, molten carbonate, solid oxide). This classification determines the temperature range in which the cell operates (low and high temperature cells), the kind of electro-chemical reactions that take place in the cell, the kind of catalysts required, the fuel required, the life of the cell, the nature of building materials and other factors. These characteristics, in turn, affect the applications for which these cells are most suitable. There are several types of fuel cells currently under development, each with its own advantages, limitations, and potential applications.
Fuel cells are very interesting for the production of electrical energy because they have:

- HIGH ELECTRICAL PERFORMANCES, with values ranging from 40-48% (relative to the lower calorific value of the combustible) for plants with cells at low temperature, reaching over 60% for those with high-temperature cells used in combined cycles;
- POSSIBILITY TO USE OF A WIDE RANGE OF FUELS such as methane, methanol, ethanol, natural gas, synthesis gas (produced from liquid fuels, coal gasification biomass); Modularity, which allows to gradually increase the installed capacity growing demand for electricity, with considerable savings in the economic and construction time; low environmental impact, both in terms of gaseous emissions of those aids, which allows to place the plants in residential areas, making the system especially suitable for the production of distributed electricity;
- POSSIBILITY OF COGENERATION. The heat cogeneration may be available at different temperature, in the form of steam or hot water, useful for sanitary conditions of environments.[3]

The best-known types of fuel cells are alkaline (AFC), molten carbonate (MCFC), phosphoric acid (PAFC), proton exchange membrane (PEMFC), solid oxide (SOFC) and direct methanol (DMFC). Each work on the same principle, striping electrons from hydrogen atoms to create electricity.

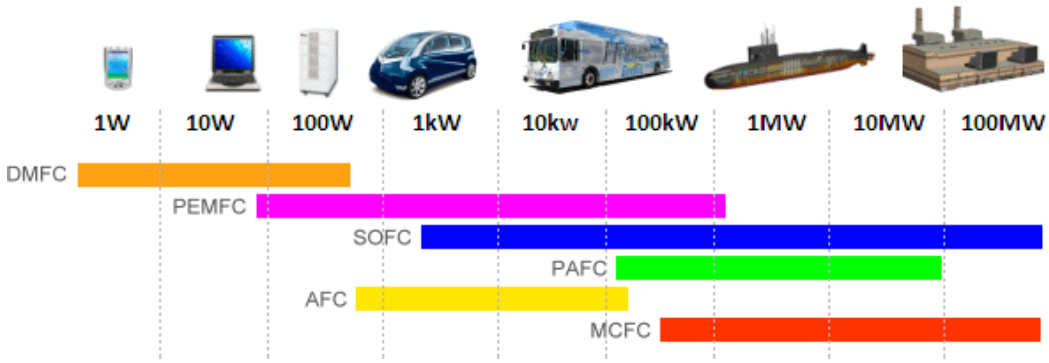

Figure 4: An example of the differences between fuel cell types and their ideal target output.

High temperature working fuel cells are:

- SOFC (Solid Oxide Fuel Cell), is composed of entirely solid materials. The electrolyte is a hard ceramic material made up mainly of zirconium oxide with small amounts of yttrium. The systems operate at about 800~1000ºC, but its large size does not allow use in a small applications[4]. High temperature means these are slow starting systems and most are designed for larger and stationary applications.
- MCFC (Molten Carbonate Fuel Cell), use a molten carbonate salt suspended in a porous ceramic matrix as the electrolyte. Salts commonly used include lithium carbonate, potassium carbonate and sodium carbonate. They operate at high temperature, around 650ºC. At the high operating temperatures, Ni (anode) and nickel oxide (cathode) are adequate to promote reaction. Noble metals are not required[5]. These systems can operate on a variety of different fuels, including coal-derived fuel gas, methane or natural gas, eliminating the need for external reformers.

Low temperature working fuel cells are:

- AFC (Alkaline Fuel Cell), is one of the oldest types of fuel cell. The electrolyte they use is made of liquid potassium hydroxide (KOH). One of the major advantages for an alkaline fuel cell is that non-precious metals can be used as a catalyst. However, the catalysts can be easily poisoned by CO_2 that can reacts with KOH to form K_2CO_3 that precipitates altering the electrolyte. As such, the hydrogen and oxygen used in an AFC needs to be purified, which is a more costly process. The operating temperature of AFC's is between 100ºC ~ 250ºC.
- PEMFC (Proton Exchange Membrane Fuel Cell), use a platinum coated solid polymer that requires only hydrogen and oxygen to produce electricity. The advantages of a PEM fuel cell is that they have a high power density and are low in weight. They are also able to operate in low temperatures, typically between 60°C and 120°C, which allows them to start quickly (less warm uptime). The only liquid in this fuel cell is water, thus corrosion problems are minimal. The major disadvantage of PEM fuel cells is that they require an expensive catalyst, in this case platinum, which adds to the overall unit cost. Hydrogen delivery is also another significant barrier, it requires careful handling and storage. This makes PEM fuel cells more applicable for industrial uses where delivery and storage can be in a controlled environment.
- PAFC (Phosphoric Acid Fuel Cell). Phosphoric acid concentrated is the electrolyte used in a PAFC. As an acid, it requires a high temperature (150ºC ~ 200ºC) to start the reaction. At lower temperatures, PA is a poor ionic conductor. It also uses platinum as a catalyst, similar to PEM fuel cells, which is costly. However, PAFC's are more tolerant to impurities in fuels than PEM fuel cells, and they are very efficient at generating electricity and heat, which makes

them ideal for power plants. However, they are typically large and heavy which makes them less than ideal for smaller or portable applications.

- DMFC (Direct Methanol Fuel Cell), are PEM based fuel cell that use methanol instead of pure hydrogen. As such, they share many of the same advantages of a PEM fuel cell, with the added benefit that methanol is a much easier and safer fuel for transportation and storage. The disadvantage of methanol is that the reaction is often not as efficient as pure hydrogen because methanol can often move across the membrane decreasing its concentration at the anode and poisoning the cathode. To address these concerns, some fuel cells reform the methanol (RMFC) before it reacts with the catalyst. While this approach improves the efficiency of methanol, it still requires an expensive reforming process that needs to operate at much higher temperatures (250ºC).

Thanks to their small dimensions, low weight and capability to provide high power at low temperatures, PEMFCs are being actively developed for use in cars and buses, as well as for a very wide range of portable applications, and also for combined heat and power system[1]. In this type of fuel cells the electrolyte is a polymer membrane, the perfluorosulfonic acid (PFSA), that is a solid organic acid better known as NAFION®.

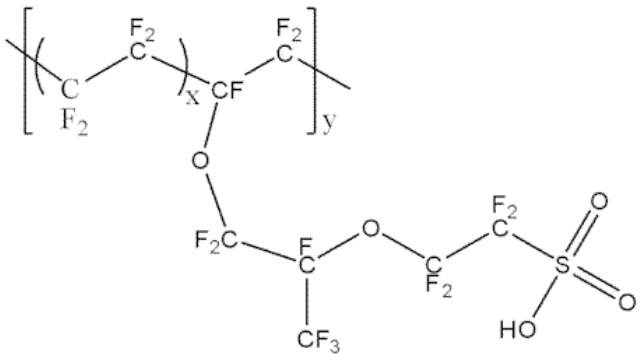

Figure 5: NAFION® monomer structure.

The commercial line of NAFION® cation-exchange membranes possess many desirable properties for moderate temperature PEM fuel cell applications, such as high proton conductivity under fully hydrated conditions and good oxidative stability[6], this made possible to obtain good performance fuel cells.

1.3 Main Applications

The recent increasing impetus in developing and commercializing fuel cells in both stationary and mobile applications, are due to its several advantages. These include clean by-products (e.g., water),

which means it is zero waste emissions. They also operate quietly, not having any moving parts, even when with extra fuel processing and supply equipment.

In the 1960s, the first practical fuels were developed and then used in the U.S Gemini and Apollo programs for space applications[7].

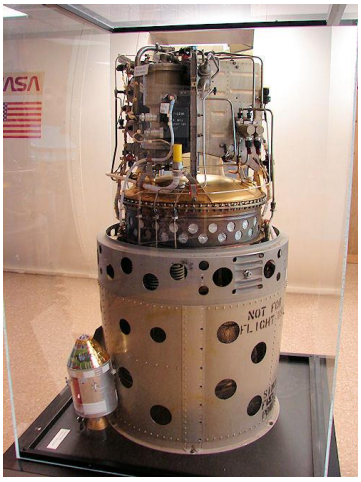

Figure 6: An example of fuel cell used in space missions.

However fuel cells have also been used increasingly for terrestrial (stationary and mobile) applications. For example, in 1993, Ballard Power System demonstrated fuel cell powered buses. Then all major automotive manufactures developed fuel cell vehicle prototypes in the late 1990s and the early 2000s, which underwent tests in the United States, Japan and Europe. In 2005, Samsung Electronics also unveiled a prototype of fuel cells for portable power applications that can run a laptop about 15 h[7].

Figure 7: Examples of fuel cells in mobile applications.

For stationary power applications, more than 2500 fuel cell stationary power systems have already been installed globally at hospitals, office buildings, utility power plants and so on[7].

Figure 8: On left: fuel cell used in power plants; on right: fuel cell used on a building.

1.4 PEMFC (Proton Exchange Membrane Fuel Cell)

Polymer electrolyte membrane (PEM) fuel cells are promising candidates for mobile applications (e.g. cars) due to the low operating temperature that allows a relatively short start-up, no toxic emission and fairly good performance. But these types of systems require pure hydrogen as a fuel and noble metals as catalyst (usually Pt), which results in a high cost. PEMFCs are particularly amenable for use as a laboratory experiment, due to safety and operational advantages[8], where the lifetime requirements and the high loadings of noble metals for mobile applications can be achieved. During the operating cycle these systems may present problems such as chemical degradation or mechanical failure of the membrane, loss of electrochemically active area (ECSA) of the catalyst and chemical and mechanical degradation of the gas diffusion layer.

1.4.1 Working Principle

A PEM fuel cell contains a solid polymer electrolyte and porous electrodes containing a Pt catalyst. PEMFC is an electrochemical cell that is fed hydrogen, which is oxidized at the anode, and oxygen that is reduced at the cathode. The protons released during the oxidation of hydrogen are conducted through the proton ex-change membrane to the cathode. Since the membrane is not electrically conductive, the electrons released from the hydrogen travel along the electrical detour provided and an electrical current is generated[9] (**Figure 9**).

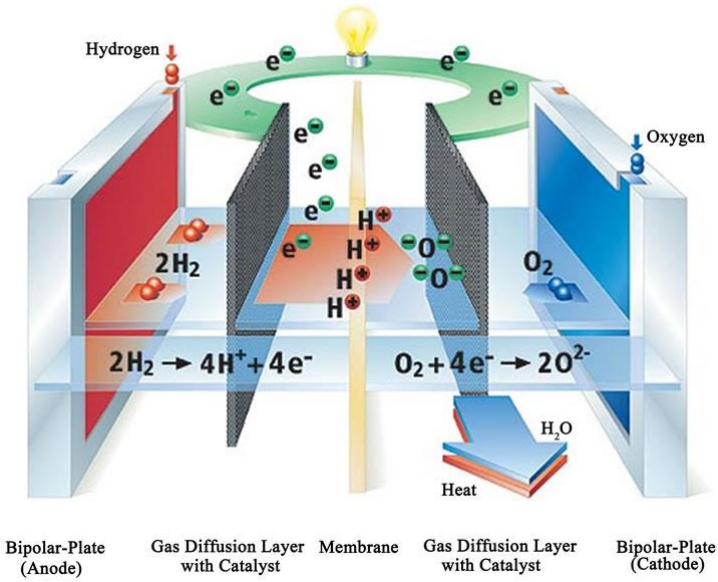

Figure 9: Schematic representation of a PEMFC.

The reactants gas (hydrogen and oxygen) flows into the cell through the flow-field channels. From these latter the gases diffuse trough the gas-diffusion layers into the catalyst layers, where the electrochemical reactions take place. The only generated by-product is water that is carried away from the cell by diffusion/permeation through the cathode GDL into the flow-filed channels and by back-diffusion through the membrane to the anode side. The characteristics reactions that occur in a PEMFC are:

$$H_2 \rightarrow 2H^+ + 2e^- \qquad (2)$$

$$\frac{1}{2} O_2 + 2H^+ + 2e^- \rightarrow H_2O \qquad (3)$$

$$H_2 + \frac{1}{2} O_2 \rightarrow H_2O \qquad (4)$$

When an external resistance is applied to the cell, non-equilibrium exists and current flows. The cell voltage becomes smaller as the net reaction rate increases because of irreversible losses[8]. A representative polarization curve for hydrogen-oxygen PEMFC is shown in **Figure 10**. The voltage-current density relationship for a given fuel cell (geometry, catalyst/electrode characteristic, and electrolyte/membrane properties) and operating conditions (concentration, flow rate, pressure, temperature) is a function of the kinetic, ohmic, and mass transfer resistances. Fuel crossover and internal current losses result from the flow of fuel and electric current in the electrolyte. The

electrolyte should only transport ions, however a certain fuel and electron flow, even if limited, will always occur. Although the fuel loss and internal currents are small, they are the main reason for the real open circuit voltage (OCV) being lower than the theoretical one (E_{rev}).

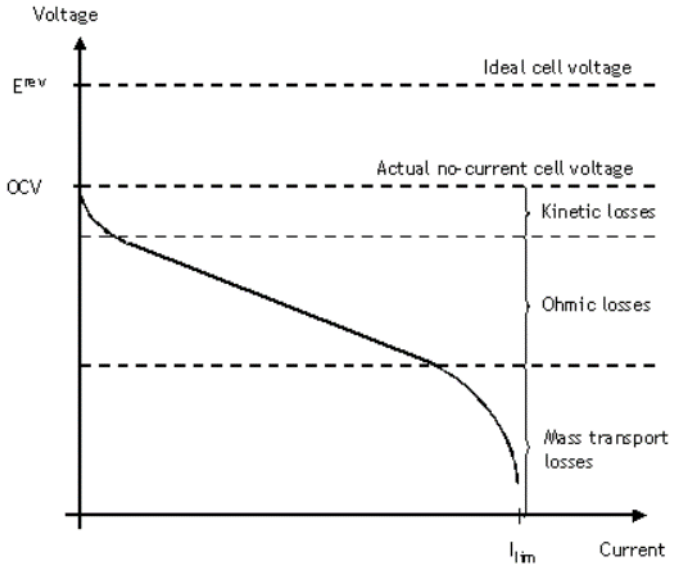

Figure 10: Polarization curve showing the cell potential drop due to electrode activation (kinetic losses), ohmic resistance and mass transport losses.

Activation losses are caused by the slowness of the reactions taking place on the electrode surfaces. The voltage decreases somewhat due to the electrochemical reaction kinetics. The ohmic losses result from resistance to the flow of ions in the electrolyte and of electrons through the cell hardware and various interconnections. The corresponding voltage drop is essentially proportional to current density, hence the term “ohmic losses”. Mass transport losses result from the decrease in reactant concentration at the surface of the electrodes as fuel is used. At maximum (limiting) current, the concentration at the catalyst surface is practically zero, as the reactants are consumed as soon as they are supplied to the surface.

1.4.2 Electrocatalysis in PEMFC

1.4.2.1 Hydrogen Oxidation Reaction (HOR)

The hydrogen oxidation reaction (HOR) is a very important reaction occurring in some kinds of electrochemical sensors and fuel cells. In acid media the catalysis of the reaction is usually promoted by the platinum catalyst dispersed as fine particles on high surface area carbon supports[10]. The kinetics of the reaction is very fast and, in a fuel cell, HOR is usually controlled by mass transfer limitations[11]. HOR involves the adsorption of the gas onto the catalyst surface followed by dissociation of the molecule and an electrochemical reaction to form two protons. The electrochemical oxidation of di-hydrogen:

$$H_2 \rightarrow 2H^+ + 2e^- \quad (E^0 = 0.00 \text{ V vs. SHE}) \qquad (5)$$

on noble metal surfaces such as Pt and Pd is very facile[12]. Other metals also show high activity for H_2 electro-oxidation, but in acidic electrolytes noble metals show the greatest stability towards corrosion or passivation[2]. The accepted mechanism of the HOR is formed by a primary chemical

$$H_2 + 2M \rightarrow 2M\text{-}H_{ads} \quad \text{(Tafel reaction)} \qquad (6)$$

and / or electrochemical adsorption steps:

$$H_2 + M \rightarrow M\text{-}H_{ads} + H^+ + e^- \quad \text{(Heyrovsky reaction)} \qquad (7)$$

followed by a discharge path of the adsorbed hydrogen atom given by

$$M\text{-}H \rightarrow M + H^+ + e^- \quad \text{(Volmer reaction)} \qquad (8)$$

For a given electrode material and electrolyte, the rates of **Eq.(7)** and **Eq.(8)** may be quite different, and the mechanism may be formed preferentially by the Tafel/Volmer steps or by the Heyrovsky-Volmer steps. On Pt electrode, a Tafel-Volmer mechanism, with dissociative adsorption of dihydrogen (Tafel reaction) being the rate determining step (rds), has been proposed for this reaction[13] in acidic electrolytes. While pure H_2 is the ideal choice of fuel for the PEMFC, economical sources of pure H_2 are not readily available. Therefore, currently the most practical source of H_2 is the catalytic processing of hydrocarbons. Hydrogen produced by the steam reforming or partial oxidation of hydrocarbon fuels (gasoline, diesel, methane, alcohols) contains impurities such as CO (1-3%) and

CO_2 (19 - 25%). It is well known that CO binds strongly Pt sites and reduces the number of the catalytic centers available for H_2 adsorption and oxidation. Although the electrochemical CO oxidation:

$$CO + H_2O \rightarrow CO_2 + 2H^+ + 2e^- \quad (E_0 = -0.1 \text{ V vs. SHE}) \qquad (9)$$

is thermodynamically favourable, in practice a large over-potential is required on pure Pt surfaces before oxidation occurs. For example, on dispersed Pt catalysts, the onset of CO oxidation is not observed until 0.5 V at 80ºC. Therefore, in the potential region where anodes need to operate (i.e.0-0.1 V), CO is an inert adsorbate. The degree of CO poisoning of Pt catalysts is highly dependent on both temperature and CO concentration[2] . CO_2 poisoning on pure Pt catalysts is modest when compared to the effect of CO, especially when the large differences in relative concentrations in reformate are considered. The poisoning effect comes from two possible mechanism:

$$CO_2 + H_2 \rightarrow CO + H_2O \qquad (10)$$

$$CO_2 + 2Pt\text{-}H_{ads} \rightarrow Pt\text{-}CO + H_2O + Pt \qquad (11)$$

Both mechanism are forms of the "reverse water-gas shift" reaction with **Eq.(10)** being the familiar gas-phase reaction and **Eq(11)** the electrochemical equivalent. In both cases, the product is CO, which has the same effect as fuel stream CO. The most elegant way to overcome anode poisoning is through the development of CO and CO_2 tolerant electrocatalysts. Much effort has been spent modifying Pt with others metals to improve CO tolerance. In early 1960s Niedrach[14]found that the addition of Ru, Rh and Ir to Pt in the form of unsupported mixed metal powders (blacks) gets substantial tolerance, compared to Pt black alone. Moreover, they found that mixing Pt black with metal oxides, such as $CoMoO_4$, MoO_2 and WO_3, also improves CO tolerance over Pt alone[15]. In the recent years, many researchers have reported the superior CO and CO_2 tolerance of carbon supported PtRu catalysts with respect to carbon-supported Pt catalysts[16].

1.4.2.2 Oxygen Reduction Reaction (ORR)

Oxygen reduction reaction in aqueous solutions occurs mainly by two pathways: the direct 4-electron reduction pathway from O_2 to H_2O, and the 2-electron pathway from O_2 to hydrogen peroxide (H_2O_2)[17]. In PEM-Fuel Cells, ORR is the reaction occurring at the cathode and the 4-electron direct pathway is highly preferred:

$$O_2 + 4H^+ + 4e^- \rightarrow 2H_2O \qquad (12)$$

Normally, the ORR kinetics is very slow. In order to speed up the ORR kinetics to reach a practical usable level in a fuel cell, a cathode ORR catalyst is needed. At the current stage in technology, platinum (Pt)-based materials are the most practical catalyst[17]. The mechanism of the electrochemical O_2 reduction reaction is quite complicated and involves many intermediates, primarily depending on the natures of the electrode material, catalyst, and electrolyte. The theorized mechanism is the following[18]:

$$O_2 + Pt \rightarrow Pt\text{-}O_2 \qquad (13)$$

$$Pt\text{-}O_2 + H^+ + e^- \rightarrow Pt\text{-}HO_2 \qquad (14)$$

$$Pt\text{-}HO_2 + Pt \rightarrow Pt\text{-}OH + Pt\text{-}O \qquad (15)$$

$$Pt\text{-}OH + Pt\text{-}O + 3H^+ + 3e^- \rightarrow 2Pt + 2H_2O \qquad (16)$$

Although a huge variety of catalysts have been investigated, at present Pt-based catalysts are the most widely used cathode materials in low temperature fuel cells, due to their intrinsic activity and stability in acidic solutions. Because the Pt-based catalyst are too expensive for making commercially viable fuel cells, extensive research over the past several decades has focused on developing alternative catalyst, including non-noble metal catalysts[19]. Co- and Fe-macrocycles were found to catalyse the ORR in acid medium. Fe/N/C or Co/N/C electrocatalysts for the ORR in PEM fuel cells have been widely studied due to their promising performance[20]. In particular, it has been demonstrated that high-surface-area CoTMPP/C catalyst can rival Pt/C under specific operating conditions[21]. Unfortunately, most of the catalysts above mentioned and reported in the literature, are not stable in fuel cells, even for relatively short times[22]. Currently, the focus of many research groups is to understand the cause(s) of instability of Fe/N/C or Co/N/C catalysts. As mentioned above, oxygen reduction is a complex reaction that includes a number of electrochemical and/or chemical steps and various intermediates. The number of potential mechanisms is so high that it is almost impossible to determine which one occurs for any electrode material and operating conditions. However, all of these mechanisms can be classified into two distinct reaction paths: a direct path without formation of soluble H_2O_2, and a series path with H_2O_2 diffusing from the electrode. In the series path, H_2O_2 can be further reduced to H_2O or can be decomposed chemically. As we have seen, for practical applications of a fuel cell, the

direct path is desirable because the formation of H_2O_2 reduces the cell performances by limiting the cell potential and lead to internal corrosion phenomena (membrane corrosion). In the case of N-macrocycle metal complexes, H_2O_2 is believed to be responsible for the deterioration of electrode performance over time, mainly due to corrosion of the carbon support. Despite ongoing studies, the identification of the active site(s) of such transition metal-nitrogencarbon (M-N-C) type catalysts is not yet complete[23].

1.5 Polyoxometalates (POMs)

Due to the high value of the platinum, in the path towards fuel cells commercialization, one of the big challenges is to reduce the catalyst material cost. Two approaches are currently very attractive: the exploration of non-noble catalysts and the reduction of the Pt loading[24]. In the last years, the research is focused on the development of compounds that make it possible to reduce the amount of Platinum, as polyoxometalates (POMs). POMs are a class of inorganic compounds that is unmatched not only in terms of molecular and electronic structural versatility, but also regarding reactivity and relevance to analytical chemistry, catalysis, biology, medicine, geochemistry, materials science and topology[25]. POMs are synthetized starting from heteropolyacids, indicated with the acronym HPA (HeteropolyAcid), and they are made of oxygen and early transition metals (e.g., M = V, Nb, Ta, Mo, W) at their highest oxidation states. They may also contain a variety of heteroatoms (e.g., X = P, As, Si, Ge). POMs are molecular oxides which are distinguishable from the majority of metal oxides[26]. They may contain tens to hundreds of metal atoms that reach nuclearities as high as 368 metal atoms in one single cluster molecule (forming nanoparticles). The existence of the enormous variety of polyoxometalates is due to the fact that more than half of the elements of the periodic table can be incorporated within the structure of these compounds, such as $[P_2Mo_{18}O_{62}]^{6-}$, $[SiMo_2W_{10}O_{40}]^{4-}$, $[PMo_{10}V_2O_{40}]^{5-}$ etc. The first report of what we refer now to a POM dates back to Berzelius (1826) who described the yellow precipitate that is produced when ammonium molybdate is added in excess to phosphoric acid and which is now known as$(NH_4)_3[PMo_{12}O_{40}]_{aq}$[25], while in 1864 Marignac[27] successfully synthesized silicotungstic acid. The two basic structures of POMs are Keggin (X/M = 1/12) and Dawson (X/M = 2/18) structures. Keggin-type heteropolyanions of molybdenum are particularly attractive because of their ability to adsorb irreversibly on carbon and metal surfaces to form structured films[28], that provide a good catalyst dispersion when used as catalyst support. POMs are frequently formed in aqueous media. However, in some cases, the assembly of the oxoanions may also occur in non-aqueous media or even in the solid state such as in minerals[29].The stability of POMs in aqueous or non-aqueous solvents is generally measured by their ability to retain their structural identities and avoid degradation or transformation to other forms. Nevertheless, POMs under particular conditions may undergo degradation, and thanks to modern techniques, we now have a better understanding of the mechanisms under which POMs transform from one state to another during the degradation process.

1.5.1 POMs classification and types of structure

The structure[30] of these compounds contains a high atomic proportion of oxygen atoms that are linked to a different cluster, sometimes hydrogen and atoms of at least two other elements. One of these is a transition metal atom from V or VI group in its high oxidation states, e.g. V^{5+}, Mo^{6+}, W^{6+} called "addenda atom". The second is called "heteroatom" and its proportion is much smaller, e.g. P^{5+} and Si^{4+}. These structures contain anions packed around the cations in geometries governed by the relationship between the radii. A general classification of POMs is based on the presence or absence of the heteroatom (X). Therefore, POMs can be divided into two large families: the isopolyoxometallates (or isopolyanions), and heteropolyoxometallates or (heteropolyanions):

- Isopolyanions: $[MmOy]^{p-}$
- Heteropolyanions: $[XxMmOy]^{q-}$ (where $x \leq m$)

where M is a transition metal (addenda atoms) and X is the atom at the center of the structure. The composition of the cluster can be very complex because various elements M can be present in the structure. Later, we will see a general classification of the different structures.
The crystal structure of a heteropolycompound is governed by two basic principles[31]:

1. Any atom M is located in the center of polyhedral cavities, usually octahedral, forming polyhedra of the type MOx and their coordination through pπ-dπ bonds. The oxygen atoms are located at the top.
2. The polyoxometalates are characterized by octahedral MO_6 units that can have no more than two vertices free by oxygen atoms.

For these kinds of compounds there are three crystal structures:

- the primary structure, formed by the molecular unit (the heteropolyanions);
- the secondary structure: the three-dimensional arrangement of the different units, linked to water molecules, cations and other molecules;
- the tertiary structure formed by the union of different secondary structures.

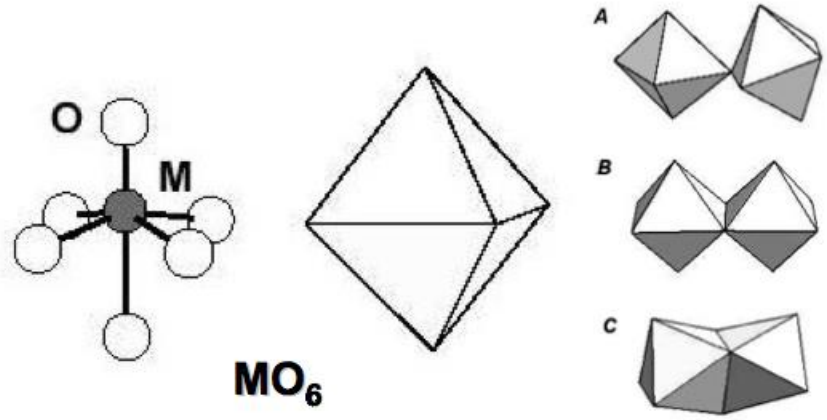

Figure 11: Basic unit MO_6 and the three possible unions between two octahedral units, where each corner represents oxygen position A) corner sharing, B) edge sharing and C) face sharing.

The structure of heteropolyanions is characterized by the rearrangement of polyhedra MO_X (where M = V, Mo, W, Nb or more rarely Ta), or more polyhedra around a central XO_n (where X = P, Si, Ge in rare cases, As, Co) which may have symmetry T_d, O_h, or I_h. It is possible to distinguish different classes (**Figure 12)** according to the different symmetry of the central heteroatom X in the polyhedron:

- Wells - Dawson $[X_2M_{18}O_{62}]^{2n-16}$ (T_d)
- Anderson - Evans $[XM_6O_{24}]^{n-}$ (O_h)
- Dexter - Silverton $[XM_{12}O_{42}]^{n-12}$ (I_h)
- Keggin $[XM_{12}O_{40}]^{n-8}$ (T_d)

We will focus the attention on the Keggin-type structure because catalysts with this structure have demonstrated a good catalytic properties.

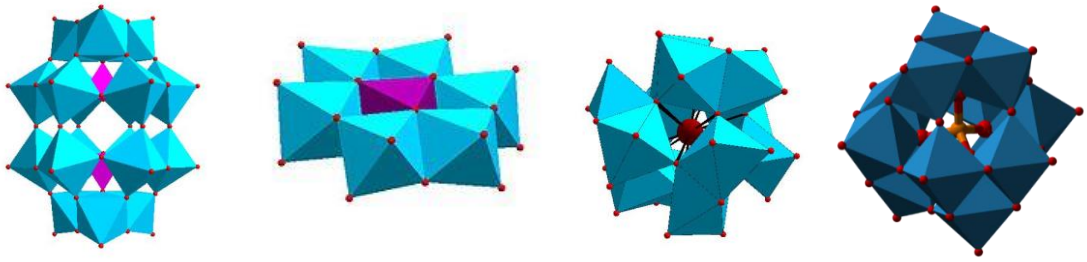

Figure 12: From left: Wells – Dawson $[X_2M_{18}O_{62}]^{2n-16}$ (T_d); Anderson - Evans $[XM_6O_{24}]^{n-}$ (O_h); Dexter - Silverton $[XM_{12}O_{42}]^{n-12}$ (I_h); Keggin $[XM_{12}O_{40}]^{n-8}$ (T_d).

1.5.2 Keggin-type structure

The arrangement of twelve metal atoms (e.g. M = V, Nb, Ta, Mo, W) around one single heteroatom (e.g. X = P, As, Si, Ge) forms a Keggin based POM, where X/M = 1/12[26]. This kind of structure is the most common for all the polyoxometalates as it is the most stable. In the Keggin structure, the heteroatom X is bonded to four oxygen atoms to form a tetrahedron and each metal atom is linked to six oxygen atoms to form octahedra. The assembly of three octahedra yields a trimetallic group M_3O_{13}. The trimetallic groups are connected to others and the common site of M_3O_{13} is linked to the central heteroatom X. In summary, there are four M_3O_{13} gathered around the central heteroatoms X to form $(XO_4)M_{12}O_{36}$[26].

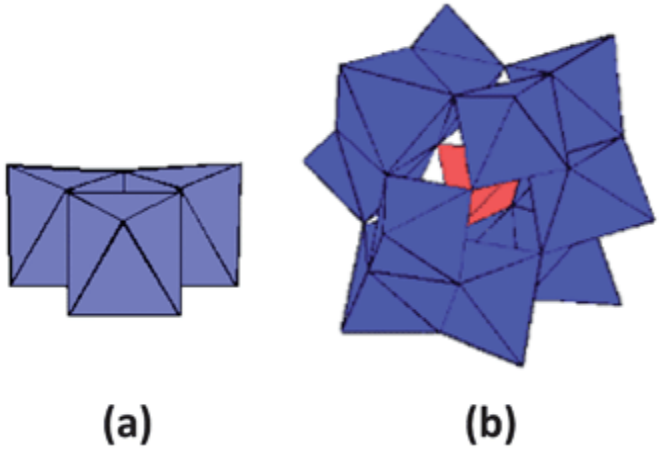

Figure 13: (a) Combination of three octahedral to form a trimetallic group M_3O_{13}. (b) Structure of the Kegging-type POM.

1.5.2.1 Primary structure

The basic structural unit consists of a central tetrahedron $[Xn+O_4]^{(8-n)}$ surrounded by 12 octahedral MO_6 groups, organized themselves into four groups M_3O_{13} (**Figure 14)**that share vertices or edges in order to minimize the electrostatic repulsion. Looking in detail the primary structure of Keggin heteropolyanion (**Figure 14**), we see that there are four different types of oxygen:

- 4 internal oxygen atoms (O_i): connecting the atom to the triads of octahedras M_3O_{13};
- 12 corner-sharing oxygen atoms (O_c): they connect the octahedras that share the vertex and not share any O_i;
- 12 edge-sharing oxygen atoms (O_c): they connect the octahedras that share the edgeconnecting two addenda that share the same O_i;
- 12 terminal oxygen atoms (O_t): are connected to only one M with partial double bonds.

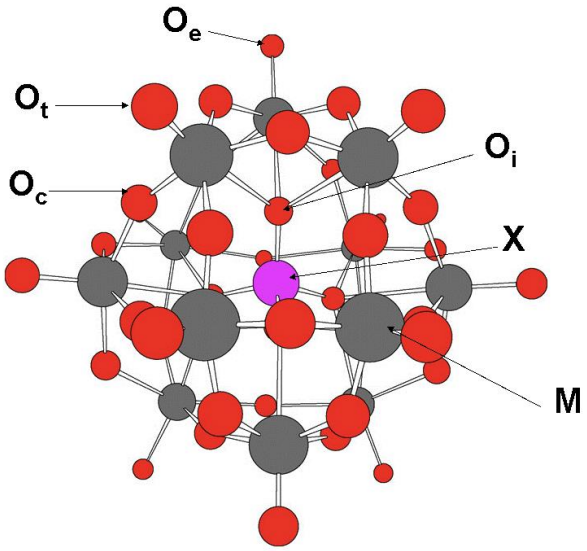

Figure 14: Schematic representation of Keggin primary structure.

The formation of double bonds M=O_t is highlighted and justified by a distorted octahedron in which each individual atom M is closer to the corresponding O_t, thus increasing the polarization of that bond. This is an important feature that gives these compounds the strength of Brönsted acid. Different forms of isomerism are all related to the base structure by rotation of 60° for one or more groups M_3O_{13}. Each of the four groups, in fact, may be subject to rotation, theoretically generating five different structural isomers α, β, γ, δ and ε. Beyond theoretical considerations, only α and β isomers have importance on a practical level. The formation of both isomers depends of course on the method of synthesis. None of the other isomers has been isolated and this suggests that they are too unstable to exist in solution. The α - Keggin, where octahedral share only vertices, are the most stabile isomers. The second type of isomerism is called positional isomerism: it occurs when two different types of addenda are present in the structure. Finally, it is possible to form the "lacunary structures" or unsaturated structures, which are species derived by removing one or more MO unit from Keggin structures to give defect structures[32].

1.5.2.2 Secondary structure

The secondary structure consists of three-dimensional arrangement of polyanions, cations and crystallization water. Generally heteropolyacids are arranged in a crystal lattice with a cubic structure body as shown, in which the cations $[H_5O_2]^+$ link anions together by forming hydrogen bonds with an oxygen end of each anion.

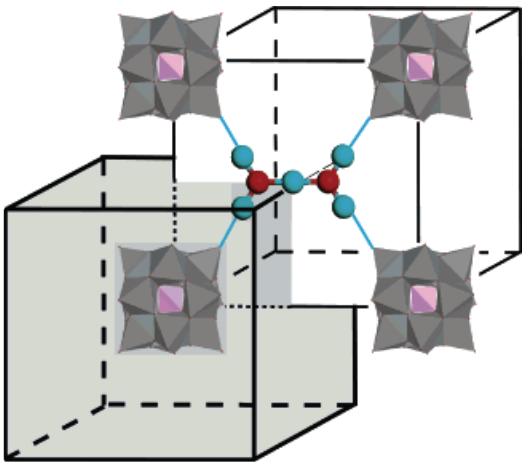

Figure 15: BCC structure of the HPA. Intercell interactions of the species $H_5O_2^+$ are highlighted.

The amount of water of hydration, adjustable through thermal treatment, affects the degree of solvation of the proton H^+ (for example, $[H_5O_2]^+$). The ability to vary the water content impacts the amount of H bonds in the structure and thus the crystalline size of the lattice[33].

1.5.2.3 Tertiary structure

The aggregates of microcrystals form the tertiary structure. The nature of counteraction strongly influences the tertiary structure in terms of particle size, porosity and surface area.

Some large cations like Cs^+ or NH^{4+} polyoxometalates give a high surface area, a large porosity and high thermal stability, very important features for applications in catalysis[34].

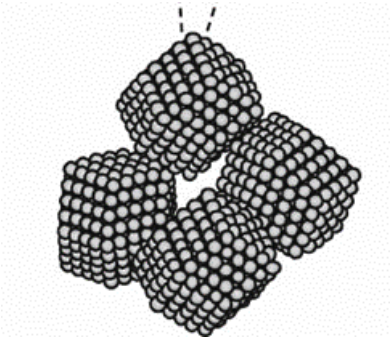

Figure 16: Schematic representation of HPA tertiary structure.

1.5.3 Salts of polyoxometalates

Polyoxometalates can forms salts, and this is a very important characteristic. Salts can be obtained by titration of the acid (HPA) with a metallic salt, for example with chloride or a carbonate. Cations as Cs^+, NH_4^+, or Rb^+ occupy the sites of $H_5O_2^+$ in the secondary structure of the polyoxometalates[35]. According to the size of counteraction the synthesized salts can be classified into two groups: group A is associated with cations of small size such Na^+ and Cu^+, and group B includes cations as large as Cs^+ or NH_4^+. Obviously, the properties of the salts depends on the used counteraction. In general, salts and hydrogenated forms of group A have a low surface area, which reflects their solubility in water, while group B salts are insoluble in water, have a high surface area and strong acidity. The properties of aggregates of the B group are particularly interesting because they can disperse, within the micro-mesoporous structure (tertiary structure), particles of Pt as catalysts. Okuhara et al.[36] have proposed the model for the microstructure of the Cs^+ salts reported in **Figure 17**. The primary structure is always a Keggin structure. The arrangement of the primary structure together with Cs^+ forms the secondary structure, which corresponds to the microcrystallites. During the preparation step, the microcrystallites form aggregates with dimensions near 1μm. These aggregates are called tertiary structure and possess micropores in the range from micropores to mesopores as revealed by N_2 adsorption. The dimension of mesopores varies from 20 to 500 Å, with an area approximately equivalent to 30% of total area. The rest of measured area is covered by micropores (width < 2nm). In any case, the Cs content precisely controls the pore size of acidic Cs^+ salts[37].

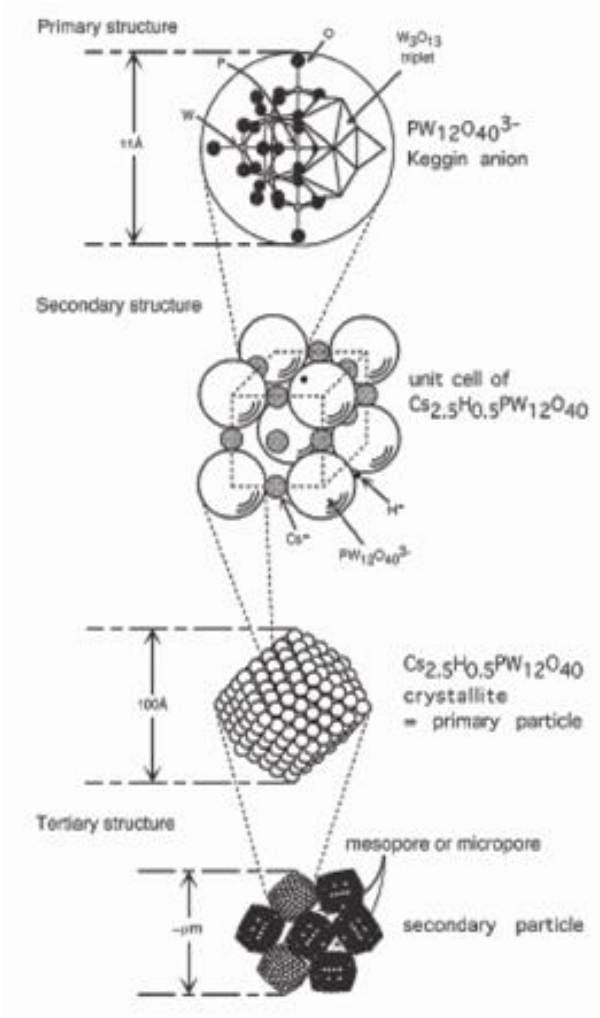

Figure 17: Model for microstructures of Cs salts.

The surface area depends on the countercation, but it is also variable depending on the precipitation and drying process and it changes with the number of substituted protons. The surface area of $Cs_xH_{(3+n)-x}PMo_{12-n}V_nO_{40}$ shows a maximum when Cs ratio is between the range of 2.5 and 3.5[38].At ratio value 3 it reaches a value of $160 m^2g^{-1}$, considerably high if we compare with a value nearly null at 2 or with a few m^2g^{-1} for the hydrogen form[39].These materials show electrocatalytic properties towards a wide range of reaction.

2. EXPERIMENTAL TECHNIQUES

2.1 Physical characterization techniques

2.1.1 Scanning Electron Microscope – Energy dispersive X-ray spectroscopy (SEM - EDX)

Scanning electron microscopy, often coupled with energy dispersive X-ray spectroscopy (SEM/EDX), is the best known and most widely-used of the surface analytical techniques. High resolution images of surface topography, with excellent depth of field, are produced using a highly-focused, scanning (primary) electron beam. The electron beam/sample interactions that occur in a limited region below the sample surface called the "interaction volume", cause the emission of different signals that are collected by specific detectors and converted into an image of the sampled area and viewed or recorded on a cathode ray tube (CRT). The generated signals include secondary electrons, backscattered and Auger electrons, photons of various energies and characteristic X-rays. The signals of greatest interest for surface topography are secondary and backscattered electrons[40]. An image of the sample surface can thus be constructed by measuring secondary electron intensity as a function of the position of the scanning primary electron beam. High spatial resolution is possible because the primary electron beam can be focused to a very small spot (<10 nm)[41].Secondary electrons are emitted as a consequence of inelastic scattering events between primary or backscattered electrons and the sample. Due to their low energy (~10 eV), they can escape only from volume close to the specimen surface. Their intensity depends on surface elements orientation, so their signal carries the main information about surface morphology. Characteristic x-rays are generated when holes created by secondary electron emission are filled by electrons from outer shells. The x-rays energies reflect the transition energies between electron shells of the involved elements. Due to their high energy and escape depth, they can thus be used for elemental analysis of the bulk of the sample (EPMA = electron-probe microanalysis). When an energy-dispersive x-ray detector (EDX) is used, the resulting spectra are usually referred to as EDX spectra and give information about sample composition. Backscattered electrons can be used as such to gain information on the sample composition and, in addition, contribute significantly to the emission of the so-called secondary electrons. The process of backscattering takes place as a result of a sequence of elastic scattering events inside the interaction volume in which the change of direction eventually results in re-emission of electrons. **Figure 18** represents a scheme of the components of the SEM microscope.

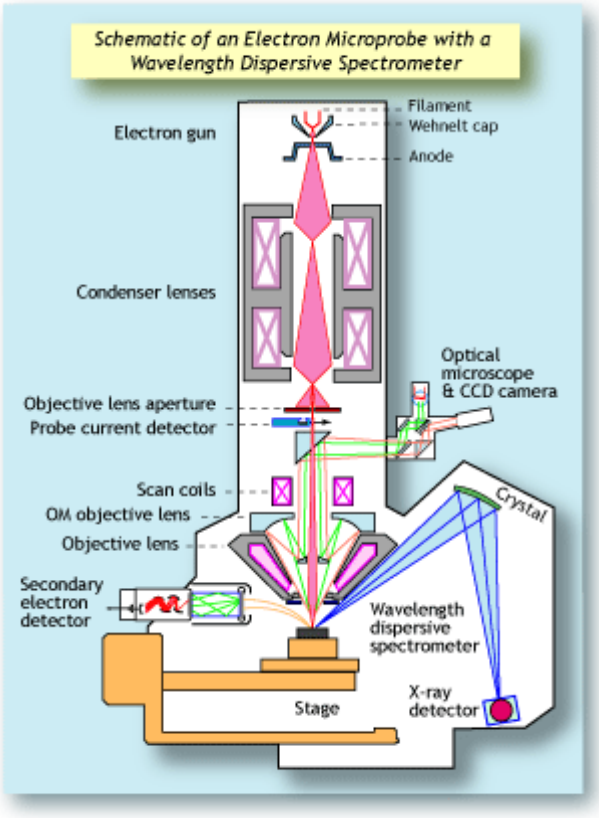

Figure 18: Scheme of a typical Scanning Electron Microscope.

When SEM is used in conjunction with EDX (Energy Dispersive X-ray spectroscopy) the analyst can perform an elemental analysis on microscopic sections of the material or contaminants that may be present.

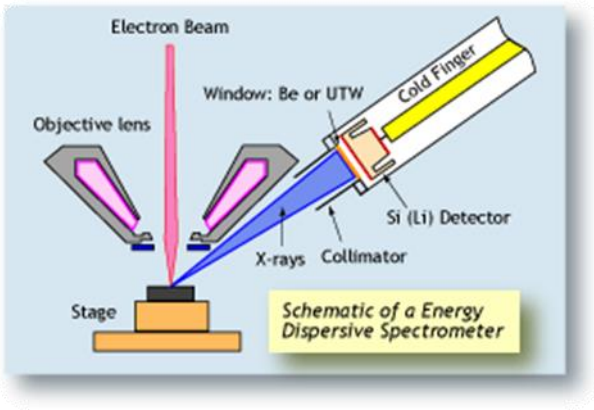

Figure 19: Detail of instrument part able to make EDX analysis.

SEM-EDX is considered a relatively rapid, inexpensive, and basically non-destructive approach to surface analysis.

It is often used to survey surface analytical problems before proceeding to techniques that are more surface-sensitive and specialized[41].

2.1.2 Infrared Spectroscopy (IR)

Infrared spectroscopy is certainly one of the most important analytical techniques available to today's scientists. One of the great advantages of infrared spectroscopy is that virtually any sample in virtually any state may be studied[42]. This technique involves examination of vibrational modes of atoms in a molecule. For a molecule to show infrared absorptions it must possess a specific features, i.e. an electric dipole moment of the molecule must change during the vibration (selection rule)[42]. Molecules contain bonds of specific spatial orientation energy. These bonds are seldom completely rigid, and when energy is supplied, they may bend, distort or stretch. A vary approximate model compares the vibration to that of a harmonic oscillator, such as an ideal spring. If the spring has a force constant, k, and masses m_A and m_B at the end, than the theoretical vibration frequency ν is given by[43]:

$$\nu = \left(\frac{1}{2}\pi\right)\sqrt{k/\mu} \qquad (17)$$

where $\mu = mA \cdot mB \,/\, (m_a + m_b)$ is called the reduced mass. Each type of molecular vibration is characterized by a vibrational quantum number, υ. For a simple stretching vibration, there is a series of levels whose energy is given approximately by[43]:

$$E = h\nu_0 \cdot \left(\upsilon + \frac{1}{2}\right) \qquad (18)$$

This means there is a set of levels spaced energy by $h\nu_0$ or in wavenumber by ν_0. The selection rule for an ideal harmonic oscillator allows transition where $\Delta\upsilon = \pm 1$, giving a single, fundamental vibrational absorption peak at $E = h\nu_0$. However, when the bonds are stretched they weaken, so better models considers this, and the molecules are treated as anharmonic oscillators[43]. Thus, when high energies are involved, larger energy transition may occur, where $\Delta\upsilon = +2, +3$, ect., giving the first overtone at wavenumber approximately double that the fundamental. The electric field of incident radiation interacts with the molecular dipole. When the frequency of the radiation resonates with a molecular vibration, absorption can occur, particularly if excitation of that vibration has an effect on the molecular dipole moment. The energy changes involved in exciting vibrational modes in this way correspond to the infrared spectral region. A full infrared spectrum consists of bands (group frequencies), assignable to particular moieties (e.g. $-CH_2-$, $-CH_3$, C=O), in characteristic frequency regions that are relatively independent on the other groups in the molecule. Since infrared spectroscopy probes molecular vibrations that involve changes in the dipole moment, the vibrations of polar molecular bonds generally correspond to strong infrared bands.

2.1.3 X-ray Diffraction (XRD)

The x-ray diffraction is probably the most effective diagnostic tool to identify the structure of the unknown materials. This technique is based on the registration of X-radiation diffracted by crystalline materials, or that possess an ordered structure. In fact, each material produces a characteristic diffraction pattern that forms a fingerprint making possible the identification by comparison with spectra of known substances. This technique is applicable to any type of material (organic, inorganic or polymeric) in powder and solid state, provided it is in crystalline form. With XRD is possible to define the crystalline phases present in each sample, and also their three-dimensional structure, but does not provide any information on what is the elemental composition of the compound. Diffraction is a phenomenon possible thanks to the existence of phase relationships between two or more waves scattered from set of ordered atoms within the lattice. These phase relationships are derived from the differences of optical path travelled by the various beams. When a crystal is struck with a certain angle of incidence θ by an X-radiation, it is in part diffused from the layer of atoms on the surface of the crystal, and partly penetrates into the underlying layer from which the atoms is again partly diffused. The total effect of the diffusion by the crystalline centers regularly spaced, is the diffraction of the light beam, which is possible if the spacing between atomic planes is of the order of magnitude of the radiation and if the atoms hit are spatially distributed in a regular manner, as happens in crystalline materials. **Figure 20** represents the section of a crystal struck by X-ray perfectly parallel, and we can see that the only one diffracted beam is the one with an angle of reflection θ equal to the angle θ of incidence.

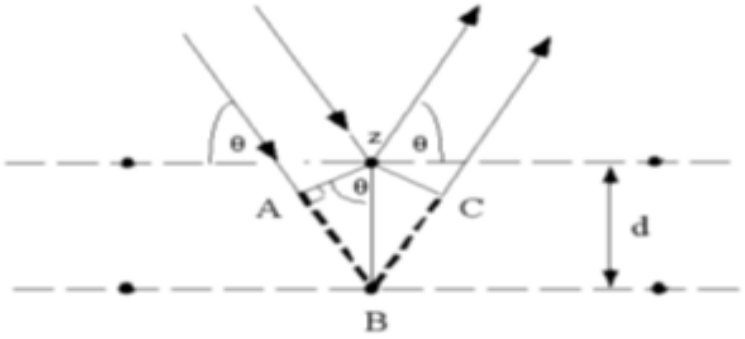

Figure 20: Crystal section struck by X-ray radiation.

Generally, the rays diffused by the planes (hkl) will be completely in phase only if they can satisfy the following formula:

$$n\lambda_{hkl} = 2d_{hkl}sin\theta_{hkl} \quad (19)$$

this relationship is known as Bragg's law, and expresses the condition for the set of planes having the Miller indices (hkl) and θ_{hkl} angle (Bragg angle), whereby said condition is verified. The order of reflection *n* can be any integer and represents the number of wavelengths in the path difference between rays diffused from the adjacent lattice planes. From XRD, the crystallite size can be found out by using the Scherrer's formula:

$$D = \frac{k\lambda}{\beta cos\theta} \qquad (20)$$

where D is the crystallite size, *k* is the shape factor (usually taken as 0.9), λ is the wavelength (1.54 Å), β is the full width of half maxima, θ is the diffraction angle.

2.2 Electrochemical characterization techniques

2.2.1 Linear sweep and cyclic voltammetry (LSV-CV)

Linear sweep voltammetry is a voltammetric method where the current at a working electrode is measured while the potential between the working electrode and a reference electrode is swept linearly in time. Oxidation or reduction of species is registered as a peak in the current signal at the potential at which the species begins to be oxidized or reduced. When cyclic voltammetry reaches a set potential, the working electrode's potential ramp is inverted. This inversion can happen multiple times during a single experiment. The potential-time relation for voltammetry measurements is shown below:

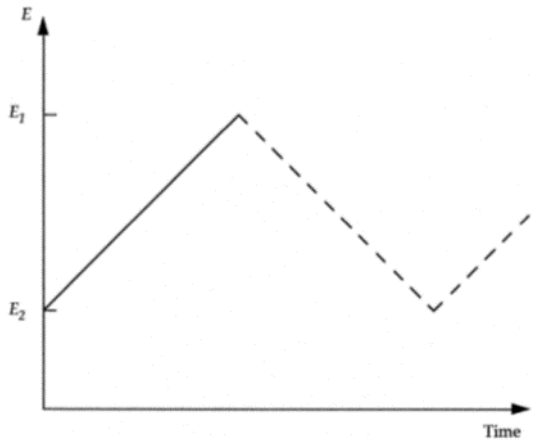

Figure 21: Potential-time profile that is used for linear-sweep voltammetry (solid line) and cyclic voltammetry.

Linear-sweep and cyclic voltammetry consist of scanning the potential between two chosen limits at a known sweep rate, υ, and measuring the current response arising from any electron transfer process. In linear-sweep voltammetry the scan terminates at the chosen and potential, E_f, whereas in cyclic voltammetry, the potential is reversed back E_f toward the starting potential E_i, or another chosen potential limit[44]. The potential limits define the electrode reactions that take place, the properties and characteristics of the electrochemical process and also gives insight into any complicating side processes such as pre- and post- electron-transfer reactions, as well as kinetic considerations. Therefore, the potential scan is normally chosen to start at a potential value where no electrode reaction occurs and swept towards positive or negative potentials to investigate oxidation or reduction processes, respectively[44]. **Figure 22** illustrates the shape of a cyclic voltammograms with an electrode of fixed area. The voltammogram is characterized by a peak potential, E_p, at which the current reaches a maximum value, and by a value of the peak current, i_p. When the reduction process is reversible the peak current is given by the relation:

$$i_p = 0.4463nFA(Da)^{1/2}C_0 \quad (21)$$

With:

$$a = nF\upsilon/RT = n\upsilon/0.026 \text{ at } 25^oC \quad (22)$$

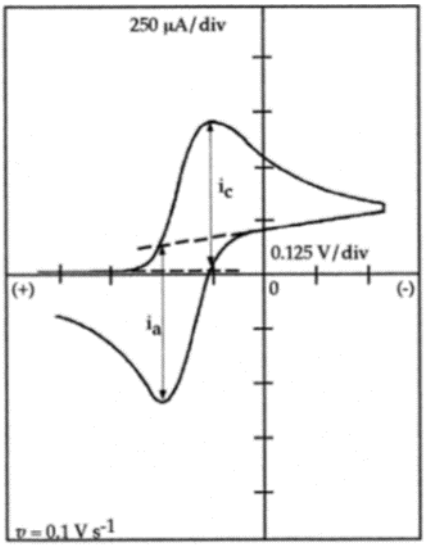

Figure 22: Linear voltage-sweep voltammogram with reversal of sweep direction to give a cyclic voltammogram.

where υ is the scan rate in volts per second. This relation results from the set of differential equations for Fick's second law of diffusion (with the appropriate initial and boundary conditions for ox and red). Thus, in terms of the adjustable parameters the peak current is given by the Randles-Sevcik equation[45]:

$$i_p = 2.69 \cdot 10^5 n^{\frac{3}{2}} A D^{\frac{1}{2}} C_0 \upsilon^{1/2} \text{ at } 25^oC \quad (23)$$

where $i_p$is in A, A is in cm^2, D is in cm^2 s^{-1}, C_0 is in mol cm^{-3}, and υ is in V s^{-1}.

For a reversible process the peak potential can be related to the polarographic half-wave potential, $E_{1/2}$, by the expression:

$$E_p = E_{1/2} - \frac{1.11RT}{nF} = E_{1/2} - 0.0285/n \text{ at } 25^oC \quad (24)$$

Another useful parameter of the voltammetric curves is the half-peak potential, $E_{p/2}$, which is the potential at which the registered current reaches half its maximum value and is used to characterize a voltammogram. For a reversible process, $E_{1/2}$ is located halfway in between E_p and $E_{p/2}$. The ratio of the peak current for the cathodic process relative to the peak current for the anodic process is equal to unity ($i_{p,c}/i_{p,a}$ =1) for a reversible electrode process. To measure the peak current for the anodic process, the extrapolated baseline, going from the foot of the cathodic wave to the extension of this cathodic current beyond the peak, must be used as a reference. For the condition

$$|E_\lambda - E_{p/2}| \geq 0.141/n \quad (25)$$

where E_λ is the extent of the voltage sweep, the difference in the peak potentials between the anodic and cathodic processes of the reversible reaction is given by the relationship

$$|\Delta E_p| = |E_{p,a} - E_{p,c}| = 0.059/n \quad (26)$$

which provides a rapid and convenient means to determine the number of electrons involved in the electrochemical reaction. For a reversible system, i_p is a linear function of $\sqrt{\upsilon}$, and E_p is independent of υ.

2.2.2 Rotating Disk Electrode (RDE) linear sweep voltammetry (RDE-LSV)

The rotating disk electrode method (RDE) has been widely used for electrochemical analysis and evaluation, as it can ensure an electrode reaction under well-described hydrodynamic condition[17]. RDE (**Figure 23**) is vertically mounted in the shaft of a synchronous controllable-speed motor and rotated with constant angular velocity (ω) about an axis perpendicular to the plain disk surface. ($\omega = 2\pi f$, where f is the rotation speed in rps)[46].

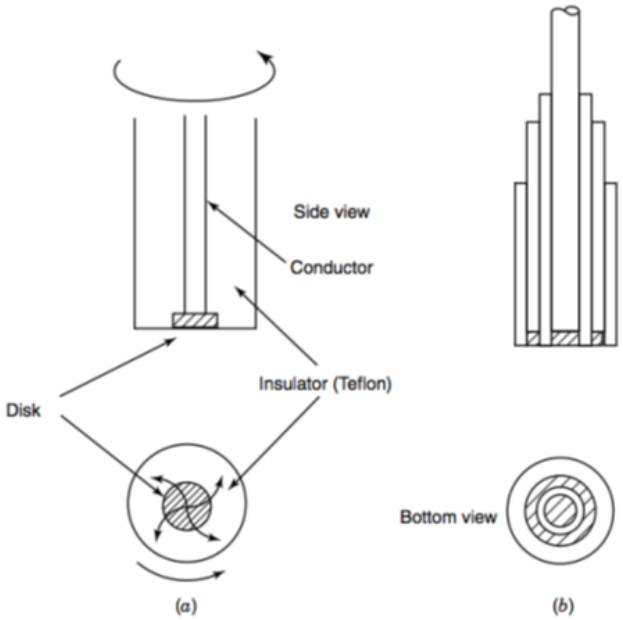

Figure 23: (a) Rotating disk and (b) ring-disk electrodes.

As a result of this motion, the fluid in an adjacent layer develops a radial velocity that moves it away from the disk centre. This fluid is replenished by a flow normal to the surface. Hence, the RDE can be viewed as a pump that draws a fresh solution up from the bulk solution. Under laminar flow conditions (usually up to about 4000 rpm), the thickness of the diffusion layer decreases with increasing electrode angular velocity according to[46]

$$\delta = 1.61 D^{1/3} \omega^{-1/2} \upsilon^{1/6} \quad (27)$$

where υ is the kinematic viscosity (defined as the viscosity divided by the density in $cm^2\ s^{-1}$). Rotation speeds of 100-4000 rpm thus correspond to δ values in the 5-50 μm range. ***Eq.(27)*** suggests that the thickness of the diffusion layer is independent of the disk diameter, that is, a uniform layer across the surface. **Figure 24** shows a typical current curve behaviour during the ORR, as we can see after the on-set potential the current go down until reach the constant value of the diffusion-limited current.

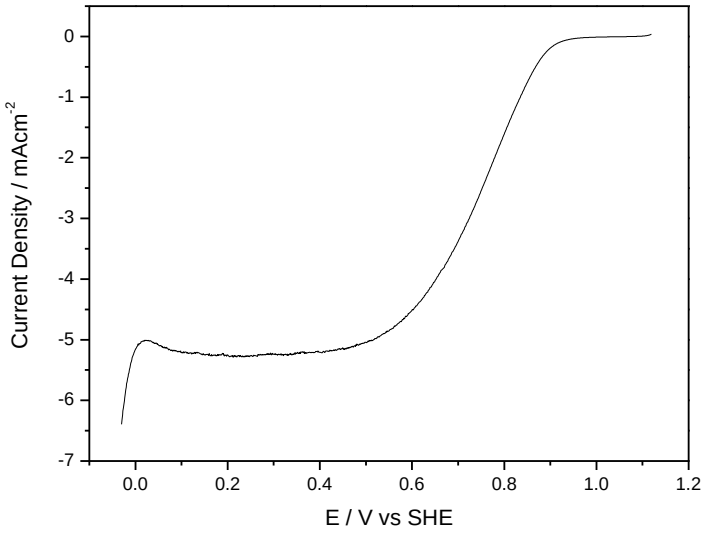

Figure 24: Typical RDE voltammograms for ORR.

The limiting current (for a reversible system) is thus proportional to the square root of the angular velocity, as described by the Koutecky-Levich equation[46]*:*

$$\frac{1}{I} = \frac{1}{I_k} + \frac{1}{I_d} + \frac{1}{I_f} = \frac{1}{I_k} + \frac{1}{C_0 B \omega^{1/2}} + \frac{L}{nF c_f D_f} \quad (28)$$

$$B = 0.62 n F {D_0}^{2/3} \upsilon^{-1/6} \quad (29)$$

$$I_k = nFkC_0 \quad (30)$$

were:

- I is the experimentally measured current (A)
- I_k is the kinetic current
- I_d is the diffusion-limited current

- I_f is inversely proportional of the diffusion resistance through surface film (Nafion)
- n is the number of electrons transferred in the half reaction (mol^{-1})
- F is the Faraday constant (96485 C/mol)
- A is the electrode area (cm^2)
- D_0 is the diffusion coefficient ($1.67 \cdot 10^{-5}$ cm^2/s for O_2)
- k is the heterogeneous electron-transfer rate constant
- ω is the angular rotation rate of the electrode (rad/s)
- v is the kinematic viscosity (cm^2/s)
- C_0 is the analyte concentration (mol/cm^3)

An increase in ω from 400 to 1600 rpm thus results in a twofold increase of the signal. A deviation from linearity of a plot of i_d vs. $\omega^{1/2}$ suggests some kinetic limitations. In addition, at very low rotation speeds (0-100 rpm), a slight upward bend is observed due to contribution by natural convection. The voltammetric wave has a sigmoidal shape, independent of ω. For quasi-reversible systems the limiting current is controlled by both mass transport and charge transfer[46], in the limit of purely kinetically controlled process ($k < 10^{-6}$ m s^{-1}) the current becomes independent of the rotation speed:

$$i_d = nFAkC \qquad (31)$$

Overall, the RDE provides an efficient and reproducible mass transport and hence the analytical measurement can be made with high sensitivity and precision. Such well-defined behaviour greatly simplifies the interpretation of the measurement. The convective nature of the electrode results also in very short response times. Sinusoidal or square-wave modulations of the rotation speed are particularly attractive for this task[45]. The rotation-speed dependence of the limiting current ***Eq. (28)*)** can also be used for calculating the diffusion coefficient or the surface area[47]. An extension of the RDE involves an addition of a concentric-ring electrode surrounding the disk (and separated from it by a small insulating gap). The resulting rotating ring-disk electrode (RRDE), shown in **Figure 23**, is extremely useful for elucidating various electrode mechanisms (through generation and detection of reactions at the disk and ring, respectively). Because of the electrode rotation, the product of the disk reaction is hydrodynamically transported across the insulating gap toward the ring where it can be detected[48]. Such "collection" experiments rely on measurements of the collection efficiency (N), which is the ratio of the ring and disk currents:

$$N = -I_r/I_d \quad (32)$$

and corresponds to the fraction of the species generated at the disk that is detected at the ring. (The negative sign arises from the fact that the currents pass in opposite directions.) Hence, the "collection" current is proportional to the "generation" current. The value of N reflects the dimensions of the electrodes and the gap. Such experiments are particularly useful for detecting short-lived intermediate species, generated at the disk and consumed before reaching the ring. Such consumption during the disk-to-ring transition time results in current ratios smaller than the "geometric" N[45]. Recently, with the development of PEM fuel cells, RDE has been widely used to screen the activity of some electrocatalysts (e.g., Pt-based, non-noble catalysts) toward fuel cell reactions, such as oxygen reduction, hydrogen oxidation, methanol oxidation, and CO tolerance in simulated fuel cell environments[17].

2.2.3 Polarization Curves – Voltage vs. Current Density Relationship

Polarization curves (plot of cell voltage vs current density) are the key performance indicators used to evaluate and compare the performances of the fuel cell. Polarization curve can differ significantly from one technology to another, depending on different parameters (mainly fuel, mass, flow, operating temperature and pressure)[49]. When an external resistance, commonly referred to as "load", is applied to the cell, non-equilibrium exists and a net current flows through the load. The net rate of an electrochemical reaction is proportional to the current density which is defined as the current of the electrochemical system divided by the active area of the device. The cell voltage becomes smaller as the net reaction rate increases because of irreversible losses. **Figure 25** shows a typical polarization curve for a fuel cell with negative entropy of reaction, showing five regions of interest labelled 1-5[3]:

- The losses in region 1 are denominated by the activation (kinetic) overpotential at the electrodes.
- The losses in region 2 are denominated by the ohmic polarization of the fuel cell. This includes all electrical and ionic conduction losses through the electrolyte, catalyst layers, cell interconnects, and contacts.
- The losses in region 3 are denominated by the concentration polarization of the fuel cell, caused by mass transport limitations of the reactants to the electrodes.
- The losses in region 4 represent the departure from the Nernst thermodynamic equilibrium potential. This loss can be due to undesired species crossover through the electrolyte, internal currents from electron leakage through the electrolyte, or other contamination or impurity

- The losses in region 5 represent the departure from the maximum thermal voltage, a result of entropy change which cannot be engineered[3].

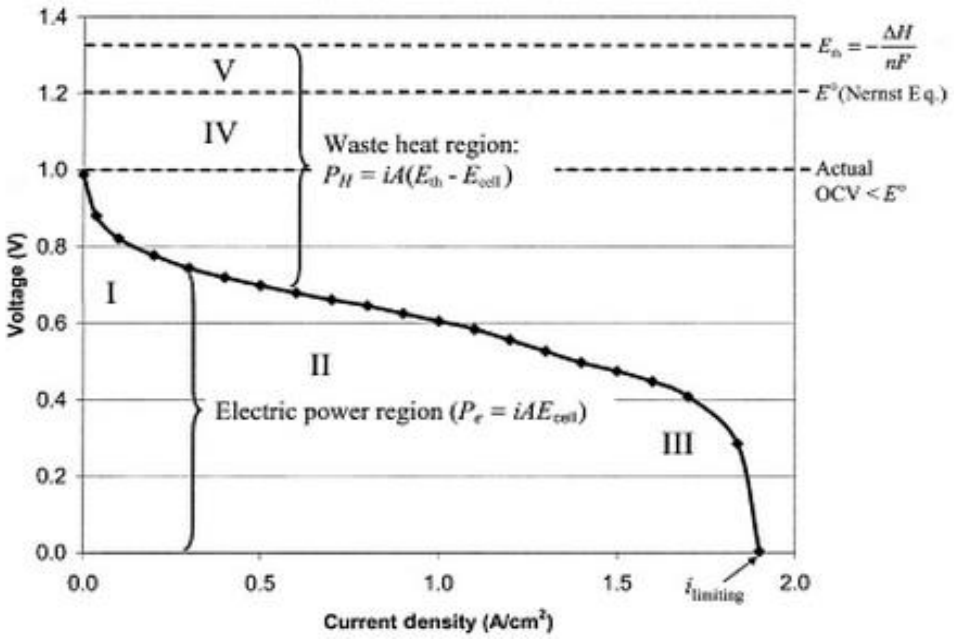

Figure 25: Typical polarization curve for fuel cell with significant kinetic, ohmic, concentration, and crossover potential losses.

Deviation between potential and the polarization curve provides a measure of a fuel cell efficiency. The voltage-current density relationship for a given fuel cell and operating conditions is a function of the kinetic, ohmic, and mass transfer resistances. Although the discussion here is based on H_2/O_2 PEM fuel cell, the same performance parameters are associated with all type of fuel cells; only the relative influence and contribution of each parameter changes with the fuel cell type.

2.2.4 Electrochemical Impedance Spectroscopy (EIS)

Electrochemical reactions consist of electron transfer at the electrode surface. These reactions mainly involve electrolyte resistance, adsorption of electroactive species, charge transfer at the electrode surface, and mass transfer from the bulk solution to the electrode surface. Each process can be considered as an electric component or a simple electric circuit. The whole reaction process can be represented by an electric circuit composed of resistance, capacitors, or constant phase elements combined in parallel or in series[50]. These are the principles on which the electrochemical impedance spectroscopy is based. The impedance experiments are easy to perform and spectra are readily recorded using computer-controlled instruments[51]. Electrochemical impedance spectroscopy involves imposing a small sinusoidal (AC) voltage or current signal of known amplitude and frequency – the perturbation – to an electrochemical cell and monitoring the AC amplitude and phase response of the cell (**Figure 26**). The AC perturbation is typically applied over a wide range of

frequencies, from 10 kHz or greater to less than 1 Hz, hence the name impedance spectroscopy. The ratio and phase-relation of the AC voltage and current signal response is the complex impedance, Z (ω). The results of an impedance spectroscopy experiment is a rich data set from which many properties of the electrochemical cell may be extracted via application of equivalent circuit models[52]. Properties of the electrochemical system commonly evaluated using impedance spectroscopy include ohmic (bulk) resistance, electrode properties such as charge transfer resistance and double layer capacitance, and transport (diffusion) effects. The impedance is the ratio between the AC voltage and the current output.

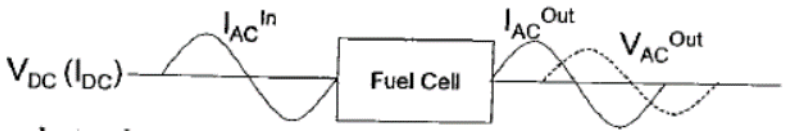

Figure 26: Schematic of an electrochemical impedance spectroscopy.

A sinusoidal current signal of amplitude I_{AC} (amps) and frequency ω (radians/seconds) can be defined:

$$I(\omega) = I_{AC} \cdot \sin(\omega \cdot t) \quad (33)$$

where t is time (s). The output AC voltage signal from the electrochemical cell can be defined:

$$V(\omega) = V_{AC} \cdot \sin[(\omega \cdot t) - \theta] \quad (34)$$

where V_{AC} is the amplitude for the output voltage signal (volts) and θ is the phase angle (radians). The phase angle is the difference in the phase of a sinusoidal voltage and current signals. In the case of AC signal, the "resistance" of circuit of the electrochemical device which is not purely resistive will be function of the frequency of oscillation of the input signal. Ohm's Law for the AC case is expressed:

$$Z(j\omega) = V(j\omega) / I(j\omega) \quad (35)$$

where Z (jω) is the complex impedance (Ω) and j is the imaginary operator,

$$j \equiv \sqrt{-1} \quad (36)$$

Eq.(35) indicates that impedance is a complex value. That is, it can take on both real and imaginary components. Note that the imaginary component of the impedance is a real measurable quantity: "j"

allows description of the out-of-phase component of the impedance. The complex relationship of impedance is implicit so Z(jω) is normally written as Z(ω). Although one can think of impedance as "resistance" to current, it is more general than that because it takes into account the phase difference between voltage and current. ***Eq.(35)*** also indicated that impedance depends on the frequency at which it is measured. Z can change as the frequency of the AC signal changes. Frequency in cycles per second, f (Hz = 1/s), is obtained through the relation:

$$\omega = 2\pi \cdot f \qquad (37)$$

Eq.(35) can be written in complex notation:

$$Z = Z' + Z'' \qquad (38)$$

where,

$$Z' = Re(Z) = |Z|cos\theta \qquad (39)$$
real (in-phase) component of impedance

$$Z'' = Im(Z) = |Z|sin\theta \qquad (40)$$
imaginary (out-of-phase) component of impedance

$$|Z| = \sqrt{(Z')^2 + (Z'')^2} \qquad (41)$$
magnitude of impedance

and

$$\theta = tan^{-1}(Z'/Z'') \qquad (42)$$

In the impedance spectroscopy experiment, the frequency of the AC perturbation is swept over a range, from ~ 10 kHz to less than 1 Hz and the impedance is evaluated as a function of frequency to evaluate the properties of the electrochemical system under investigation. Usually the real (Z´) and imaginary (Z´´) parts of the impedance are plotted as a function of frequency.

The most common circuit elements, the equations for their current versus voltage relationships, and their impedances are listed in **Table 1**.

Table 1: Common circuit elements and correspondent I vs. E relationships and impedance equations.

Component	***Current vs Voltage***	***Impedance***

Resistor	E=IR	Z=R
Inductor	E=L·dI/dt	Z=j·ω·L
Capacitor	I= C·dE/dt	Z=I/j·ω·C

Notice that the impedance of a resistor is independent of frequency and has no imaginary component. With only a real impedance component, the current through a resistor stays in phase with the voltage across the resistor. The impedance of an inductor increases as frequency increases. Inductors have only an imaginary impedance component. As a result, the current through a capacitor is phase shifted -90° with respect to the voltage. The impedance versus frequency response of a capacitor behaves in an opposite way to that of an inductor. A capacitor's impedance decreases as the frequency is raised. Inductors also have only an imaginary impedance component. The current through a capacitor is phase shifted 90° with respect to the voltage[53].

Simple equivalent circuit models is employed to model the impedance data when the cell is operated with H_2 fuel and either air or pure O_2 oxidant under humidified conditions[8].

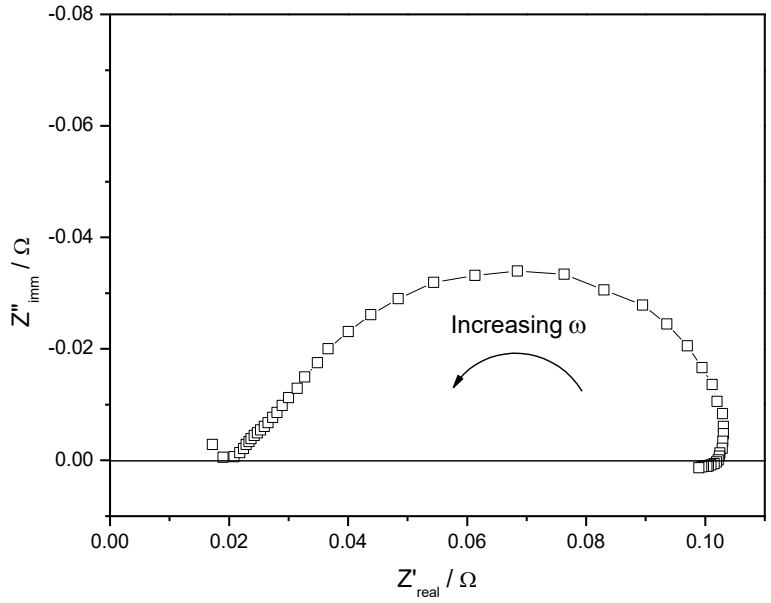

Figure 27: Impedance spectra for H_2/O_2 PEM fuel cell as a function of current density at 0.8V and 100% RH (70/70/70).

Figure 27 shows that for H_2/O_2 case, the spectra at low current densities consisted of a single high frequency loop displaced along the Z' axis. This impedance behaviour is consistent with a resistor in series with a parallel resistor-capacitor combination. The Warburg impedance is the electrical analog of diffusion processes in the absence of migration.

A suitable equivalent circuit for H_2/O_2 impedance spectra at moderate current densities is given in **Figure 28**. This electrical analog consists of a resistance representing the total non-electrode cell ohmic resistance (R_{ohm}) in series with a cathode charge-transfer resistance ($R_{ct,c}$) that is in parallel with a capacitive-like element representative of the electrode double layer (CPE)[8].

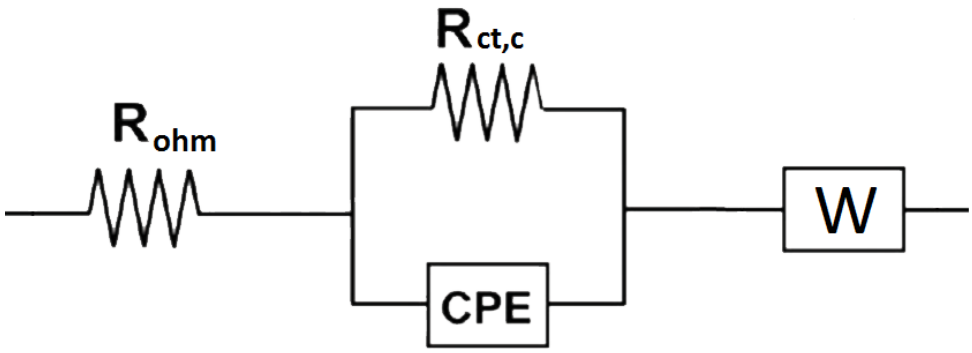

Figure 28: Equivalent circuit models used to fit the impedance spectra for a PEMFC operating at fully humidified condition[8].

Recall that the order of series elements in the equivalent circuit does not affect the impedance spectrum.

2.3 Apparatus

- SEM experiments were performed with Leo 1430 (Zeiss).
- The XRD spectra were recorded on sample powders. X-ray diffraction (XRD) data were recorded using an automated diffractometer equipped by; HV power supply Italstructures, X-ray lamp Philips with Mo anode and CPS180 position sensitive detector with a gas mixture of Kr / CO_2. Divergence of the beam controlled by fissures + soller slits of Huber.
- The IR spectra of our samples were recorded in the ATR mode (Attenuated Total Reflectance), with PerkinElmer Spectrum 100 Series FT-IR spectrometer.
- Electrochemical experiments were carried out with the CH Instruments (Austin, TX) model 832, in a Pine AKCELL3 three-electrode cell. The working electrode (RRDE) was a PINE special MT29 series tips with Glassy carbon Rings (collection efficiency: 37%; disk area: 0.2475 cm^2) driven by a Pine rotator 636 ring-disk electrode system (Pine Instruments, USA). The reference electrode was K_2SO_4 saturated Hg/Hg_2SO_4 (MSE), and Pt flag as counter electrode. We have transformed all the potentials with a factor of + 0.65 so all the potentials are reported versus the standard hydrogen electrode (SHE). The MSE reference electrode was used to avoid possible contamination of chloride come from electrolyte solution. Two supporting electrolytes of 0.1 M $HClO_4$ and 0.5 M H_2SO_4 in ultra-pure water was used. All electrochemical analysis are made at 25ºC with Haake F3-K Refrigerated Circulating Water Bath.
- A Fuel Cell of 5 cm^2 area (triple-serpentine cell, model 05-02 from Electrochem. Inc), controlled by a Scribner Associated 890CL fuel cell test system, was used for the fuel cell experiments. For MEA testing pure Hydrogen has been used at anode (100 ml/min) and pure Oxygen at cathode (200 ml/min). The gas pressure was maintained constant at 2 bar. All the potentials are reported versus the standard hydrogen electrode (SHE).

3. EXPERIMENTAL PROCEDURES

3.1 POMs salt synthesis

Three different salts ($Cs_{2.5}H_{2.5}PMo_{10}V_2O_{40}\cdot 8H_2O$, $Cs_3H_2PMo_{10}V_2O_{40}\cdot 8H_2O$ and $Cs_{3.5}H_{1.5}PMo_{10}V_2O_{40}\cdot 8H_2O$) were prepared using the following procedure. An aqueous solution of Cs_2CO_3 was added drop-wise to the PVM ($H_5PMo_{10}V_2O_{40}\cdot 8H_2O$) solution (in u.p. water) at 50°C under vigorous stirring. The fine suspension was held under stirring at 50ºC for 1h and the stir was maintained overnight at r.t. Subsequently the mixture is filtered with a under vacuum filter system using a hydrophilic filter. The final product was dried overnight in oven at 50°C. The ratio PVM–cesium carbonate was regulated in order to obtain the desired stoichiometry. When drying process is done, the product is ground in a mortar and weighed. Finally, the compound is stored in a 4cc vial, under vacuum desiccator.

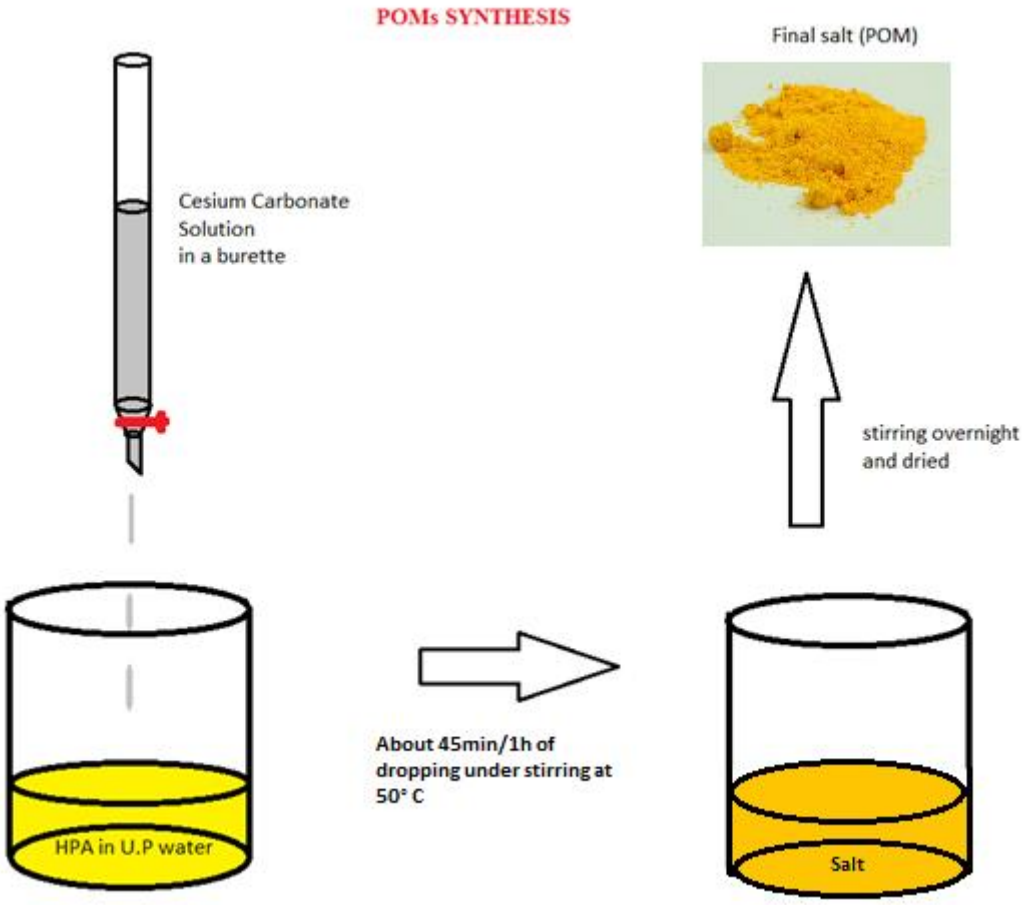

Figure 29: Schematic representation of POMs salt synthesis.

3.2 Catalytic layer preparation

The procedure for catalytic layer preparation was to mix in a vial an amount of POM salt with Pt/Vulcan and 985 µl of isopropanol. The mixture was sonicated for 10 seconds in a water bath and for 30 min with ultrasonic processor in ice bath. Only after, 15 µl of Nafion solution were added and the new mixture was put under stirring for 30 min. The weights of salt and Pt/Vulcan are calculated in according to the Pt loading wanted on the electrode. In this thesis usually 10/15 µg Pt/cm^2 are deposited on electrode surface. The Pt/POM/pure Nafion 1:1:1 mass ratio is used. Before the experiments, the working electrode is cleaned with Al_2O_3, with particle sizes of 0.05 µm. An amount of 4 µl of the prepared ink is deposited on the electrode surface trough a Hamilton 701n 10 µl syringe and let dry for 30 minutes in air.

For Fuel Cell analysis inks with mass ratio Pt/C : POM : pure Nafion of 2:1:1 are prepared. Pt loading is typically 0.2 mg/cm^2 for modified cathode.

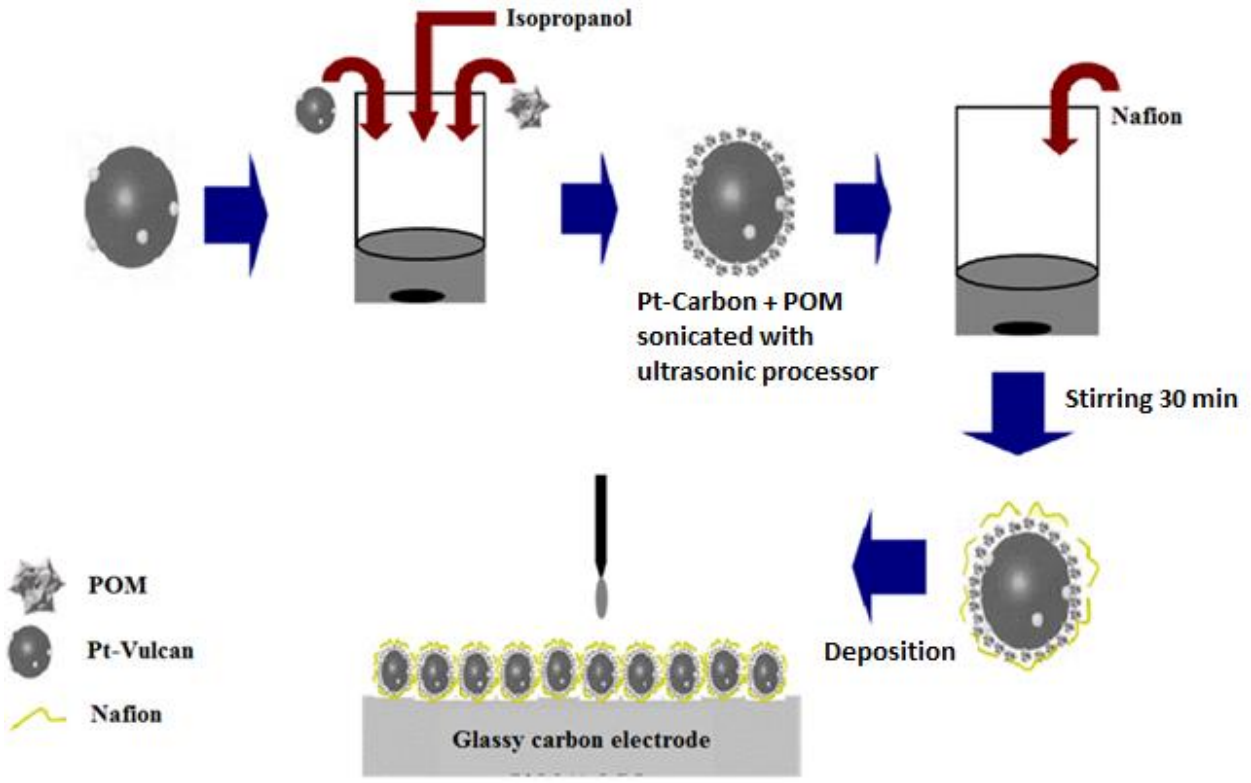

Figure 30: ink preparation scheme by mixing method.

3.3 Electrochemical analysis procedures

3.3.1 Cyclic Voltammetry of Pt-free POMs

This analysis is performed to obtain information on the redox reactions that occur on the polyoxometalates. Ink is prepared using the procedure reported in *Section 3.2* mixing the POM with only carbon support (Vulcan XC-72R). Before every test the system is saturated with Nitrogen (N_2) for at least 30 minutes, afterwards cyclic voltammetry at 10mV/s is registered. H_2SO_4 0.5 M is used as electrolyte.

3.3.2 HOR (Hydrogen Oxidation Reaction)

This analysis is performed in order to obtain active area value for each sample, achievable performing a cyclic voltammetry in saturated hydrogen atmosphere. Before every test the system is saturated with Nitrogen (N_2) for at least 30 minutes. The electrode is activated by almost 30 minutes cycling in N_2-saturated solution at 50mV/s in order to obtain clean Pt surface. Immediately after the system is purged with pure Hydrogen (H_2) until saturation is obtained; afterwards the electrode is cycled until stabile voltammogram is obtained. During the experiment the temperature of the system is kept at 25ºC. $HClO_4$ 0.1 M is used as electrolyte.

3.3.3 ORR (Oxygen Reduction Reaction)

All ORR are made after HOR cycling at least 30 minutes in pure oxygen (O_2) saturated solution, until a stabile voltammogram is obtained. During the experiment the cell is kept in Oxygen atmosphere. A cyclic voltammetry (CV) is performed during the electrode rotation at 2500, 2000, 1600, 1200, 900, 600 and 400 rpm following the order. In the end a second control test is performed at 1600 rpm to check if there are any different with the previous. Finally a LSV at 1600 rpm is made after 30 minutes of nitrogen flux to obtain the background current. Between each experiment a CV is performed until a stable voltammogram obtained. The temperature of the system is kept at 25ºC. $HClO_4$ 0.1 M is used as electrolyte.

3.3.4 CO Stripping

For CO stripping voltammetry experiments, CO adsorption is performed by bubbling CO gas (technical purity 99%, Airgas) into electrolyte for 5 minutes and 0.1V vs RHE applied for 200 seconds. The electrolyte solution is then purged with nitrogen gas (high purity 99.9%, Airgas) for 30

minutes to remove dissolved CO. Finally CO stripping is carried out by 4 cyclic voltammetries at 20 mv/s. All measurements are made at 25ºC. $HClO_4$ 0.1 M is used as electrolyte.

3.3.5 Fuel Cell analysis

The inks are prepared by following the same procedure reported in *Section 3.2*. The slurry is brushed on the gas diffusion layer (GDL) as uniformly as possible to obtain a homogenous thickness throughout all the electrode surface. The membrane electrode assembly (MEA) has been prepared by sandwiching a Nafion® 112 membrane of 60 μm thickness (Ion-Power, Inc.), pre-treated with H_2O_2 and H_2SO_4 to remove organic and inorganic impurities[54], between anode and cathode at T = 120 °C for 3 minutes. Analysis in fuel cell are performed at different percentages of relative humidity (% RH). Temperatures of cell and of feed gases are hereafter specified as TA/TM/TC. TA and TC are anode and cathode feed gas temperatures, respectively, while TM is cell temperature (°C). The first step is activation process achieved feeding fully humidified oxygen and hydrogen at cathode and anode, respectively, with 100% RH (T = 70/70/70 °C) until stable polarization curve is obtained (the process need about 3h). Following analysis with 100% RH (T = 70/70/70 °C), 62% RH (T = 60/70/60 °C) and 17% RH (T = 40/70/40 °C), are performed.

3.4 Reagents

- Vulcan XC-72R (E-Tek Division);
- Cesium carbonate, Cs_2CO_3 (Sigma-Aldrich ≥99.00%);
- Platinum, nominally 40% on carbon black HiSEPC 4000 (Alfa Aesar);
- Phosphovanadomolibdic acid PVM-2-10; (Nippon Inorganic Colour & Chemical CO., LTD.);
- LIQUION Solution LQ-1105 1100EW 5% wt. (NAFION);
- Sulphuric acid 99.999%, H_2SO_4 (Sigma-Aldrich);
- Perchloric acid 70%, redistilled, 99.999% metal basis, $HClO_4$ (Sigma-Aldrich);
- 2-Propanol ≥99.8% (Sigma-Aldrich);
- Compressed hydrogen gas (Air Liquide), H_2, impurity: H_2O < 3ppm; O_2 < 2ppm; CnHm < 0.5ppm;
- Compressed oxygen gas (Air Liquide), O_2, impurity: H_2O < 3ppm; CnHm < 0.5ppm;
- Compressed nitrogen gas (Air Liquide), N_2, impurity: H_2O < 3ppm; O_2 < 2ppm; CnHm < 0.5ppm;
- Compressed carbon monoxide gas (Air Liquide), CO, technically pure.

All reaction solutions and electrolytes are prepared with distilled water that was further purified with Millipore Milli-Q nanopure water of resistivity ≈ 17 M Ω cm. All the chemicals are of analytical grade purity and were used without further purification.

4. RESULTS AND DISCUSSION

4.1 POM 2.5-2-10 characterization

4.1.1 Physical characterizations

4.1.1.1 SEM

Figure 31 shows the micrograph of the starting HPA ($H_5PMo_{10}V_2O_{40}\cdot 8H_2O$) on which morphology with different arrays of big crystals (1-10 µm) is observed.

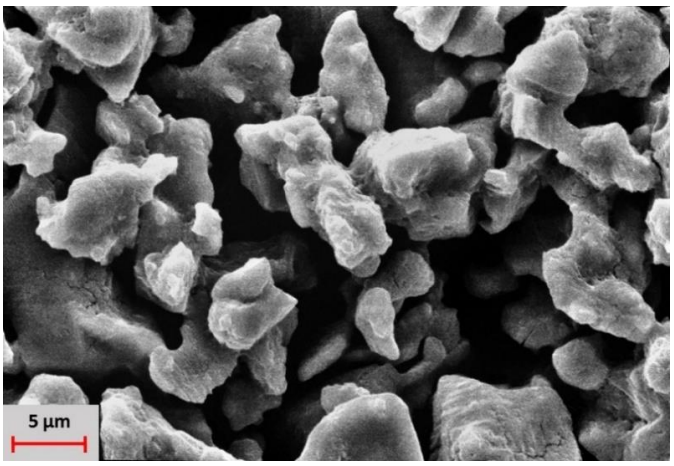

Figure 31: SEM micrograph of PVM2-10 (2500x magnification).

The micrographs of Cs salt (POM 2.5-2-10) show different type of agglomerates of small apparently cubic nanocrystals grains (50-500 nm) that appear to be more dispersed in contrast with starting HPAs; this suggest a morphological modification as a consequence of the reaction (**Figure 32**).

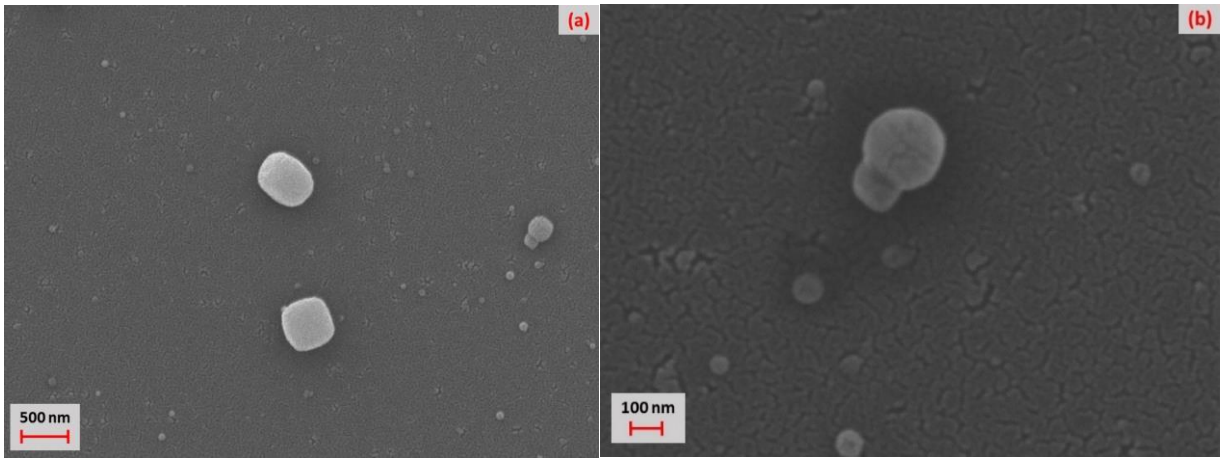

Figure 32: SEM micrographs of POM 2.5-2-10: a) 20000x magnification; b) 60000x magnification.

4.1.1.2 XRD

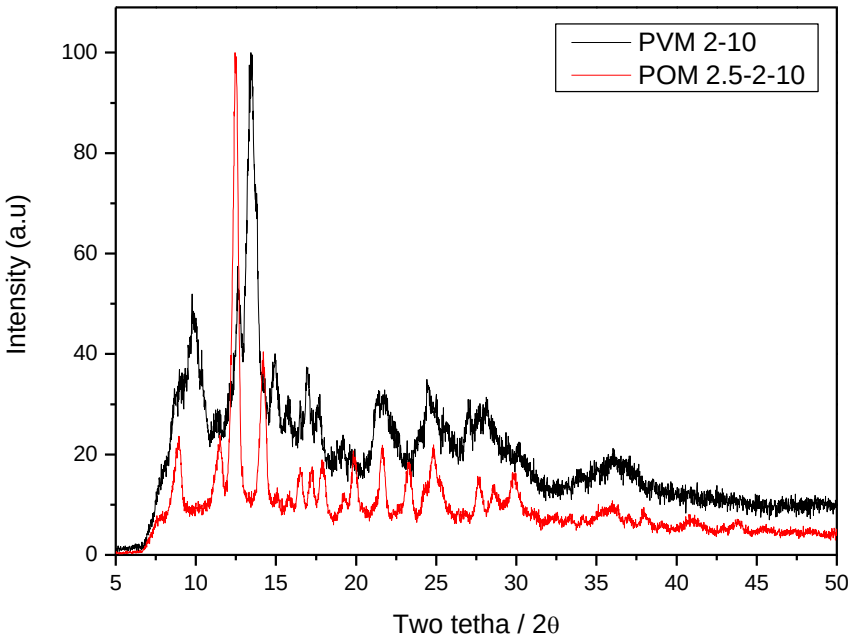

Figure 33: XRD analysis of POM 2.5-2-10 (red) compared with that of PVM 2-10 (black).

Figure 33 shows XRD pattern of starting heteropolyacid PVM 2-10 compared with that of POM 2.5-2-10. PVM 2-10 exhibits a XRD pattern which are in agreement with that reported for Keggin-type heteropolyacid[55]. XRD pattern of POM 2.5-2-10 is very similar to the reference acid, meaning that after the reaction POM salt maintains the Keggin-type structure. Anyway, there are shifts toward lower 2θ values for POM 2.5-2-10 due the introduction of larger Cs^+ cation**,** into a heteropolyacid compound to replace H^+ will greatly influence its tertiary structure, leading to the formation of micropores and mesopores and the significant increase in specific surface area[56]. Moreover, we can see that peaks for the POM salt are more defined than those of the acid, meaning a more ordered crystal lattice.

4.1.1.3 IR spectroscopy

Figure 34 shows IR spectroscopy comparison between the starting heteropolyacid (PVM 2-10) and the POM 2.5-2-10 salt. IR spectra of PVM 2-10 shows the characteristic bands of Keggin structure[57], in the region between 800-1200 cm^{-1}. The bands typical of the Keggin structure are:

- P-O bond Stretching at 1056 cm^{-1};
- Mo = O bond Stretching at 955 cm^{-1};
- Mo-O-Mo bond Stretching at 870 cm^{-1} and 730 cm^{-1}.

The band at 741, 858, 955, 1058 cm^{-1} can be confidently attributed to Mo-O-Mo bridge stretching, Mo = O bond asymmetric stretching and P-O bond stretching of PO_4 tetrahedron. The pattern of the salt is very similar the one of the heteropolyacid but there is a presence of shoulder peak at around 1000 cm^{-1}. The asymmetry for P-O bond vibration (1058 cm^{-1}) and Mo = O bond asymmetric stretching (955 cm^{-1}) indicates the presence of Vanadium atoms in the structure, that replace one or more Mo atoms. This is confirmed by literature that reported the stretching of V = O at 1070 cm^{-1}.[58] Thanks to the presence and distribution of Cs^+ cation in the material, we can see the shift of the IR salt peaks respect to starting PVM.

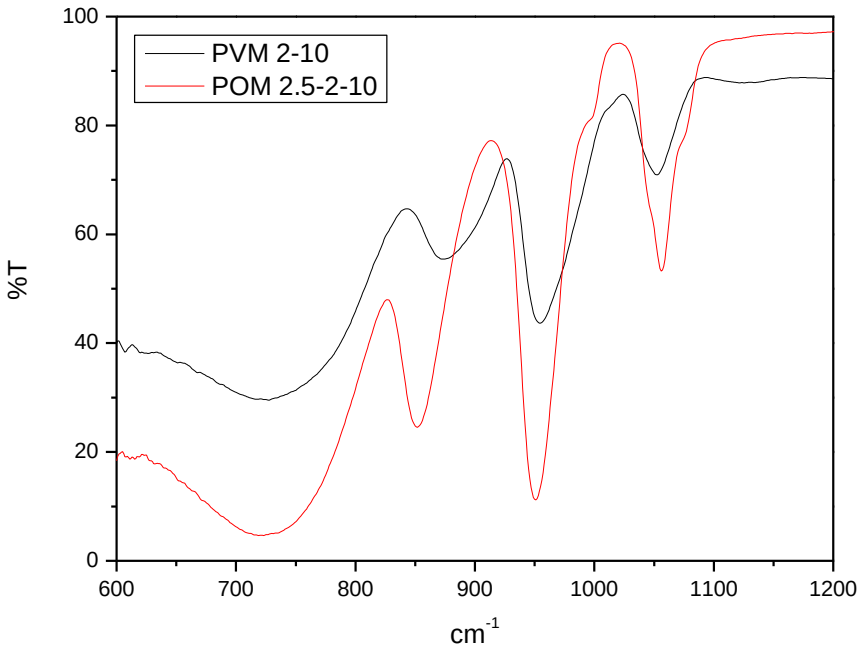

Figure 34: IR spectra of PVM 2-10 (black) and POM 2.5-2-10 (red).

4.1.2 Electrochemical characterizations

4.1.2.1 Cyclic voltammetry

In **Figure 35** is reported the cyclic voltammogram for a solution 10^{-3} M of acid PVM 2-10. Two redox couples involving Mo^{6+} that undergoes several subsequent reduction steps together with H^+ uptake are shown. Wlodarczyk et.al[59] studied a similar system like polymolybdate anion, assigning the redox couples to three consecutive redox processes each involving two-electrons:

$$PMo_{10}{}^{VI}V_2O_{40}{}^{5-} + ne^- + nH^+ \Leftrightarrow H_nPMo_n{}^{V}Mo_{10-n}{}^{VI}V_2O_{40}{}^{5-} \quad (43)$$

where n is equal to 2, 4 or 6. The presence of Vanadium that partly substitutes Molybdenum only slightly shifts the peaks towards more positive potential.

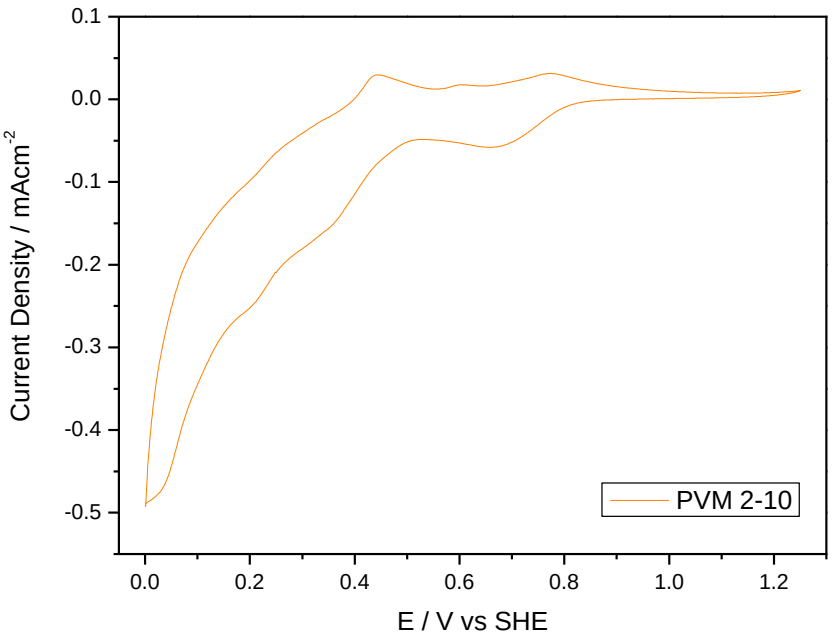

Figure 35: Cyclic voltammetry at GC electrode of PVM 2-10 solution. Electrolyte: H_2SO_4 0.5M. Scan rate: 10mV/s.

Because of the presence of the Vanadium, the heteropolyacid undergo hydrolysis in aqueous solution[60], therefore the adsorption on the GC electrode has been carried out to better identify the peaks corresponding to the various processes (**Figure 36**). The shape is maintained but a new redox couple at about 0.2 V vs RHE is observed, which can be attributed to the third Mo redox process.

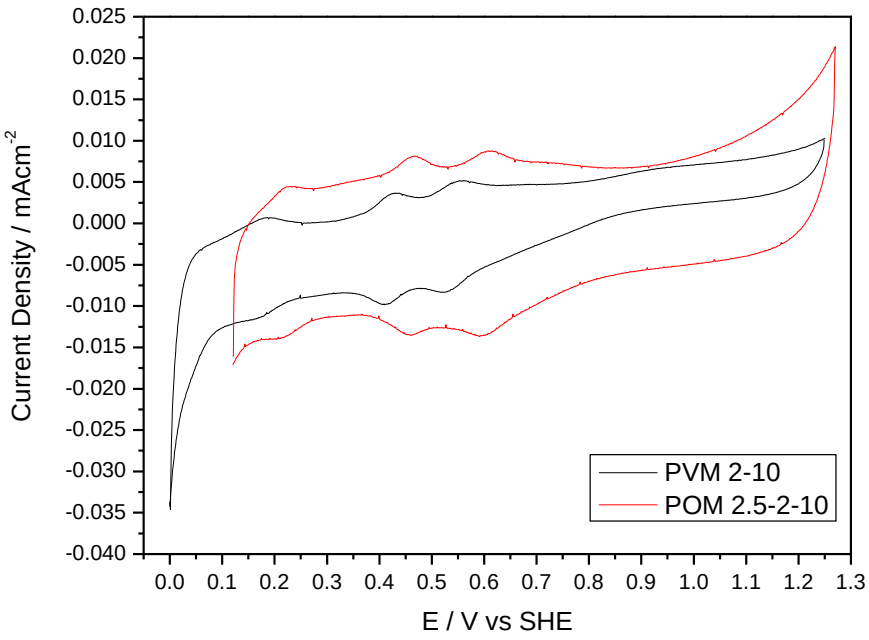

Figure 36: Cyclic voltammetry at GC electrode of PVM 2-10 (black) and Pt-free POM 2.5-2-10 coated electrode (red). Electrolyte: H_2SO_4 0.5M. Scan rate: 10mV/s.

In **Figure 36** cyclic voltammetry of POM 2.5-2-10 is also reported. The shape is maintained between acid and salt but a shift toward positive potential is observed. According with the literature[61], we can explain this shift with the presence of the Cs^+ cation in the Kegging structure that goes to affect the thermodynamics of redox processes involved.

4.1.2.2 Active area

Figure 37 shows the cyclic voltammograms of catalytic layers (Pt/POM 2.5-2-10) with L_{Pt} = 10 and 15 µg /cm^2 compared with the reference unmodified commercial ink (Pt/C 40%) with L_{Pt} = 15 µg/cm^2. In the voltammograms the peaks of Cs salts cannot be distinguished due to overlapping with Hydrogen adsorption process on Pt in the region 0-0.3 V. A redox couple around 0.45V appears for the modified layer corresponding to the salts reduction process.

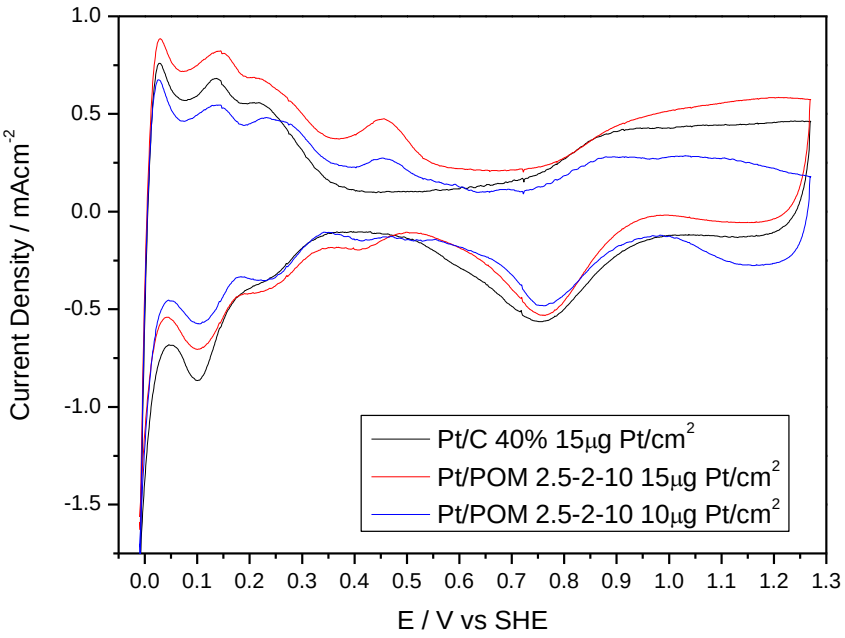

Figure 37: Cyclic voltammograms recorded in 0.1 M $HClO_4$ solution saturated with hydrogen. Scan rate: 50mV/s.

The reduction peak visible at 0.75 V, corresponding to the reduction of Pt-oxo species, tend to shift to higher potentials respect to unmodified layer. This behaviour indicates a facilitate adsorption and reduction of Oxygen molecules during electrocatalysis[62].

Table 2: Comparison between calculate active area and R factor of layer with POM 2.5-2-10 mixed with Pt/C 40%.

INK	L_{Pt}	Calculate Active Area	Roughness Factor
Pt/C 40% Alfa Aesar	15 µg Pt/cm^2	2.50 cm^2	10.12
Pt/C 40% + POM 2.5-2-10	15 µg Pt/cm^2	2.38 cm^2	9.63
Pt/C 40% + POM 2.5-2-10	10 µg Pt/cm^2	1.67 cm^2	6.74

As we can see from **Table 2**, the layer with POM 2.5-2-10 at L_{Pt} = 15 µg Pt/cm^2 presents active area value similar to the unmodified Pt/C with the same L_{Pt}. The POM 2.5-2-10 layer at L_{Pt} = 10 µg Pt/cm^2 present a value slightly less, but this drop is easily explained by the 33% less of Pt used; anyway there is no performance loss in comparison to the decrease of Pt loading. However, we must consider the

uncertainty in the calculation of the active area, due to the Cs peaks around 0.45 V that overlap those of the Hydrogen redox processes.

4.1.2.3 ORR

In **Figure 38(a)** we can see a shift of ORR onset potential toward more positive value for both modified layers respect to commercial Pt/C 40%. The layer with L_{Pt} = 15 μg/cm^2 shows, in the first part, a comparable onset potential; while in the final part of the curve is possible to see a higher slope. Higher shift is observed for the layer with L_{Pt} = 10 μg/cm^2. This shift indicates a lower activation energy due to a more favourable kinetics for the ORR. This suggests that the presence of insoluble salt in the INKs improves the catalytic activity of the Pt particles. Several factors such as porosity, surface area, Pt particles dispersion, H^+ availability from POM matrix, and amount of conductive agent may improve the catalytic activity.

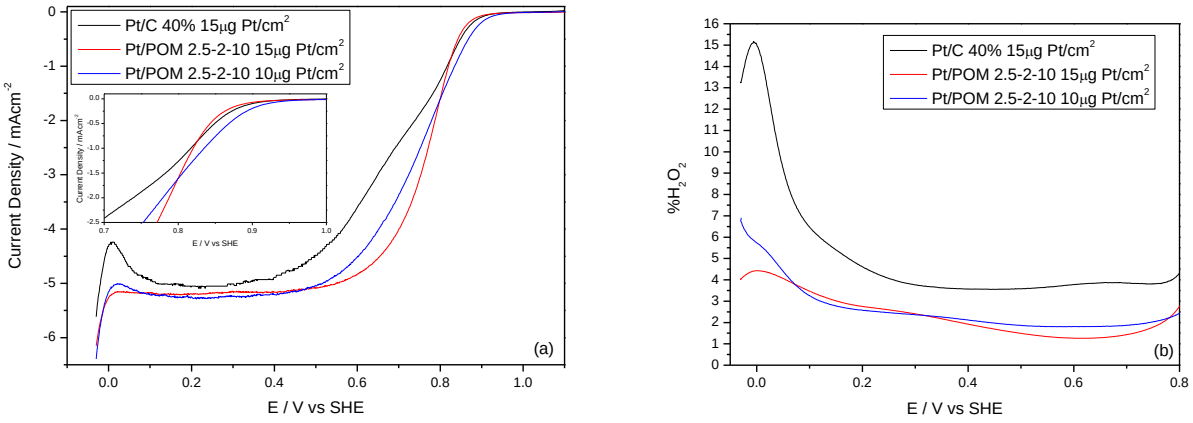

Figure 38: (a) comparison of selected RDE voltammograms at 1600 rpm rotation speed for ORR of Pt/C and Pt/POM electrodes. Insert: detail of the onset potential; (b) disk currents measured at E_{ring} = 1.2 V vs RHE and 1600 rpm. Electrolyte: $HClO_4$ 0.1M, scan rate: 5 mV/s.

Moreover, in **Figure 38(a)** we can see the non-linear trend of the current for the unmodified layer caused from a high production of peroxide during the reaction. This can be confirmed from the **Figure 38(b)**, where we can see at 0.6 V (i.e. the potential relevant to fuel cell cathodes) the calculated H_2O_2 is 3.8% for the Pt/C 40 %, compared with about 1% for both modified layers. This means that for the Pt/POM electrode, the reduction of O_2 tends more towards four-electron mechanism. Peroxide formation increases significantly in the H_{upd} region, as revealed by the decrease of the disk current density at very low potentials. As a consequence, at potentials lower than 0.6V, the calculated value of formed H_2O_2 is increased until 4-7% for Pt/POM, while it increases about 15% for Pt/C. Fractions of H_2O_2 are computed from the disk and ring currents using the equation: ($XH_2O_2 = (2I_R/N)/(I_D + I_R/N)$), where I_D and I_R are the disk and ring currents and N is the collection efficiency)[63]. We can

thus hypothesize better electrode performance in the case of real Fuel Cell using Pt/POM with lower Pt loading.

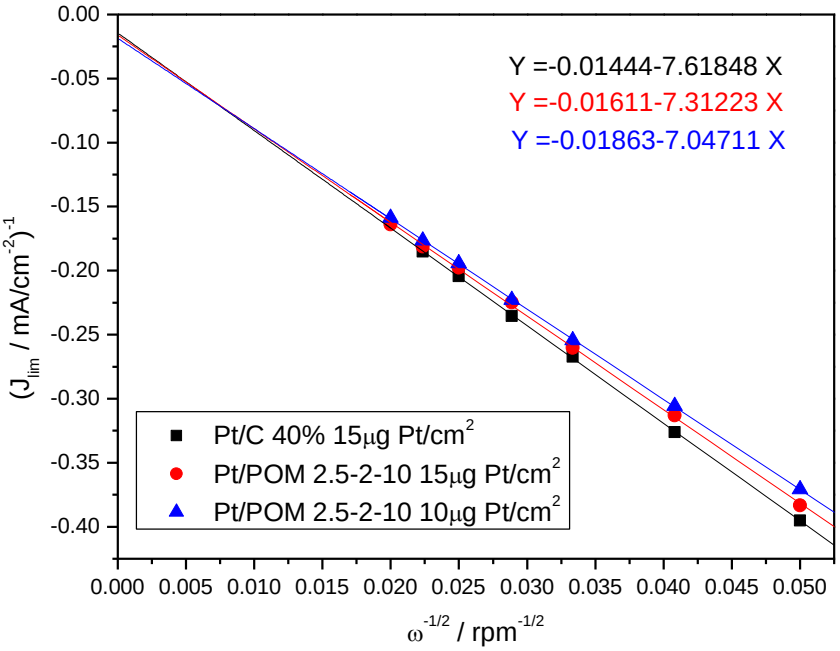

Figure 39: Comparison of Koutecky-Levich graphs of analysed catalytic layers, obtained using the data in Figure 38(a) take at 0.3V.

From Koutecky-Levich plots (**Figure 39**) is possible to see the dependence of RDE limit current versus square-root of scan rates. The decrease of K-L plot slope means a more favourable process in the electron exchange and higher reactivity. The K-L plots for all layers are linear with a non-zero intercept as expected for a kinetically limited process, so we can assert that the kinetics limitation are not originated from slow charge propagation or slow diffusion of Oxygen through the catalytic film; in this case they would result into non-linearity[64]. The non-zero intercept, can be assumed as inversely proportional to the rate constant for the catalytic reaction.

Table 3: Comparison between calculate number of electron and BC0 for ORR.

INK	L_{Pt}	Number of electron	BC_o $mA \cdot cm^{-2} \cdot rpm^{-(1/2)}$
Theoretical Pt/C	-	4	0.143
Pt/C 40% Alfa Aesar	15 μg Pt/cm^2	3.53	0.131
Pt/C 40% + POM 2.5-2-10	15 μg Pt/cm^2	3.67	0.137
Pt/C 40% + POM 2.5-2-10	10 μg Pt/cm^2	3.81	0.142

All the BC_o values (**Table 3)** are close to the theoretical one[65], but the BC_o for Pt/POM layers appear to be higher than Pt/C values; this means that the process is advantaged for the layer modified with

POMs, which produced a best charge transfer, reflecting a probable decrease of rate constant at less negative potential[62].The general decrease of the BC_o compared with the theoretical one is due to the H_2O_2 production, typical for this process[66].

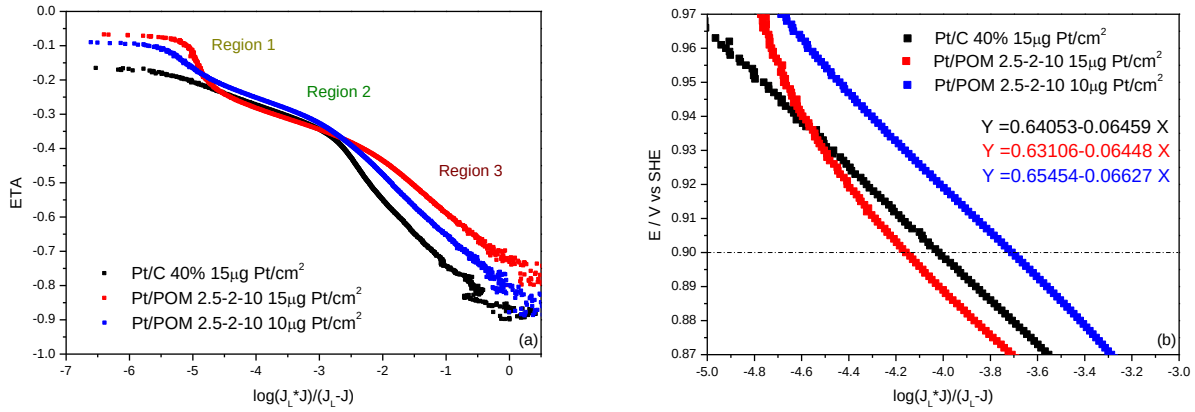

Figure 40: (a) ORR Tafel plots at 1600 rpm rotation speed of RDE voltammogram (reduction scan); low overpotential region oxygen Tafel plots at 1600 rpm rotation speed regards the positive going scan of RDE voltammogram.

In **Figure 40(a)**, we reported the full Tafel plots for ORR. We can distinguish three different slopes that are correlated to the number of electrons exchanged during the ORR. Generally, value of Tafel slope close to - 120 mV/dec means a single electron transfer, while value close to - 60 mV/dec suggest a two-electron transfer[67]. As shown from Tafel plots, there are two region (Region 1 and Region 3) in which the slopes are characteristic to single electron transfer, while the Region 2 shows a slope characteristic for two-electron transfer. A possible reaction path, including the three Region, can thus be formulated as:

Region 1	$O_2 + H^+ + e^- \rightarrow O_2H$	*(44)*
Region 2	$O_2H + 2H^+ + 2e^- \rightarrow H_2O + OH$	*(45)*
Region 3	$OH + H^+ + e^- \rightarrow H_2O$	*(46)*
Overall	$O_2 + 4H^+ + 4e^- \rightarrow 2H_2O$	*(47)*

POM-modified matrix can helps the reduction reaction due to its high acidity; so a big presence of protons on the catalytic sites leads to much faster reaction kinetics.

Table 4: Calculated values of Tafel slopes for ORR.

INK	L_{Pt}	Region 1	Region 2	Region 3
Pt/C 40% Alfa Aesar	15 μg Pt/cm^2	-	-66.4 mV/dec	-184.4 mV/dec
Pt/C 40% + POM 2.5-2-10	15 μg Pt/cm^2	-196.3 mV/dec	-62.9 mV/dec	-155.5 mV/dec
Pt/C 40% + POM 2.5-2-10	10 μg Pt/cm^2	-124.6 mV/dec	-67 mV/dec	-158 mV/dec

Table 4 shows calculated values of Tafel slopes for each layer. For Pt/C 40% the Region 1 is undetectable. This can be explained by the high formation of peroxide (see **Figure 38**) during the reaction that probably blocks the catalytic site, decreasing the reaction kinetics.

The best result is obtained from layer Pt/POM 2.5-2-10 L_{Pt} = 10 μg/cm^2, in fact value of -124.59 mV/dec suggests that modifier layer, with low Pt loading, favour a single step transfer and avoid a high peroxide formation.

Figure 40(b) shows the Tafel plots for different electrodes in the low potential region (0.9 V), where the influence of mass transport is negligible[66]. A good electrochemical speed reaction for layer Pt/POM 2.5-2-10 L_{Pt} = 10 μg/cm^2 is confirmed, but layer Pt/POM 2.5-2-10 L_{Pt} = 15 μg/cm^2 presents worse performances compared with the unmodified layer. The decrease in performance may be explained by a non-optimal Pt/POM ratio, and by the increase of the layer thickness that disadvantage physically kinetics of the reaction. Anyway some uncertainties in the results are given by the site-blocking and electronic effect of OH_{ads}[68]. It has been reported by Koper[69] that OH intermediates are formed through dissociative adsorption of molecular oxygen, followed by protonation and via water oxidation. As a consequence, the high amount of OH_{ads} species on Pt surface has an inhibition effect of Pt sites, resulting in reduced ORR rate.

4.1.2.4 CO stripping

The CO-stripping analysis (**Figure 41**) is useful to analyse the dynamics of CO poisoning catalyst, discovering the CO affinity that exist between CO and catalyst on a given support.

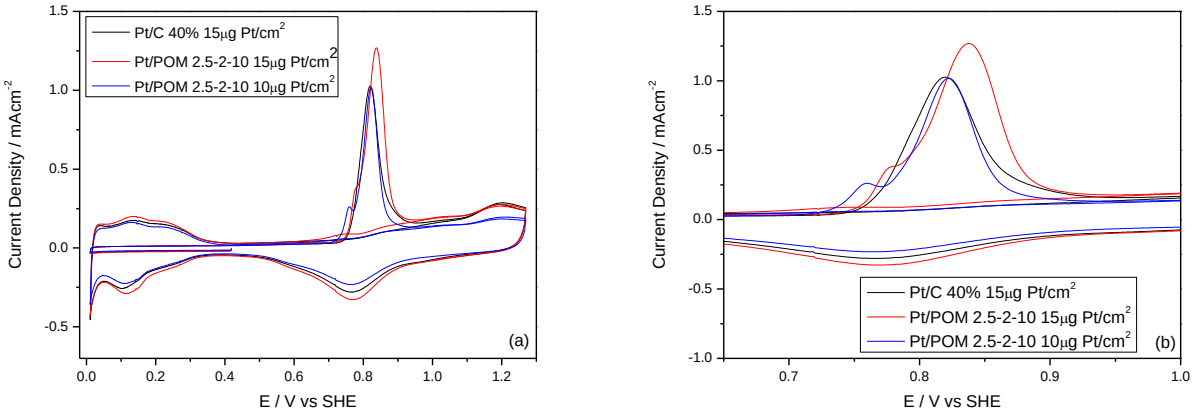

Figure 41: (a) First and second anodic and cathodic cycles of CO stripping CV for Pt/C and Pt/POM2.5-2-10.; (b) detail of CO stripping voltammetry peaks between 0.6V and 1V vs RHE. Electrolyte: $HClO_4$ 0.1M. Scan rate: 20 mV/s.

As we can see in **Figure 41(a)**, for all the catalytic layers the CO adsorbed totally blocks the catalytic Pt sites. This is evidenced at the beginning of the voltammogram, where the hydrogen adsorption/desorption peaks are not visible. CO adsorbed on Pt surface is completely oxidized in the first anodic scan. Completely CO removal is evident in the subsequent anodic scan, where there are no peaks between 0.6 V and 1 V. After stripping the Hydrogen peaks between 0.3 V and 0 V became visible.

Table 5: Peak and Onset potential for CO oxidation adsorbed on the catalytic layers (pure Pt/C as a reference).

INK	L_{Pt}	Peak Potential/V	Onset Potential/V
Pt/C 40% Alfa Aesar	15 μg Pt/cm^2	0.82	0.75
Pt/C 40% + POM 2.5-2-10	15 μg Pt/cm^2	0.84	0.73
Pt/C 40% + POM 2.5-2-10	10 μg Pt/cm^2	0.82	0.71

As shown in **Table 5** the Onset potential values of the systems modified with POM 2.5-2-10 are lower than reference system; the best improvement is observed, also in this case, for low Pt loading Pt/POM 2.5-2-10 modified layer. The results suggest that the CO stripping starts before for the system modified with POM 2.5-2-10 compared with the commercial Pt/C 40%.

The Cs-POM salts could behave as redox mediator for the CO-oxidation reaction with the Pt present in the system[62]. The proposed mechanism probably proceeds via the following reaction[70]:

$$POM + CO + H_2O \rightarrow CO_2 + H_2POM \qquad (48)$$

$$H_2POM \rightarrow HPA + 2H^+ + 2e^- \qquad (49)$$

The catalytic enhancement of the layer with Cs salts containing HPA as matrix may be due to synergistic effect between Pt and POM.

4.2 POM 3-2-10 characterization

4.2.1 Physical characterizations

4.2.1.1 SEM

In **Figure 42** is possible to observe SEM micrographs of POM 3-2-10.

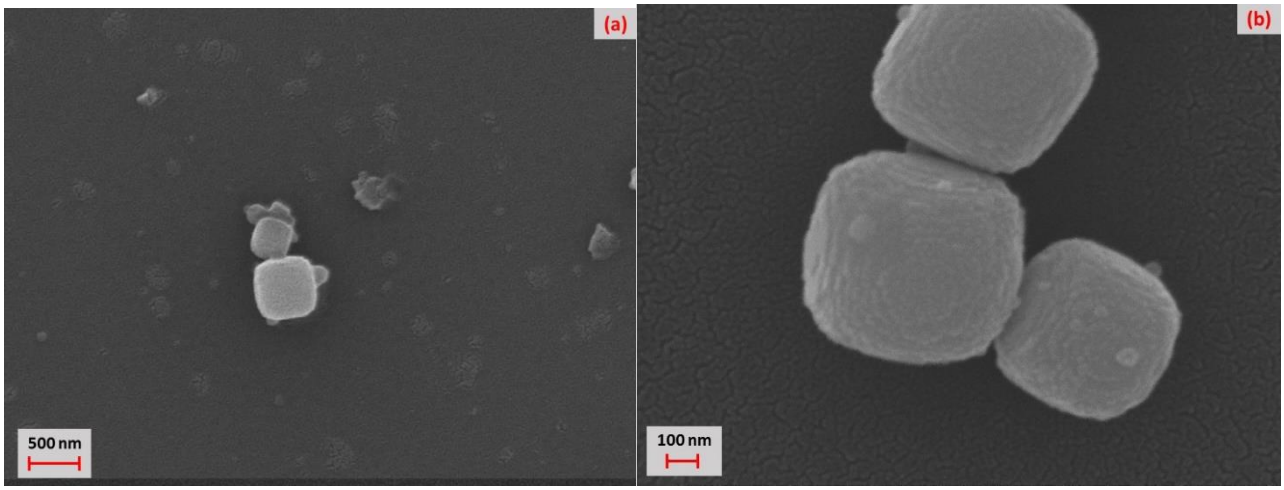

Figure 42: SEM micrographs of POM 3-2-10: a) 20000x magnification; b) 60000x magnification.

As in the case of POM 2.5-2-10, POM 3-2-10 presents different type of agglomerates of small cubic nanocrystals grains that appear to be more dispersed in comparison with starting HPAs (**Figure 31**), confirming morphological modification as a consequence of the Cs introduction during reaction. The grains dimension appears slightly bigger than Cs-2.5, with size around 200-500 nm. This size increase is probably correlate to the higher Cs addition during the synthesis. Also the particles appears closer to cubic morphology than Cs-2.5.

4.2.1.2 XRD

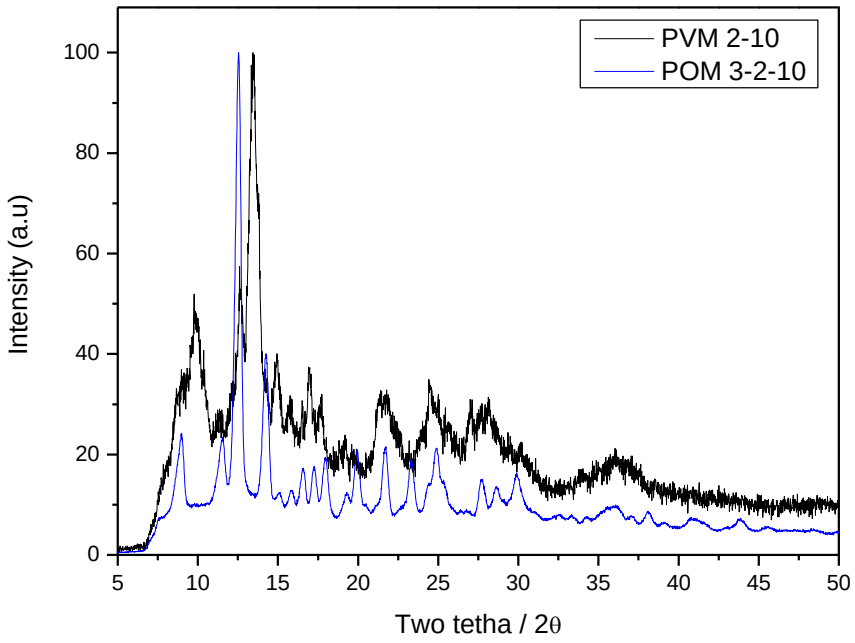

Figure 43: XRD analysis of POM 3-2-10 (blue) compared with that of PVM 2-10 (black).

Figure 43 shown XRD pattern of starting heteropolyacid PVM 2-10 compared with that of POM 3-2-10. Also POM 3-2-10 exhibits XRD pattern very similar to the reference acid, meaning that after the reaction POM salt maintains the Keggin-type structure. Peaks shift toward lower values is detected, probably due to the introduction of Cs^+ into a heteropolyacid compound that replace H^+ and will greatly influence its tertiary structure. Moreover, we can see as peaks for the POM salt are more defined than those of the acid, meaning a more ordered crystal lattice.

4.2.1.3 IR spectroscopy

Figure 44 shows the IR spectroscopy comparison between the starting heteropolyacid (PVM 2-10) and the POM 3-2-10 salt. Also in this case, the pattern of the salt is very similar the one of the heteropolyacid and there is a presence of shoulder peak at around 1000 cm^{-1}. The asymmetry for P-O bond vibration (1058 cm^{-1}) and Mo = O bond asymmetric stretching (955 cm^{-1}) indicates the presence of Vanadium atom in the structure, that replace one or more Mo atoms. Here we can also note the shift of the IR salt peaks respect to starting PVM, due to the presence and distribution of Cs^{+} cation in the material.

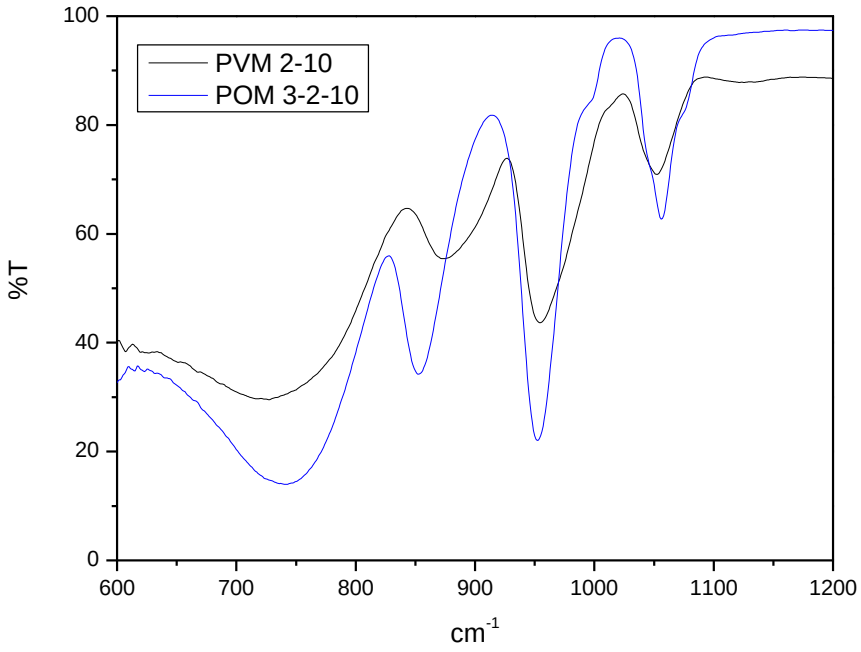

Figure 44: IR spectra of PVM 2-10 (black) and POM 3-2-10 (blue).

4.2.2 Electrochemical characterizations

4.2.2.1 Cyclic voltammetry

Figure 45 shows cyclic voltammetry of POM 3-2-10 compared with the cyclic voltammetry of the GC-adsorbed PVM 2-10. The shape is maintained between acid and salt but a shift toward positive potential is observed, probably due to the introduction of Cs^+ cation in the Kegging structure that also in this case gives thermodynamics influences.

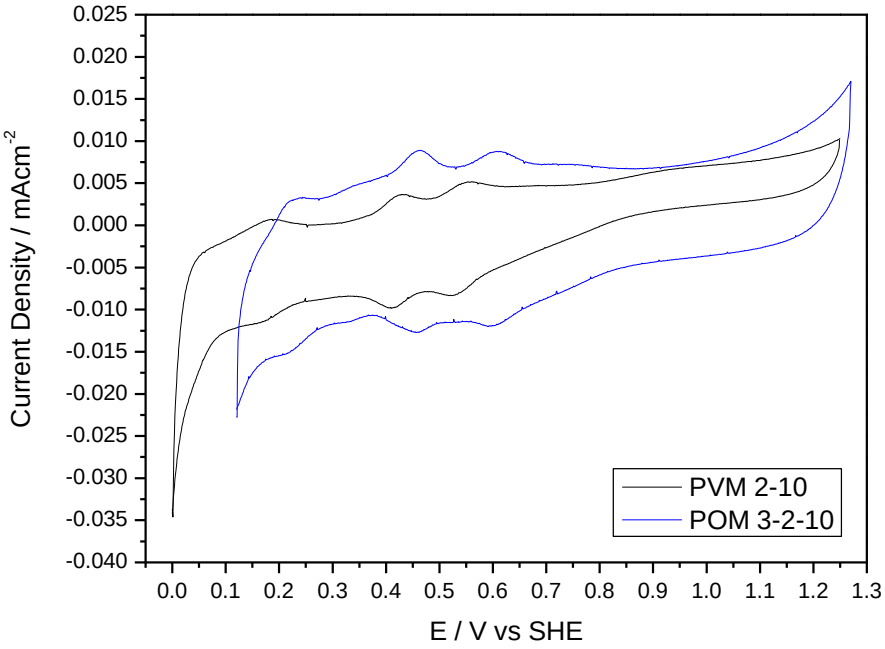

Figure 45: Cyclic voltammetry at GC electrode of PVM 2-10 (black) and Pt-free POM 3-2-10 coated electrode (blue). Electrolyte: H_2SO_4 0.5M. Scan rate: 10 mV/s.

4.2.2.2 Active area

Figure 46 shows the cyclic voltammograms of catalytic layers (Pt/POM 3-2-10) with L_{Pt} = 10 and 15 µg/cm^2 compared with the reference unmodified commercial ink (Pt/C 40%) with L_{Pt} = 15 µg/cm^2. For the modified layers the reduction of salts is partially covered by Hydrogen adsorption on Pt, in the region 0-0.3 V. Only the peak at 0.45 V, characteristic of POM is visible.

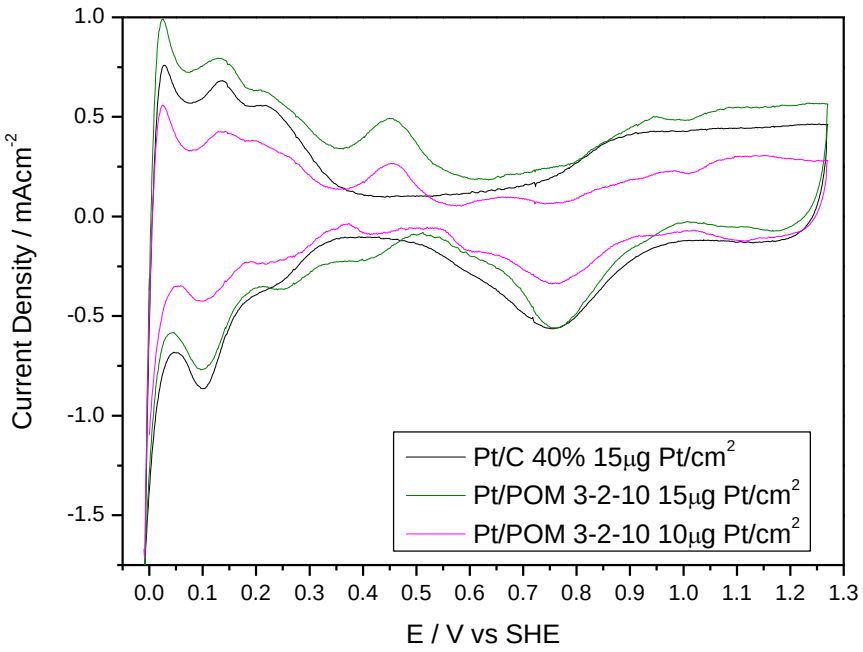

Figure 46: Cyclic voltammograms recorded in 0.1 M $HClO_4$ solution saturated with hydrogen. Scan rate: 50 mV/s.

As for layer Pt/POM 2.5-2-10, a shift of Pt-oxo (PtO or PtOH) species towards higher potentials respect to unmodified layer is visible.

Table 6: Comparison between calculate active area and R factor of layer with POM 2.5-2-10 mixed with Pt/C 40%.

INK	L_{Pt}	Calculate Active Area	Roughness Factor
Pt/C 40% Alfa Aesar	15 µg Pt/cm^2	2.50 cm^2	10.12
Pt/C 40% + POM 3-2-10	15 µg Pt/cm^2	1.65 cm^2	6.57
Pt/C 40% + POM 3-2-10	10 µg Pt/cm^2	1.36 cm^2	5.50

As we can see in **Table 6**, both layers Pt/POM 3-2-10 presents values lower than unmodified layer. There is an uncertainty in the calculation of the active area values due to the Cs peak (around 0.45 V) overlapping to that of Hydrogen redox processes. Anyway we can observe a small decrease in the value of Pt/POM 3-2-10 L_{Pt} = 10 µg/cm^{2}compared with that at L_{Pt} = 15 µg/cm^2.

4.2.2.3 ORR

In **Figure 47(a)** we can see an ORR onset potential shift toward positive potential, in particular for modified layers having Pt loading 10 μg/cm^2 respect to commercial Pt/C 40%. This shift indicates a lower activation energy due to a more favourable kinetics for the ORR. Modified layer with 15 μg/cm^2 of Pt loading shows similar results respect to the reference system, in particular in the first part of the curve. Around 0.7 V the POM modified layer shows more linear shape, while the commercial Pt/C present some irregularity, also in this case probably due to peroxide production during Oxygen reduction.

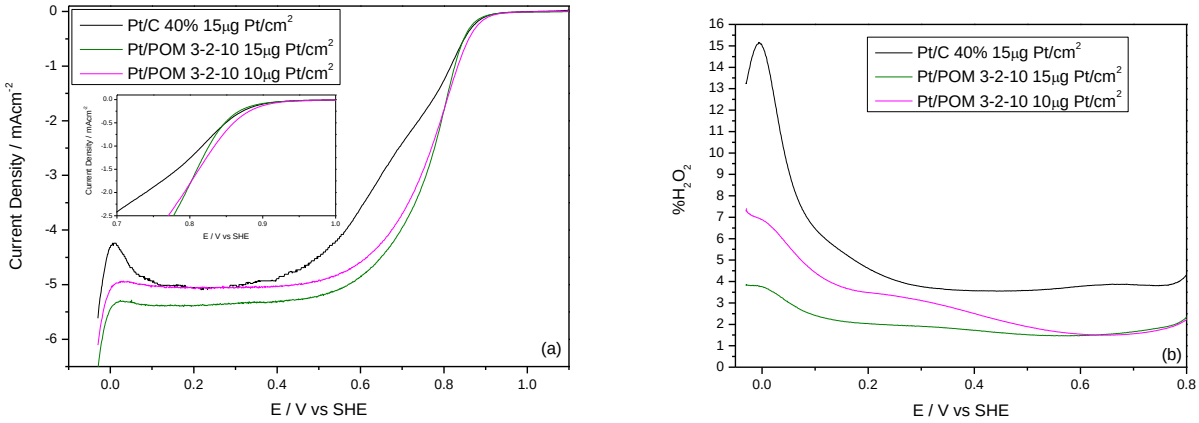

Figure 47: (a) comparison of selected RDE voltammograms at 1600 rpm rotation speed for ORR of Pt/C and Pt/POM electrodes. Insert: detail of the onset potential; (b) disk currents measured at E_{ring} = 1.2 V vs RHE and 1600 rpm. Electrolyte: $HClO_4$ 0.1M, scan rate: 5 mV/s

In **Figure 47(b)** we can see that at 0.6 V (i.e. the potential relevant to fuel cell cathodes) the calculated H_2O_2 is 3.8% for the Pt/C 40 %, compared with about 1% for both modified layers. This means that for the Pt/POM electrode the reduction of O_2 tends more towards four-electron mechanism. As we already discussed, peroxide formation increases significantly in the H_{upd} region, so at potentials lower than 0.6V the calculated value of formed H_2O_2 is increased until 4-7% for Pt/POM, while it increases about 15% for Pt/C. Also for Pt/POM 3-2-10 we can hypothesize better electrode performance in the case of real Fuel Cell using Pt/POM with lower Pt loading.

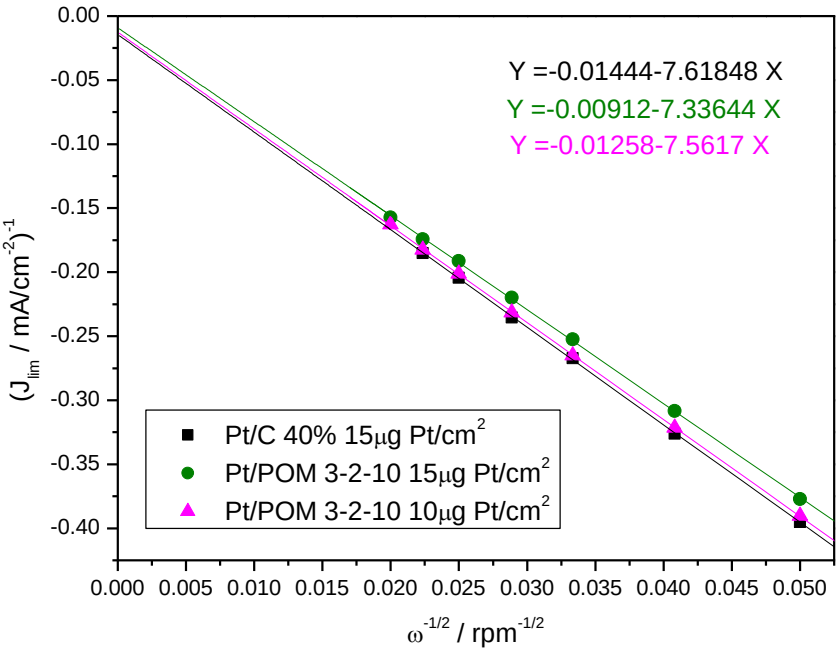

Figure 48: Comparison of Koutecky-Levich graphs of analysed catalytic layers, obtained using the data in Figure 47(a) at 0.3V.

Figure 48 shows Koutecky-Levich plots for Pt/POM 3-2-10 (L_{Pt} = 10 and 15 μg/cm^2) compared with that of Pt/C 40% (L_{Pt} = 15 μg/cm^2). Also in this case K-L slope decrease, meaning a more favourable process in the electron exchange and higher reactivity. The K-L plots for all layers are linear with a non-zero intercept so, the kinetics limitation are not originated from slow charge propagation or slow diffusion of Oxygen through the catalytic film.

Table 7: Comparison between calculate number of electron and BC0 for ORR.

INK	L_{Pt}	Number of electron	BC_o mA·cm^{-2}·rpm$^{-(1/2)}$
Theoretical Pt/C	-	4	0.143
Pt/C 40% Alfa Aesar	15 μg Pt/cm^2	3.53	0.131
Pt/C 40% + POM 3-2-10	15 μg Pt/cm^2	3.66	0.136
Pt/C 40% + POM 3-2-10	10 μg Pt/cm^2	3.75	0.140

All the BC_o values (**Table 7)** are close to theoretical. BC_o for Pt/POM modified layer appear to be higher than Pt/C values; this means that the process is advantaged for the layer modified with POMs, which produced a best charge transfer, reflecting a probable decrease of rate constant at less negative potential. Also in this case the general decrease of the BC_o compared with the theoretical one is due to the H_2O_2 production.

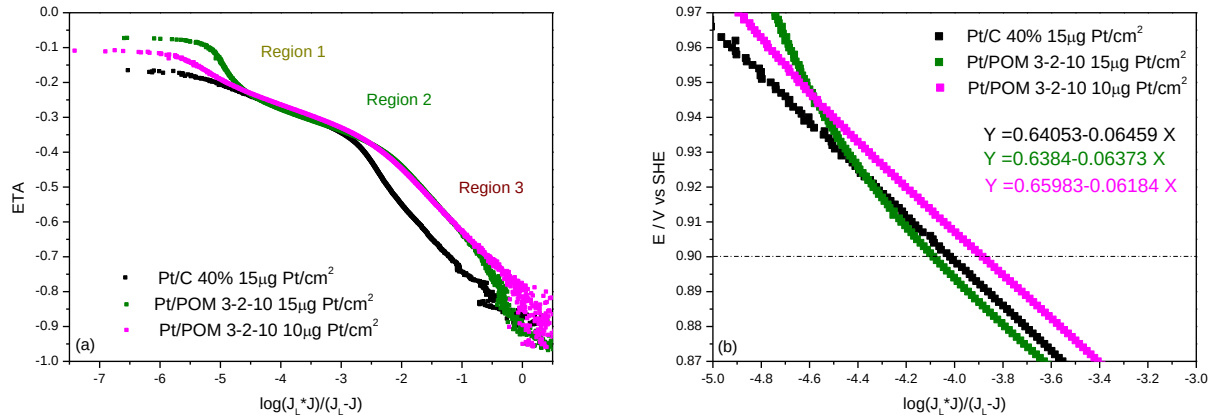

Figure 49: (a) ORR Tafel plots at 1600 rpm rotation speed of RDE voltammogram (reduction scan); low overpotential region oxygen Tafel plots at 1600 rpm rotation speed regards the positive going scan of RDE voltammogram.

In **Figure 49(a)** we reported the full Tafel plots for ORR. We can observe the presence of the three different Regions, discussed in *Section 4.1.2.3*, that are correlated to the number of electrons exchanged during the ORR. The results confirm the better behaviour in Region 1 for modified support respect to unmodified.

Table 8: Calculated values of Tafel slopes for ORR.

INK	L_{Pt}	Region 1	Region 2	Region 3
Pt/C 40% Alfa Aesar	15 μg Pt/cm^2	-	-66.4 mV/dec	-184.4 mV/dec
Pt/C 40% + POM 3-2-10	15 μg Pt/cm^2	-148.8 mV/dec	-61.4 mV/dec	-134.2 mV/dec
Pt/C 40% + POM 3-2-10	10 μg Pt/cm^2	-110 mV/dec	-63.4 mV/dec	-139.1 mV/dec

Table 8 shows the calculated Tafel slope values for each layer. Very good results are obtained for both modified layers with Pt/POM 3-2-10 that show, for all Regions, values close to the theoretical. In particular Pt/POM L_{Pt} = 10 μg/cm^2 layer shows a value very close to theoretical for Region 1, meaning that layer modified with low Pt loading, favour a single step transfer and avoid a high peroxide formation, more than other tested supports.

Figure 49(b) shows the Tafel plots for different electrodes in the low potential region (0.9 V). Also in this case good electrochemical speed reaction is confirmed for low Pt loading layer; while for Pt/POM 2.5-2-10 L_{Pt} = 15 μg/cm^2 layer worse performances are observed compared with Pt/C. The decrease in performance can be again explained by a non-optimal Pt/POM ratio, by the increase of the layer thickness that disadvantage physically kinetics of the reaction, while some uncertainties in the results are given by the site-blocking and electronic effect of OH_{ads}.

4.2.2.4 CO stripping

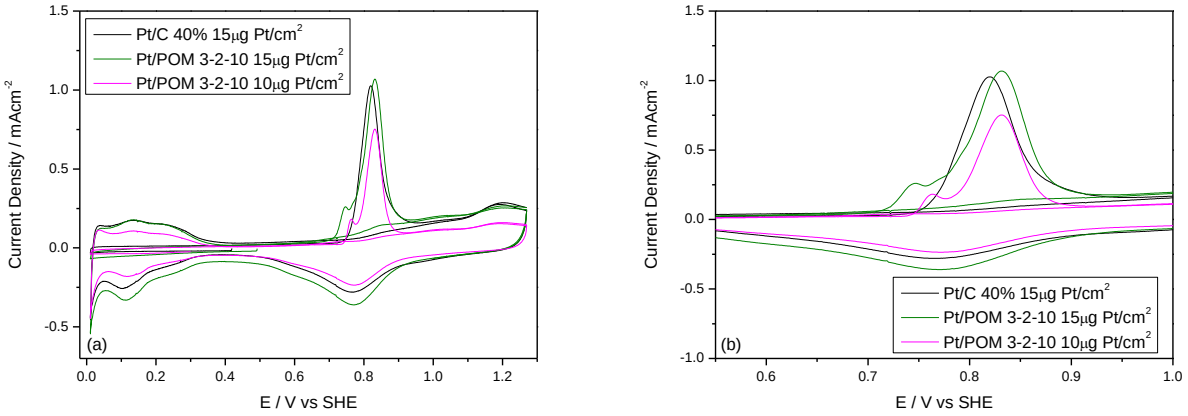

Figure 50: (a) First and second anodic and cathodic cycles of CO stripping CV for Pt/C and Pt/POM 3-2-10.; (b) detail of CO stripping voltammetry peaks between 0.6V and 1V vs RHE. Electrolyte: $HClO_4$ 0.1M. Scan rate: 20 mV/s.

Figure 50 shown the CO-stripping analysis for Pt/POM 3-2-10 layers compared with Pt/C reference. As we can see in **Figure 50(b)**, for all the catalytic layers the CO adsorbed on Pt surface is completely oxidized in the first anodic scan. In the subsequent anodic scan, where there are no peaks between 0.6 V and 1 V, CO is completely removed. We can see, in **Figure 41(a)**, the Hydrogen reduction peaks that appear between 0.3 V and 0 V after stripping.

Table 9: Peak and Onset potential for CO oxidation adsorbed on the catalytic layers (pure Pt/C as a reference).

INK	L_{Pt}	Peak Potential/V	Onset Potential/V
Pt/C 40% Alfa Aesar	15 μg Pt/cm^2	0.82	0.75
Pt/C 40% + POM 3-2-10	15 μg Pt/cm^2	0.83	0.71
Pt/C 40% + POM 3-2-10	10 μg Pt/cm^2	0.83	0.73

As shown in **Table 9** the Onset potential values of the systems modified with POM 3-2-10 are lower than reference system; the best improvement is observed again for Pt/POM 3-2-10 modified layer with L_{Pt}: 15 μg/cm^2. The results suggest that the CO stripping starts before for the systems modified with POM 3-2-10 compared with the commercial Pt/C 40%. Stripping reaction mechanism is reported in *Section 4.1.2.4*.

4.3 POM 3.5-2-10 characterization

4.3.1 Physical characterizations

4.3.1.1 SEM

Figure 51 shows SEM micrographs of POM 3.5-2-10.

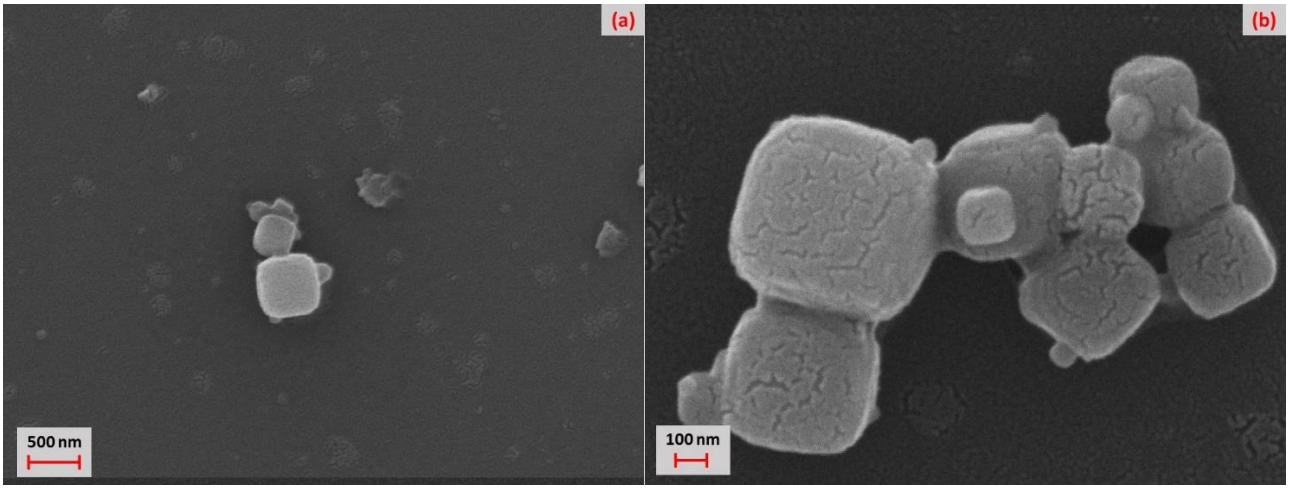

Figure 51: SEM micrographs of POM 3.5-2-10: a) 20000x magnification; b) 60000x magnification.

POM 3.5-2-10 presents different type of agglomerates of small cubic nanocrystals grains that appear to be more dispersed in comparison with starting HPAs (**Figure 31**), confirming morphological modification as a consequence of the reaction. In this case the cubic structure appear to be more defined than the previous synthesis. The formed particles dimension ranges from 50 to 400 nm.

4.3.1.2 XRD

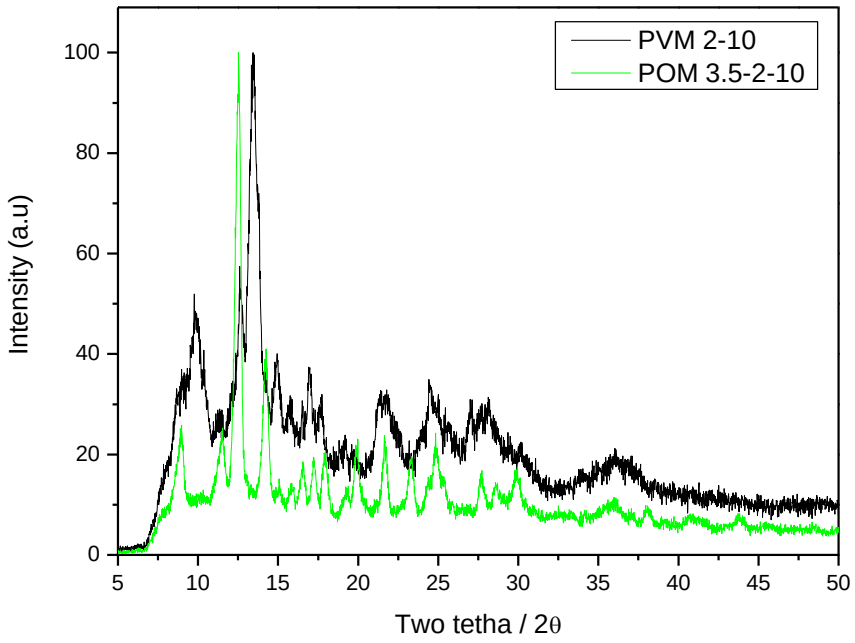

Figure 52: XRD analysis of POM 3-2-10 (green) compared with that of PVM 2-10 (black).

Figure 52 shows XRD pattern of starting heteropolyacid PVM 2-10 compared with that of POM 3.5-2-10. Also POM 3.5-2-10 exhibits XRD pattern very similar to the previous POMs analysed. Comparing with reference acid POM salt present more defined pattern, meaning a more orderly crystal lattice. The peaks shift toward lower values for POM 3.5-2-10 is confirmed also in this case, probably due to H^+ replace with Cs^+ cation. The Keggin-type structure is maintained.

4.3.1.3 IR spectroscopy

Figure 53 shows the IR spectroscopy comparison between the starting heteropolyacid (PVM 2-10) and POM 3.5-2-10. Also in this case, the pattern of the salt is very similar the one of the heteropolyacid and there is a presence of shoulder peak at around 1000 cm^{-1}. The asymmetry for P-O bond vibration (1058 cm^{-1}) and Mo = O bond asymmetric stretching (955 cm^{-1}) indicates the presence of Vanadium atom in the structure, that replace one or more Mo atoms. Here we can also note the shift of the IR salt values respect to starting PVM, due to the presence and distribution of Cs^{+} cation in the material.

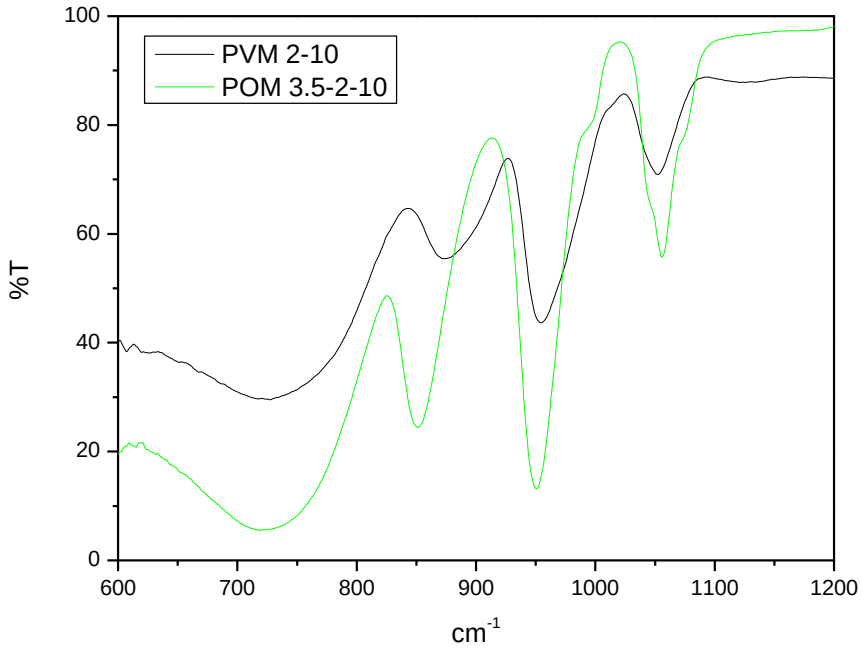

Figure 53: IR spectra of PVM 2-10 (black) and POM 3.5-2-10 (green).

4.3.2 Electrochemical characterizations

4.3.2.1 Cyclic voltammetry

Figure 54 shows cyclic voltammetry of POM 3.5-2-10 compared with starting PVM 2-10 adsorbed on GC electrode. The shape is maintained between acid and salt but a shift toward positive potential is observed, probably due to the presence of the Cs^+ cation in the Kegging structure that induces thermodynamics influences.

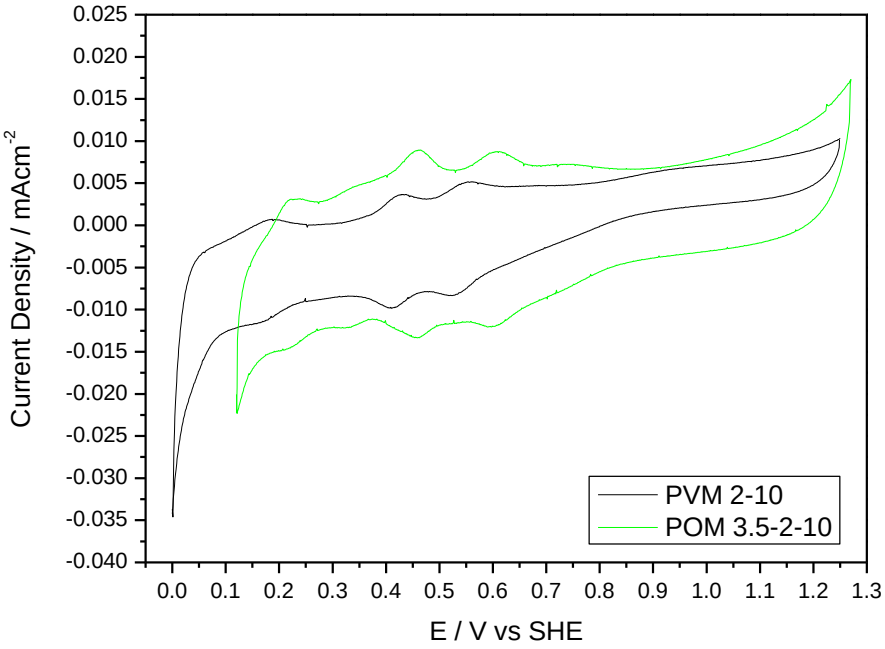

Figure 54: Cyclic voltammetry at GC electrode of PVM 2-10 (black) and Pt-free POM 3.5-2-10 coated electrode (green). Electrolyte: H_2SO_4 0.1M. Scan rate: 10 mV/s.

4.3.2.2 Active area

Figure 55 shows the cyclic voltammograms of catalytic layers (Pt/POM 3.5-2-10) with L_{Pt} = 10 and 15 µg /cm^2 compared with the reference unmodified commercial ink (Pt/C 40%) with L_{Pt} = 15 µg/cm^2. Also in this case only POMs reduction peaks around 0.45 V is visible and is partially overlapped with Hydrogen reduction process on Pt visible in the region 0-0.3 V.

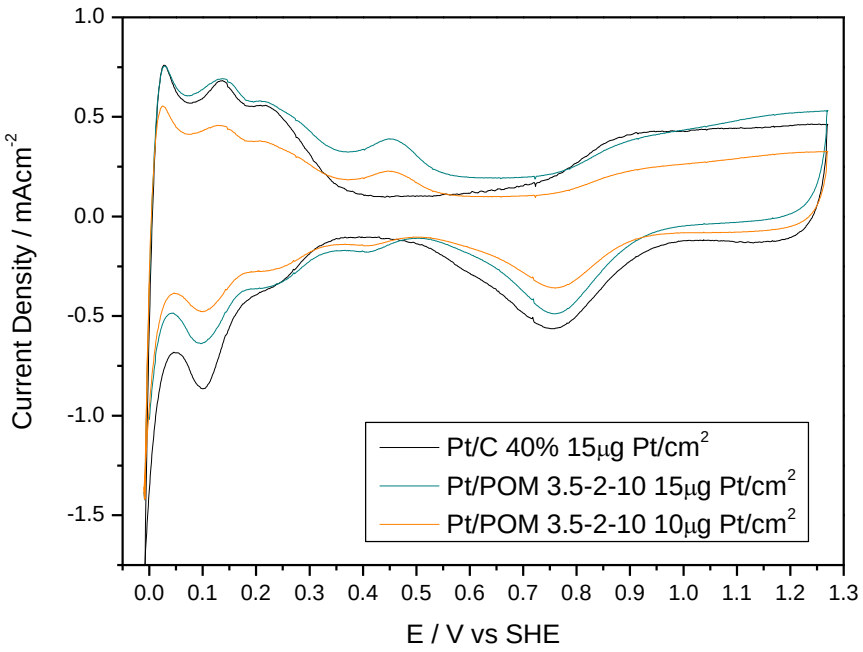

Figure 55: Cyclic voltammograms recorded in 0.1 M $HClO_4$ solution saturated with hydrogen. Scan rate: 50 mV/s.

As for the previous modified layers, a slightly shift of Pt-oxo (PtO or PtOH) peaks towards higher potentials is visible.

Table 10: Comparison between calculate active area and R factor of layer with POM 3.5-2-10 mixed with Pt/C 40%.

INK	L_{Pt}	Calculate Active Area	Roughness Factor
Pt/C 40% Alfa Aesar	15 µg Pt/cm^2	2.50 cm^2	10.12
Pt/C 40% + POM 3.5-2-10	15 µg Pt/cm^2	1.51 cm^2	6.11
Pt/C 40% + POM 3.5-2-10	10 µg Pt/cm^2	1.20 cm^2	4.81

As we can see in **As for** the previous modified layers, a slightly shift of Pt-oxo (PtO or PtOH) peaks towards higher potentials is visible.

Table 10 both Pt/POM 3.5-2-10 layers presents values lower than unmodified layer. Among POMs we shown so far, this is the one that presents the lowest active area values. As we previously told,

also in this case there is an uncertainty in the calculation of the active area values due to the overlapping of the Cs peak with the Hydrogen redox processes.

4.3.2.3 ORR

In **Figure 56(a)** we can see the RRDE test of modified inks with POM 3.5-2-10 using two different Pt loadings. In this test, in contrast with previous results, the layer with L_{Pt}: 15 μg/cm^2 shows remarkable improvement, showing a positive shift of onset potential using comparable Pt loading respect to the reference Pt/C. Low Pt loading ink presents loss of performance, but always comparable with high Pt loading reference ink. Also in this case there is a more linear shape respect to unmodified Pt/C that present some irregularity, probably due to peroxide production during Oxygen reduction.

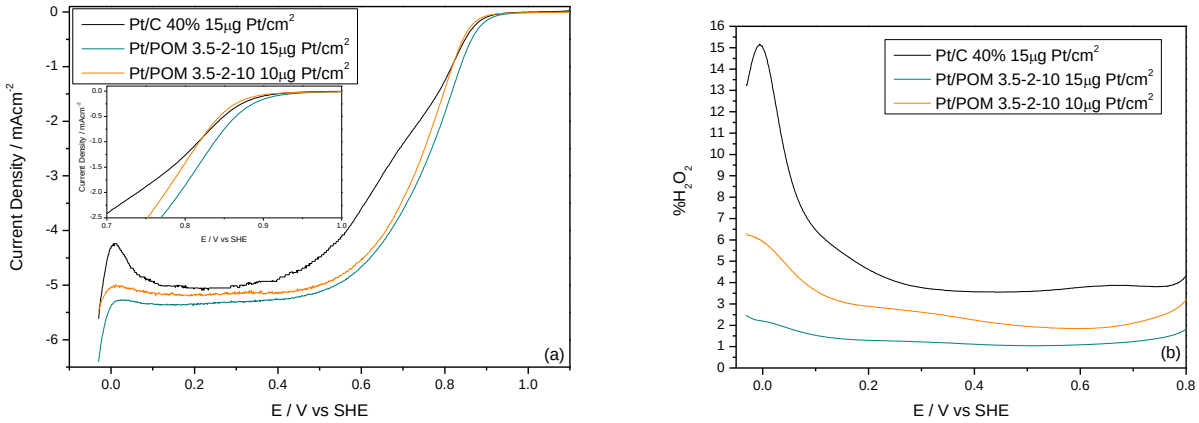

Figure 56: (a) comparison of selected RDE voltammograms at 1600 rpm rotation speed for ORR of Pt/C and Pt/POM electrodes. Insert: detail of the onset potential; (b) disk currents measured at E_{ring} = 1.2 V vs RHE and 1600 rpm. Electrolyte: $HClO_4$ 0.1M, scan rate: 5 mV/s

In **Figure 56(b)** we can see at 0.6 V (i.e. the potential relevant to fuel cell cathodes) H_2O_2 is 3.8% for the Pt/C 40 %, compared with about 1% for Pt/POM 3.5-2-10 L_{Pt}.= 15 μg/cm^2, and 2% for Pt/POM 3.5-2-10 L_{Pt} = 10 μg/cm^2. The high percentage of peroxide formation obtained for Pt/POM 3.5-2-10 L_{Pt} = 10 μg/cm^2 compared with Pt/POM 3.5-2-10 L_{Pt} = 15 μg/cm^2, can be an explanation for the worse performance for the layer at lower Pt loading. Anyway, peroxide formation increases significantly in the H_{upd} region, so at potentials lower than 0.6V the calculated value of formed H_2O_2 is increased until 4-7% for Pt/POM, while it increases about 15% for Pt/C. In this case we cannot hypothesize better electrode performance in the case of real Fuel Cell using Pt/POM with lower Pt loading.

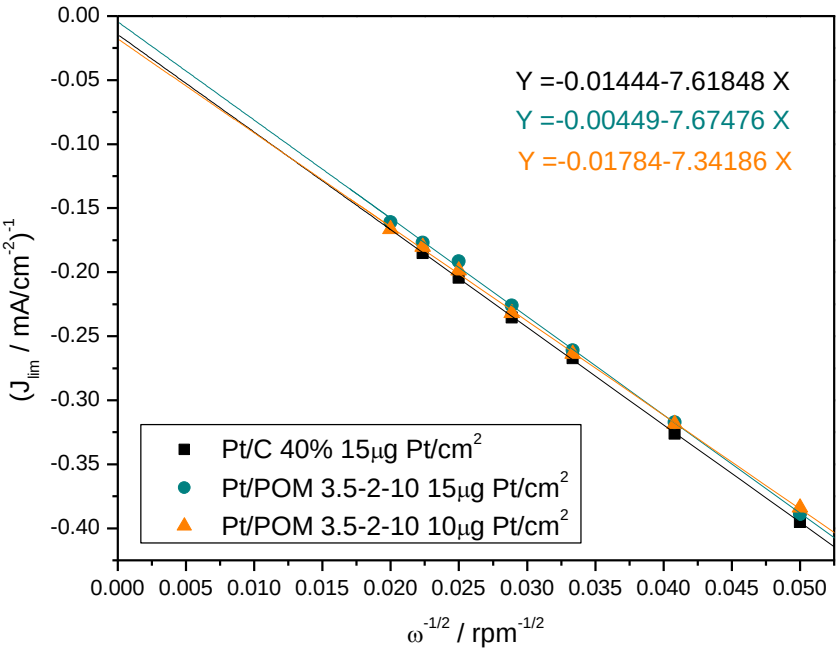

Figure 57: Comparison of Koutecky-Levich graphs of analysed catalytic layers, obtained using the data in Figure 56(a) at 0.3V.

Figure 57 shows Koutecky-Levich plots for Pt/POM 3.5-2-10 (L_{Pt} = 10 and 15 µg/cm^2) compared with that of Pt/C 40% (L_{Pt} = 15 µg/cm^2). The K-L plots for all layers are linear with a non-zero intercept so, the kinetics limitation are not originated from slow charge propagation or slow diffusion of Oxygen through the catalytic film. Decrease in K-L plot slope is observed only for layer Pt/POM with L_{Pt} = 10 µg/cm^2, while there is an increase, signature of worse kinetics, for the Pt/POM with L_{Pt} = 15 µg/cm^2.

Table 11: Comparison between calculate number of electron and BC0 for ORR.

INK	L_{Pt}	Number of electron	BC_o mA·cm^{-2}·rpm$^{-(1/2)}$
Theoretical Pt/C	-	4	0.143
Pt/C 40% Alfa Aesar	15 µg Pt/cm^2	3.53	0.131
Pt/C 40% + POM 3.5-2-10	15 µg Pt/cm^2	3.53	0.131
Pt/C 40% + POM 3.5-2-10	10 µg Pt/cm^2	3.66	0.136

All the BC_o values (**Table 11**) are close to the theoretical one. In this case the BC_o calculations for the different inks present similar value.

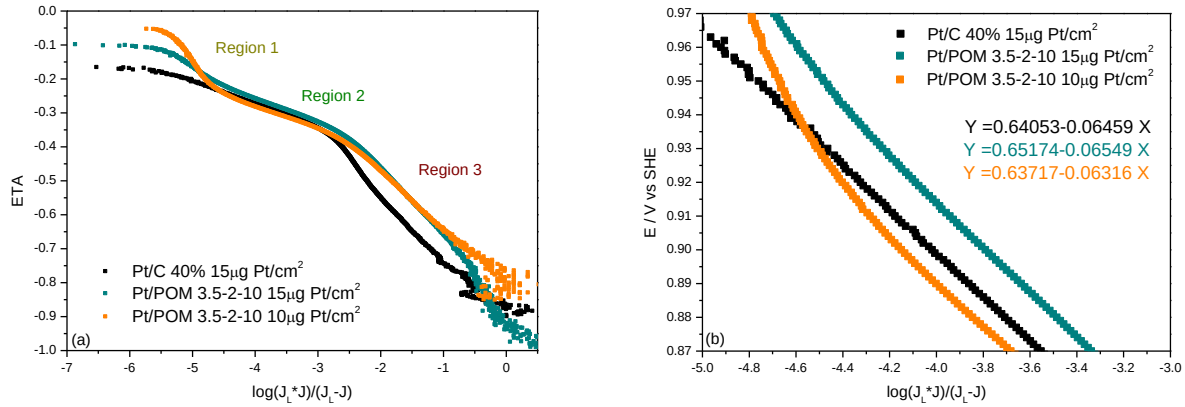

Figure 58: a) ORR Tafel plots at 1600 rpm rotation speed of RDE voltammogram (reduction scan); low overpotential region oxygen Tafel plots at 1600 rpm rotation speed regards the positive going scan of RDE voltammogram.

In **Figure 58(a)** we reported the full Tafel plots for ORR. From these results is possible to confirm that obtained in RRDE experiments. Also in this case three different Regions are presents, just discussed in *Section 4.1.2.3*, that are correlated to the number of electrons exchanged during the ORR. It is confirmed that Region 1 is more visible in the modified layer respect to reference system.

Table 12: Calculated values of Tafel slopes for ORR.

INK	L_{Pt}	Region 1	Region 2	Region 3
Pt/C 40% Alfa Aesar	15 μg Pt/cm^2	-	-66.4 mV/dec	-184.4 mV/dec
Pt/C 40% + POM 3.5-2-10	15 μg Pt/cm^2	-124.2 mV/dec	-66.1 mV/dec	-192.7 mV/dec
Pt/C 40% + POM 3.5-2-10	10 μg Pt/cm^2	-159 mV/dec	-63.1 mV/dec	-180.3 mV/dec

Table 12 shows calculated Tafel slopes values for each layer. Comparable results are obtained for Pt/POM 3.5-2-10 with L_{Pt} = 15 μg/cm^2 that shows, for Region 1 and 2, values close to theoretical values and similar to the reference system. Moreover, Pt/POM 3.5-2-10 layer with L_{Pt} = 10 μg/cm^2 shows, in Region 1, very high value that can be explained by a quite large number of peroxide products. **Figure 58(b)** shows the Tafel plots for different electrodes in the low potential region (0.9 V). In this case good electrochemical speed reaction are observed for layer Pt/POM 3.5-2-10 L_{Pt} = 15 μg/cm^2 compared with unmodified layer. Despite decrease in layer thickness, Pt/POM 3.5-2-10 with low Pt loading presents worse performance compared with 15 μg Pt/cm^2 POMs modified layer. The decrease in performance can be again explained by a non-optimal Pt/POM ratio, while some uncertainties in the results are given by the site-blocking and electronic effect of OH_{ads}.

4.3.2.4 CO stripping

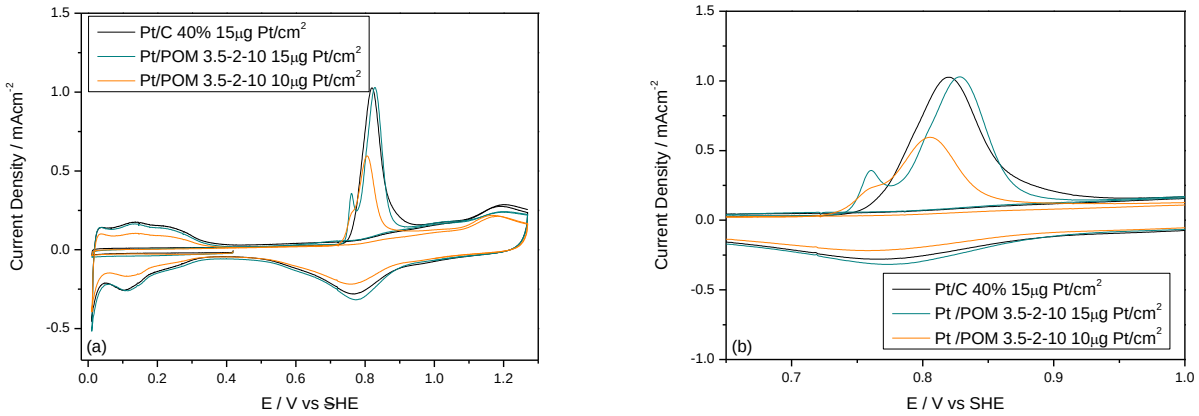

Figure 59: (a) First and second anodic and cathodic cycles of CO stripping CV for Pt/C and Pt/POM 3.5-2-10; (b) detail of CO stripping voltammetry peaks between 0.6V and 1V vs RHE. Electrolyte: $HClO_4$ 0.1M. Scan rate: 20 mV/s.

Figure 59 shows the CO-stripping analysis for layers Pt/POM 3.5-2-10 compared with unmodified layer. As we can see in **Figure 59 (b)**, for all the catalytic layers the CO adsorbed on Pt surface is completely oxidized in the first anodic scan. Completely CO removal is evident in the subsequent anodic scan (**Figure 59 (a)**), where there are no peaks between 0.6 V and 1 V. The complete CO stripping is confirmed by the presence of Hydrogen peaks between 0.3 V and 0 V in the subsequent voltammetry.

Table 13: Peak and Onset potential for CO oxidation adsorbed on the catalytic layers (pure Pt/C as a reference).

INK	L_{Pt}	Peak Potential/V	Onset Potential/V
Pt/C 40% Alfa Aesar	15 μg Pt/cm^2	0.82	0.75
Pt/C 40% + POM 3.5-2-10	15 μg Pt/cm^2	0.83	0.73
Pt/C 40% + POM 3.5-2-10	10 μg Pt/cm^2	0.80	0.72

As shown in **Table 13** the Onset potential values of the systems modified with POM 3.5-2-10 are lower than for the reference system; the best improvement is observed again for layer Pt/POM 3.5-2-10 with Pt loading 10 μg/cm^2. The results suggest that the CO stripping starts before for the system modified with POM 3.5-2-10 compared with the commercial Pt/C 40%.

4.4 Conclusions

In this section, we have analysed physical and electrochemical performance of the three POMs with different Cs amount, in order to get a preliminary forecast of electrochemical performance. In particular the work is focused to understand which combination of Pt/POM gives the best electrochemical performance and which of the three POMs synthesized enhances those benefits. As we have seen from physical analysis, the three POMs presents almost the same characteristics in morphology and structure; from SEM analysis is evident that when the Cs ratio increase, a more defined cubic conformation is observed. After Cs introduction, the co-catalyst results to be better dispersed respect to initial acid, and Keggin-type structure of the starting HPA is maintained after the synthesis reaction. Cubic nanocrystal agglomerates, from 50 nm to 500 nm of size, are formed.

As regards electrochemical analysis, we have obtained different electrochemical performance from the three POMs. In fact POM 2.5-2-10 and POM 3-2-10 with L_{Pt} = 10 μg/cm^2 (**Figure 60(a)**) have shown the best increases in performance compared with unmodified layer with higher Pt loading (15 μg/cm^2). These are very good result, meaning that with decrease in Pt loading, in the case of Pt/POM layers, we can obtain an increase in performance. Tafel Plot analysis in the low overpotential region confirm the good electrochemical speed reaction for layer POM 2.5-2-10 and POM 3-2-10. Worst result is obtained for POM 3.5-2-10 (**Figure 60(b)**). Reverse situation is obtained in the case of POM 3.5-2-10, with which best increase is obtained from the layer with equal Pt loading (15 μg/cm^2) compared with unmodified Pt/C.

Taking into consideration these results, we decided to analyse POMs 2.5-2-10 and 3-2-10 in working fuel cell, because they have shown improvements in performance with the low Pt content, which is one of the main goals of this work.

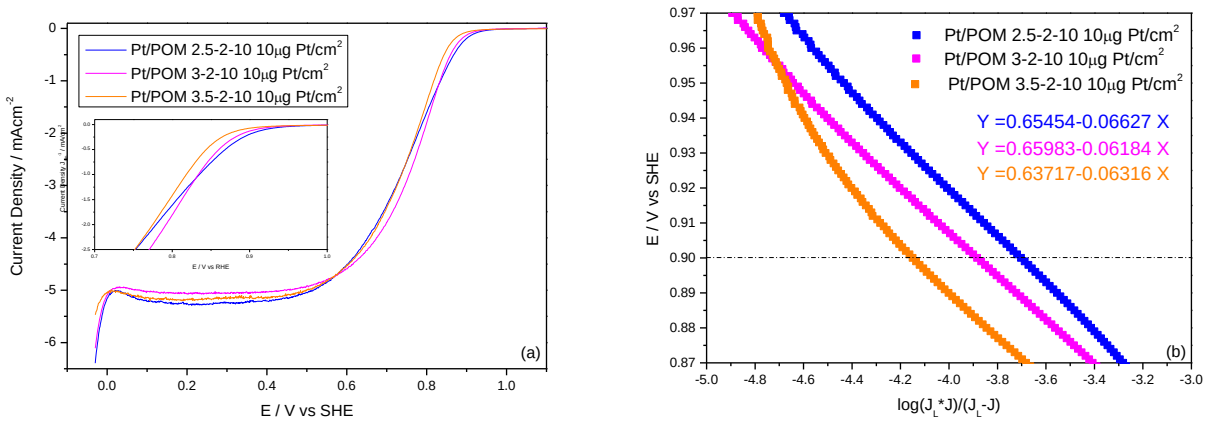

Figure 60: (a) comparison of selected RDE voltammograms for ORR of three Pt/POMs electrodes; (b) low overpotential region oxygen Tafel plots regards the positive going scan of RDE voltammogram for the three Pt/POMs. Rotation speed: 1600 rpm. L_{Pt}: 10 μg/cm^2.

4.5 Fuel Cell analysis

In this Section, we will see results obtained with a Fuel Cell employing a MEA made of commercial electrodes and separator, compared with modified MEA employing Pt/POM 2.5-2-10 and Pt/POM 3-2-10 cathodes. For each MEA, the anode is always a commercial ETEK (L_{Pt}: 0.5 mg/cm^2) and cathode is prepared using Pt/POMs ($L_{Pt} \approx$ 0.2 mg/cm^2) over commercial gas diffusion layer (GDL). For each analysis we followed the procedure described in *Section 3.3.5*.
We analysed three different MEAs:

- Comm. MEA = anode: Pt/C ETEK 0.5 mg/cm^2; cathode: Pt/C ETEK 0.5 mg/cm^2;
- Mod. MEA 1 = anode: Pt/C ETEK 0.5 mg/cm^2; cathode: Pt/POM 3-2-10 0.198 mg/cm^2;
- Mod. MEA 2 = anode: Pt/C ETEK 0.5 mg/cm^2; cathode: Pt-POM 2.5-2-10 0.21 mg/cm^2;

The analysis is performed at different RH: 100%, 62% and 17%.

4.5.1 RH 100%

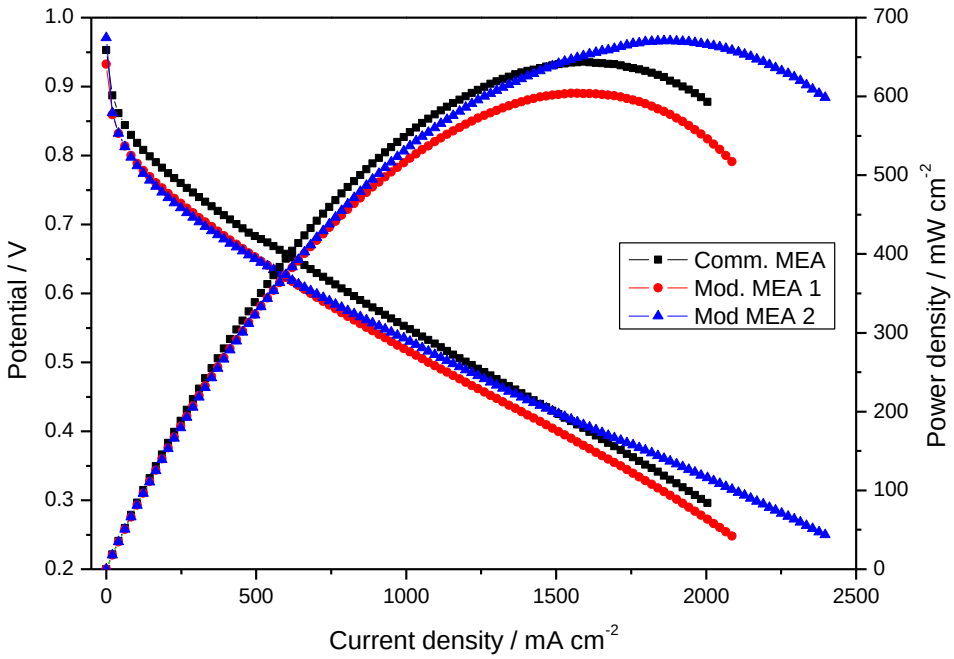

Figure 61: Polarization and power curves of: Comm. MEA (black); Mod. MEA 1 (red); Mod. MEA 2 (blue), obtained with 100% RH (70/70/70); feed gas: H_2 100ml/min, O_2 200ml/min; pressure: 2 bar.

Figure 61 shows performance tests performed at 100% relative humidity (T = 70/70/70). Despite the very low Pt loading at the cathode Mod. MEAs (62% reduction of Pt mass content), the performances are only slightly reduced especially in the final part of the curve. At 0.65V, the current density value for both Pt/POM-modified cells is 530 mA/cm^2, while for the commercial cell is 620 mA/cm^2. Reduction of 90 mA/cm^2 in current density is almost negligible considering the high decrease in Pt loading. At 0.3 V current density value for Comm. MEA is 1993 mA/cm^2, for Mod. MEA 1 is 1908 mA/cm^2 and for Mod. MEA is 2153 mA/cm^2. Differences between the two Mod. MEAs may be explained by a possible cell flooding during the analysis, or possible uncertainties and errors during inks preparation or cell assembly. Also Power density shows the same behavior, in fact values obtained at 1600 mA/cm^2 from the three cells are 645 mW/cm^2 for Comm. MEA, 606 mW/cm^2 for Mod. MEA 1 and 654 mW/cm^2 for Mod. MEA 2.

It is possible to confirm that the lower Pt loading is compensated by the higher Pt active surface and better charge transfer respect to commercial MEA, because of the same concurrent enhancing effects, already evidenced in previous RRDE characterization, as improved porosity and surface area, H^+ availability from acid POM matrix, improved Pt particles dispersion.

AC impedance spectroscopy measurements are performed in order to have a better comparison, on the electrochemical behavior, between commercial MEA and modifies MEAs. The impedance are collected at potentials of 0.4 V and 0.8 V, allowing the understanding of behavior at high and low current densities, respectively.

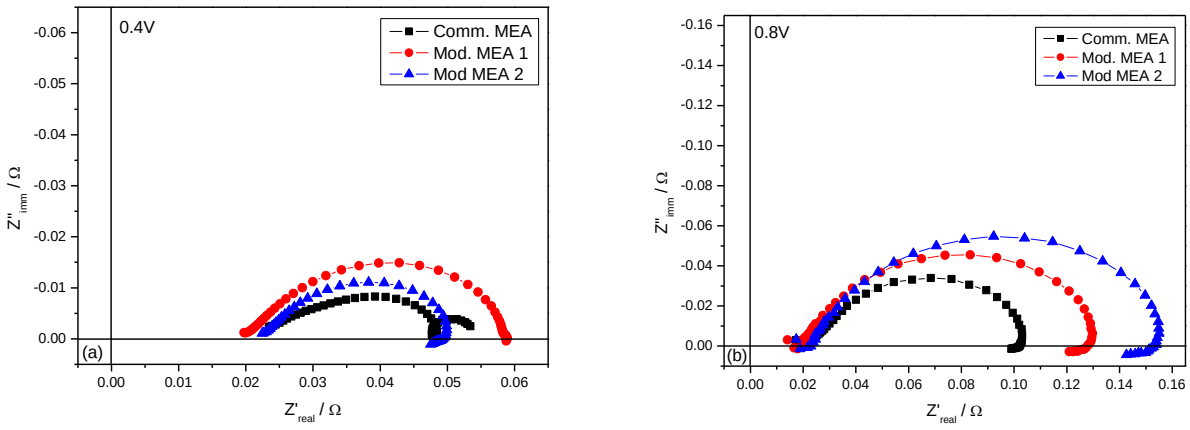

Figure 62: Nyquist plot of impedance spectroscopy tests of Comm. MEA and Mod. MEAs at two different voltage: (a) 0.4V; (b) 0.8V; obtained with 100% RH (70/70/70).

Table 14: Calculated values from Figure 62 of R_{el} and R_{ct}.

RH 100% 70/70/70	Comm. MEA		Mod. MEA 1		Mod. MEA 2	
	R_{el}/Ω	R_{ct}/Ω	R_{el}/Ω	R_{ct}/Ω	R_{el}/Ω	R_{ct}/Ω
0.4 V	0.020585	0.029061	0.018308	0.039945	0.021013	0.029109
0.8 V	0.019376	0.082741	0.019988	0.11363	0.022438	0.13639

Impedance results at high current densities **Figure 62(a)**, show that R_{el} values for all experiment are comparable; Mod. MEA 1 shows a slightly lower value, this means that the high acidity of POMs based cathode reduces the proton transfer resistance thorough the membrane. The first high frequency arc (R_{ct}) is visible for all experiments (combination of charge transfer resistance for the ORR and double layer capacitance within the catalyst layer) and shows higher values only for Mod. MEA 1 and comparable value for Mod. MEA 2, respect to Commercial reference, confirming the results obtained in polarization curves. The second arc at low frequency is visible only for Comm. MEA, and is associated with the mass-transport limitations of gas phase reactant (Oxygen), within the gas diffusion media. This is not visible for Mod. MEAs, hence no present limitation in mass-transport, meaning a more favourable transport of reactant, thanks to high porosity of POMs used. At low current density (**Figure 62(b)**), R_{el} values are comparable, while R_{ct} resistance for both Mod MEAs shows higher values respect to Comm. MEA, as expected.

4.5.2 RH 62%

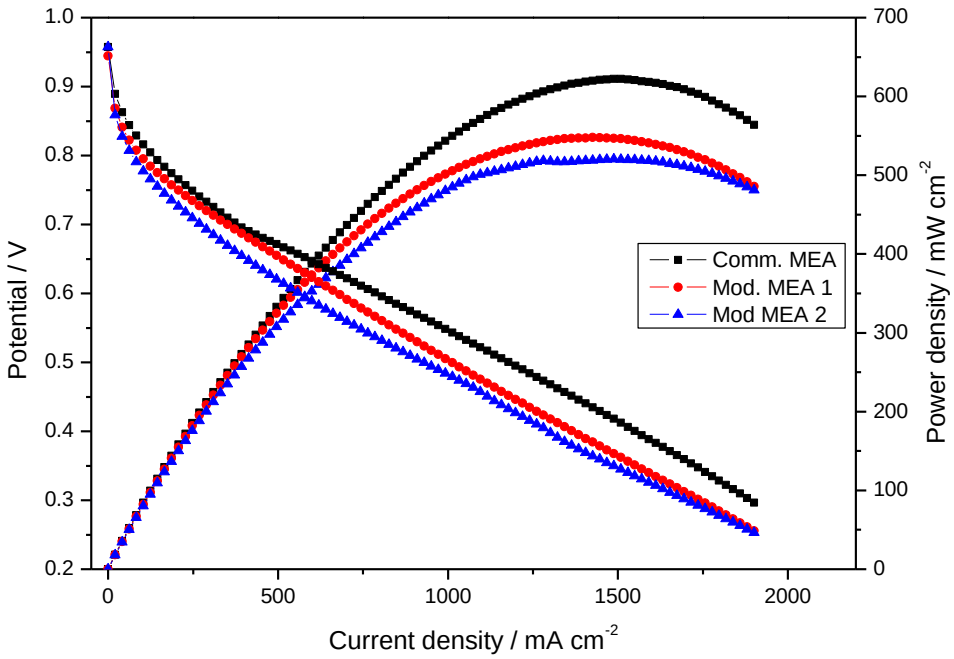

Figure 63: Polarization and power curves of: Comm. MEA (black); Mod. MEA 1 (red); Mod. MEA 2 (blue), obtained with 62% RH (60/70/60); feed gas: H_2 100ml/min, O_2 200ml/min; pressure: 2 bar.

Figure 63 shows performance test performed at 62% relative humidity (T = 60/70/60). As in previous situation, with high reduction in Pt loading at the cathode Mod. MEAs the performances are only slightly reduced. At 0.65V current density values for the cells are 515 mA/cm^2, 505 mA/cm^2 and 420 mA/cm^2 for Comm. MEA, Mod. MEA 1 and Mod. MEA 2, respectively. At 0.3 V current density value for Comm. MEA is 1860 mA/cm^2, for Mod. MEA 1 is 1760 mA/cm^2 and for Mod. MEA is 1720 mA/cm^2. We can observe an excellent response of Mod. MEA 1 that shows, in particular at 0.65 V, a comparable value with respect to Comm. MEA, despite the high Pt reduction. Mod. MEA 2 appears to be more influenced, confirming the response previously observed in RH 100%. Some systematic errors, in particular during the MEAs assembly, may also be considered. Power density shows the same behavior and values obtained at 1600 mA/cm^2 from the three cells are 610mW/cm^2, 545 mW/cm^2 and 525 mW/cm^2 for Comm. MEA, Mod. MEA 1 and Mod. MEA 2, respectively.

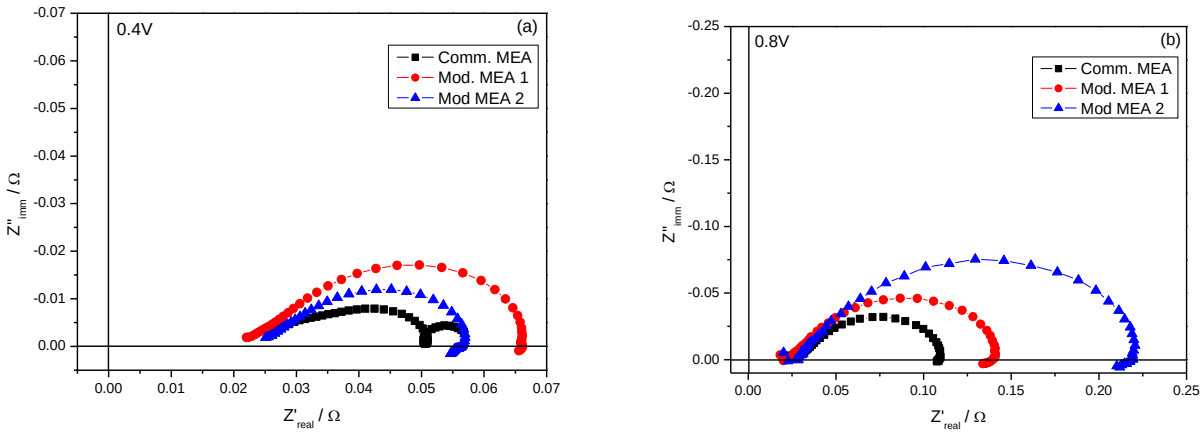

Figure 64: Nyquist plot of impedance spectroscopy tests of Comm. MEA and Mod. MEAs at two different voltage: (a) 0.4V; (b) 0.8V; obtained with 62% RH (60/70/60).

Table 15: Calculated values from Figure 64 of R_{el} and R_{ct}.

RH 62% 60/70/60	Comm. MEA		Mod. MEA 1		Mod. MEA 2	
	R_{el}/Ω	R_{ct}/Ω	R_{el}/Ω	R_{ct}/Ω	R_{el}/Ω	R_{ct}/Ω
0.4 V	0.021149	0.021149	0.020888	0.045801	0.023196	0.034309
0.8 V	0.024309	0.081927	0.025004	0.12015	0.028861	0.19971

Impedance results at 62% RH shows similar results respect the previous test at 100% RH. Values of R_{el} are comparable and only Mod. MEA 1, at high current densities, shows a slight resistance reduction. R_{ct} presents the same trend than 100% RH. Mass-transport limitations of gas phase reactant is visible also at high current density only for Comm. MEA. In conclusion at 62% relative humidity, thanks to the higher Pt active surface and better charge transfer respect to commercial reference, performance of modified MEAs seems to be comparable to Comm. MEA, despite the low cathode Pt loading used.

4.5.3 RH 17%

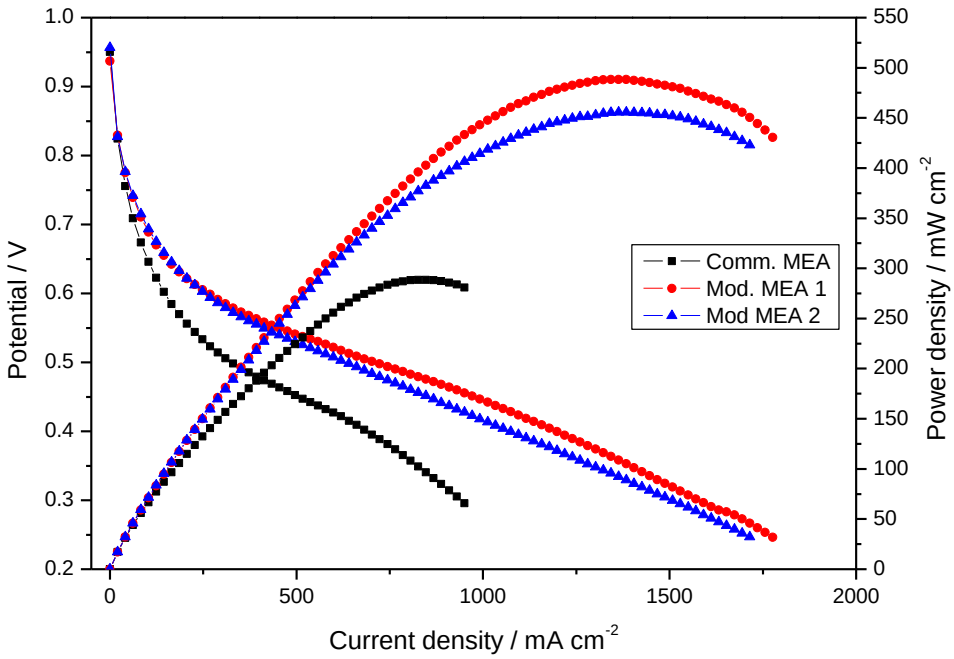

Figure 65: Polarization and power curves of: Comm. MEA (black); Mod. MEA 1 (red); Mod. MEA 2 (blue), obtained with 17% RH (40/70/40); feed gas: H_2 100ml/min, O_2 200ml/min; pressure: 2 bar.

Figure 65 shows performance test performed at 17% relative humidity (T = 40/70/40). Excellent results are obtained from this analysis conditions. An outstanding improvement of catalytic activity of the Pt nanoparticles supported by insoluble POMs respect to the commercial electrodes is observed, confirming the possible cell flooding in the previous experiments. At 0.65V current density values for both Pt/POM-modified cells is 165 mA/cm^2, while for the commercial cell is 95 mA/cm^2. Despite the very low Pt loading at the cathode, an increase of 90 mA/cm^2 is obtained. At 0.3 V current density value for Comm. MEA is 930 mA/cm^2, for Mod. MEA 1 is 1600 mA/cm^2 and for Mod. MEA 2 is 1535 mA/cm^2, registering an increase of about 650 mA/cm^2. In this case Mod. MEAs electrodes present a very similar performances, denoting a high improvement catalytic activity of the Pt in high dehydration conditions. Maximum power density values from the three cells are: 290 mW/cm^2, 490 mW/cm^2 and 455 mW/cm^2 for Comm. MEA, Mod. MEA 1 and Mod. MEA 2, respectively.

With this analysis we can confirm the higher Pt active surface and better charge transfer for Mod. MEAs electrodes compared to commercial reference.

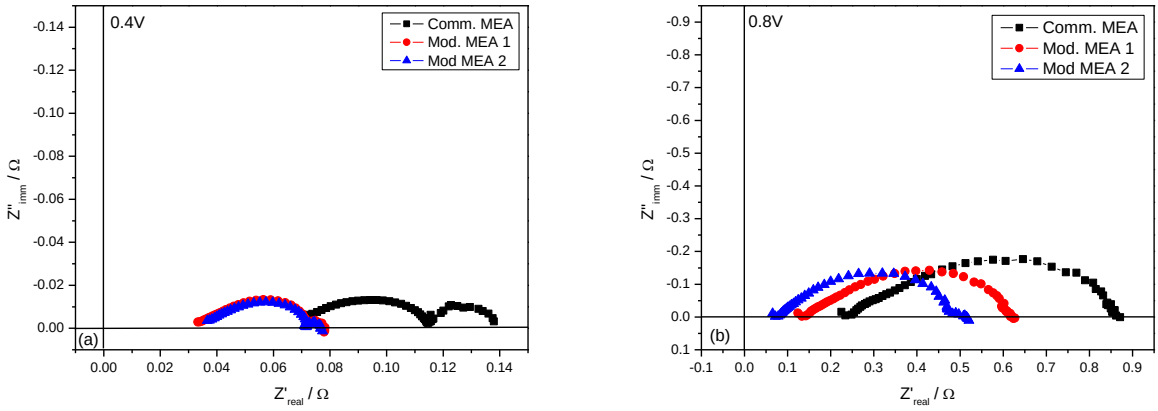

Figure 66: Nyquist plot of impedance spectroscopy tests of Comm. MEA and Mod. MEAs at two different voltage: (a) 0.4V; (b) 0.8V; obtained with 17% RH (40/70/40).

Table 16: Calculated values from Figure 66 of R_{el} and R_{ct}.

RH 17% 40/70/40	Comm. MEA		Mod. MEA 1		Mod. MEA 2	
	R_{el}/Ω	R_{ct}/Ω	R_{el}/Ω	R_{ct}/Ω	R_{el}/Ω	R_{ct}/Ω
0.4 V	0.052024	0.049411	0.030522	0.043292	0.032395	0.040927
0.8 V	0.22143	0.64613	0.1256	0.48661	0.066676	0.40478

The results of Impedance spectroscopy at RH 17% highlight the good results obtained with POMs use to build cathode. As is possible to see in **Figure 66(a)**, at high current density using the same polymer electrolyte membrane, the electrolyte resistance (R_{el}) undergoes a sharp drop, emphasizing that the high acidity of POM-based cathodes brings to higher H^+ availability, reducing resistance of proton transfer through the membrane. Also resistance to the charge transfer (R_{ct}) is lower, which means a favourable kinetics using POMs matrix as co-catalysts. The second arc at low frequency is now visible in all tests, but very small for both Mod. MEAs, which means that mass-transport limitations of gas phase reactant (Oxygen) within the gas diffusion media, is widely reduced in modified systems due to high porosity of POMs support. At low current density (**Figure 66(b)**) the results is confirm as well. Both R_{el} and R_{ct} are undergoes decrease.

4.5.4 Conclusions

In this last section, we have tested two POMs selected from preliminary electrochemical analysis (POM 3-2-10 and POM 2.5-2-10) that shown better catalytic performance with reduced Pt content. Cathode electrode with reduced Pt contents have been prepared and assembled in complete Fuel Cell, then tested at three different relative humidity values. The two cathode-modified MEAs with low Pt loadings have been compared with a totally commercial MEA (unmodified cathode and high L_{Pt}). The results at high RH are very interesting, because the POMs presence at the cathode compensate the low Pt loading, achieving very good and comparable performance with respect to Comm. MEA; mainly thanks to high POMs acidity that provide high H^+ presence. The slight performance reduction is attributed to low Pt content and a possible flooding that hides the real efficiency. Reducing RH at 62%, the results are almost the same. We have obtained outstanding results with a further reducing RH until 17%. The cell performance, even with Pt content reduced more than 60% are greatly increased, because POMs seem to act as humidity reservoirs. Both calculated resistances (R_{el} and R_{ct}) decrease, highlighting the improvement of H^+ transfer thorough the membrane and the better kinetics of charge transfer. This is thanks to high dispersion of Pt and enhances of active area, high porosity that reduce the mass-transport limitations of gas phase reactant (Oxygen) within the gas diffusion media and higher H^+ availability due to POM acidity. From results obtained with impedance analysis, we have hypothesized an equivalent circuit model valid for all the previous systems. We are in the case of a finite length diffusion (adsorption followed by charge-transfer process), usually described as circuit element "**O**", that can be approximated as[8, 71]:

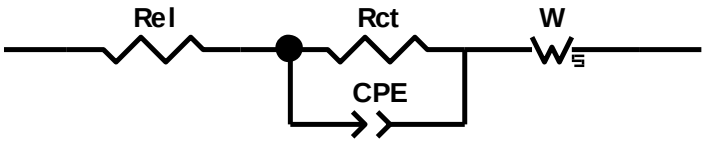

Figure 67: Proposed equivalent circuit model.

This electrical analogue, shown in **Figure 67**, consists of a resistance representing electrolyte impedance (R_{el}), combination of charge transfer for the ORR and double layer capacitance within the catalyst layer (R_{ct}) and Warburg impedance due to diffusion resistance[8].

5. CONCLUSIONS

In order to improve the ORR kinetics involved in PEM-fuel cells, insoluble polyoxometalates with formula $Cs_{2.5}H_{2.5}PMo_{10}V_2O_{40}\cdot 8H_2O$, $Cs_3H_2PMo_{10}V_2O_{40}\cdot 8H_2O$ and $Cs_{3.5}H_{1.5}PMo_{10}V_2O_{40}\cdot 8H_2O$ are synthesized, starting from the corresponding heteropolyacid $H_5PMo_{10}V_2O_{40}$. These salts are first physically an electrochemically characterized, then tested as co-catalysts support for Pt. The presented SEM analysis suggests a morphological modification when, after the synthesis process, protons in heteropolyacid are replaced by Cs^+ cations. In fact starting HPA presents larger and irregular morphology while POMs salts present smaller and more cubic nanocrystals grains. We can hypothesize that with the increment of the Cesium amount in the structure, this latter appears with a more defined cubic structure. IR spectra performed show that the primary Keggin structure of the HPA remains unaltered when protons are replaced by Cs^+ cations. Good results are obtained from RRDE electrochemical analysis. Investigated material have shown comparable performance at the same Pt loading (15 $\mu g/cm^2$) of the commercial reference and better performance when the L_{Pt} is lowered to 10 $\mu g/cm^2$ for POMs modified systems. There are two hypotheses may be put forward to explain the improvement of the catalytic activity of the Pt supported by POMs to the naked catalyst. One hypothesis regards the increase of the electrochemical properties due to high surface acidity, high proton conductivity, insolubility in water and fast redox behaviour, hence increase the kinetics and catalytic properties. The other hypothesis is oriented on the morphologies of the modified electrodes. Due to peculiar structure of the salts, the Pt nanoparticles trapped in the pores cannot grow above certain dimensions, decreasing the trend of the particles to aggregate and increasing the available active area. Moreover, the introduction of the Cs^+ in the Kegging structure leads to the formation of micropores and mesopores resulting in a significant increase in specific surface area, hence the permeability of the gases. Despite about 60% reduction of Pt mass content, Fuel cell test using Pt/POMs-modified cathodes show comparable performance in RH = 100% and RH = 62% conditions, while better activity are obtained at RH = 17 %. Therefore, the good activity registered with RRDE for Pt/POMs modified electrodes are also confirmed for real Fuel cell system, promising an important reduction of PEM-fuel cells cost and future developments in the use of this type of technology.

REFERENCES

[1] J. Laminie, A. Dicks, *Fuel Cell Systems Explained second edition*, **(2003)**.

[2] G. Hoogers, *Fuel cell technology handbook*, **(2003)**.

[3] Matthew M. Mench *Fuel Cell Engines*, **(2008)**.

[4] S. McIntosh, R.J. Gorte, *Chemical Reviews* 104 **(2004)** 4845.

[5] M. Winter, R.J. Brodd, *Chemical Reviews* 104 **(2004)** 4245.

[6] T. Fuller, K. Shinohara, V. Ramani, P. Shirvanian, H. Uchida, S. Cleghorn, M. Inaba, S. Mitsushima, P. Strasser, H. Nakagawa, H.A. Gasteiger, T. Zawodzinski, C. Lamy, *Proton Exchange Membrane Fuel Cells 8*, **(2008)**.

[7] B. Gou, W. Ki Na, B. Diong, *Fuel Cells: Modeling, Control, and Applications*, **(2010).**

[8] K.R. Cooper, V. Ramani, J.M. Fenton, H.R. Kunz, *Experimental Methods and Data Analyses for Polymer Electrolyte Fuel Cells*, **(2005)**.

[9] S. Litster, G. McLean, *Journal of Power Sources*, 130 **(2004)** 61-76.

[10] R.M.Q. Mello, E.A. Ticianelli, *Electrochim. Acta*, 42 **(1997)** 1031.

[11] J. Jiang, A. Kucernak, *J. Electroanal. Chem.*, 567 **(2004)** 123.

[12] H.A. Gasteiger, S.S. Kocha, B. Sompalli, F.T. Wagner, *Applied Catalysis B: Environmental*, 56 **(2005)** 9.

[13] Markovic, B.N. Grugur, P.N. Ross, *J. Phys. Chem*., B 101 **(1997)** 5405.

[14] L.W. Niedrach, I.B. Weinstock, *Electrochem. Technol*. 3 **(1965)** 270.

[15] M. Mastragostino, A. Missiroli, F. Soavi, *J. Electrochem. Soc.*, 151 **(2004)** A1919.

[16] C. He, H.R. Kunz, J.M. Fenton, *J. Electrochem. Soc*. 144 **(1997)** 970.

[17] J. Zhang, *PEM Fuel Cell Electrocatalysts and Catalysts Layers Fundamentals and Applications*, **(2008).**

[18] A.S. Aricò, S. Srinivasan, V. Antonucci, *Fuel Cells*, **(2001)**, 1, 133.

[19] L. Zhang, J. Zhang, DP. Wilkinson, H. Wang, *J. Power Sources*, 156 **(2006)** 171-82.

[20] M. Lefevre, E. Proietti, F. Jaouen, J.P. Dodelet, *Science*, 324 **(2009)** 71.

[21] H. Liu et al. / *Electrochimica Acta*, 52 (**2007**) 4532–4538.

[22] J. Maruyama, I. Abe, *J. Electrochem. Soc.*, 154 **(2007)** B297.

[23] P. Zelenay, *ECS Transactions*, 25 (1) **(2009)** 485-492.

[24] J. Fournier, G. Faubert, J.Y. Tilquin, R. Cote, D. Guay, J.P. Dodelet, *J. Electrochem. Soc*, 144 **(1997)** 145.

[25] P. Gouzerh, M. Che, *L'actualité Chimique*, 298 **(2006)** 9.

[26] M.Ammam, *J. Mater. Chem. A*, 1 **(2013)** 6291.

[27] J. C. Marignac, *Recherches chimiques et cristallographiques sur les fluozirconates*, *Ann. Chim. Phys.*, 3 **(1864)** 5.

[28]Z.P. Guoa, D.M. Hana, D.Wexler, R. Zenga, H.K. Liua, *Electrochimica Acta*, 53 **(2008)** 6410–6416.

[29] S. A. Williams, *Mendozavilite and paramendozavilite, two new minerals from Cumobabi, Sonora, Bol. Mineral.*, 2 **(1986)** 13.

[30] L.C.W.Baker, D.C.Glick, *Chemical Reviews*, 98 **(1998)** 3.

[31] M. T. Pope and A Muller; *Angew. Chem. ED. Engl*, 30 **(1991)** 34-48.

[32] J.M.Clemente-Juan, E.Coronado, *Coord.Chem.Reviews*, 193 **(1999)** 361.

[33] R.Neuman, "*Polyoxometalate Complex Oxidation Chemistry" in Progress in inorganic chemistry, Vol.47*, **(1998)**.

[34] T. Okuhara, T. Nakato, *Catalysis Surveys from Japan*, 2 **(1998)** 31-44.

[35] G.M. Brown, M.R. Noe-Spirlet, W.R. Busimg, H.A. Levy, *Acta Cryst.*, B33 **(1977)** 1038.

[36] T. Okuhara, T. Nakato, *Catalysis Surveys from Japan*, 2 **(1998)** 31-44.

[37] M.Sultan et al., *Applied Catalysis A: General*, 259 **(2004)** 141.

[38] T. Okuhara, *Chemical Reviews*, 102 **(2002)** 3641.

[39] Jung-Il Yang et al., *Applied Catalysis A: General*, 123 **(2000)** 194–195.

[40] R. Marassi, F. Nobili, *chapter in Encyclopaedia of electrochemical power sources*, **(2008)**.

[41] www.surfacesciencewestern.com

[42] Barbara H. Stuart, *Infrared Spectroscopy: Fundamentals and Applications, (***2004)**.

[43] D. Kealey, P. J. Haines, *Analytical Chemistry*, **(2002)**.

[44] Nicholas D. Spencer, John H. Moore, *Encyclopedia of Chemical Physics and Physical Chemistry: Fundamentals*, **(2001).**

[45] Joseph Wang, *Analytical Electrochemistry*, *Second Edition*, **(2001)**.

[46] Joseph Wang, *Analytical Electrochemistry, Third Edition*, **(2006)**.

[47] A.J. Bard, L. Faulkner, *Electrochemical Methods, Fundamentals and Applications*,**(2001)**.

[48] H. Wang, X. Yuan, H. Li, *PEM Fuel Cell Diagnostic Tools*, **(2012)**.

[49] Agata Godula-Jopek, *Hydrogen Production: by Electrolysis*, **(2015).**

[50] X. Yuan, C.Song, H.Wang, J. Zhang, *Electrochemical Impedance Spectroscopy in PEM Fuel Cells: Fundamentals and Applications*, **(2010)**.

[51] M.E. Orazem, B. Tribollet, P. Pintauro, *Tutorials in Electrochemical Technology: Impedance Spectroscopy*, **(2008).**

[52] E. Barsoukov, J. R. Macdonald, *Impedance spectroscopy theory, experimental, and Applications*, *Second edition*, **(2005)**.

[53] www.gamry.com

[54] Yaliang Tang, Anette M. Karlsson, Michael H. Santare, Michael Gilbert, Simon Cleghorn, William B. Johnson, *Materials Science and Engineering A*, 425 **(2006)** 297–304.

[55] M. Langpape, J.M.M Millet, U.S. Ozkan, M. Boudeulle, *J. Catalysis*, 181 **(1999)** 80.

[56] M. Sun, J. Zhang, C. Cao, Q. Zhang, Y. Wang, H. Wan, *Applied Catalysis A : General*, 349 **(2008)** 212-221.

[57] J.K. Lee et al., *Applied Catalysis A: General*; 214 **(2001)** 125.

[58] C. Rocchiccioli-Deltcheff, R. Thouvenot, R. Franck, *Spectrochim. Acta A*, 32 **(1976)** 587.

[59] R. Wlodarczyk, M. Chojak, K. Miecznikowski, A. Kolary, P.J. Kulesza, R. Marassi, *Journal of Power Sources*, 159 **(2006)** 802–809.

[60] K.Unoura and N.Tanaka, *Inorg. Chemistry*, **(1983)** 98, 219.

[61] M. Ai, *Appl. Catal*., 4 **(1982)** 245.

[62] M. Chojak, A. Kolary-Zurowska, R. Wlodarczyk, K. Miecznikowski, K. Karnicka, B. Palys, R. Marassi, P. J. Kulesza, *Electrochimica Acta* 52, **(2007)**, 5574–5581.

[63] U.A. Paulus, T.J. Schmidt, H.A. Gasteiger, R.J. Behm, *Journal of Electroanalytical Chemistry*, 495 **(2001)** 134–145.

[64] C.P. Andrieux, J.M. Dumas-Bouchiat, J.M. Saveant, *Journal of Electroanalytical Chemistry*, 131 **(1982)** 1.

[65] U. A. Paulus et al., *J. Phys. Chem. B*, 16 (**2002)** 106.

[66] S. Dsoke, A. Kolary-Zurowska, A. Zurowski, P. Mignini, P.J. Kulesza, R. Marassi, *Journal of Power Sources*, 196 **(2011)** 10591– 10600.

[67] J. Maruyama, M. Inaba, Z. Ogumi, *Journal of Electroanalytical Chemistry*, 458 **(1998)** 175–182.

[68] J. X. Wang, N.M. Markovic, R. R. Adzic, *J. Phys. Chem. B*, 108 **(2004)** 4127-4133.

[69] Marc T.M. Koper, *Fuel cell catalysis a surface science approach*, **(2009)**.

[70] R.J. Santis, M.-C. Kuo, J.A. Turner, A.M. Herring, *J. Electrochem. Soc.*, 155 **(2008)** B155.

[71] J. R.Macdonald, *J. Elecrtoanal. Chemistry*, 223 **(1987)** 25-50.